

UNIVERSITÀ
DI PAVIA

University of Pavia

Department of Earth and Environmental Sciences

Master of Science in

Agri-Food Sustainability

Loess Distribution along the Apennine Fringe of the Po Plain: Identification and Classification of Loess Deposits through Fieldwork, Digital Soil Mapping and Remotely Sensed Data, and Modelling of Their Spatial Distribution

Distribuzione del Loess nel Margine Appenninico della Pianura Padana: Identificazione e Classificazione dei Depositi Loessici Attraverso Rilievi di Campo, Cartografia Pedologica Digitale e Dati Telerilevati, e Modellizzazione della Loro Distribuzione Spaziale

Supervisor:

Prof. Michael Maerker

Co-supervisor:

Dr. Manuel La Licata

Master's Thesis by *Kartikey Bisht*

Matricola: 550276

Academic Year 2025 / 2026

Table of Contents

Abstract

1. Introduction
    - 1.1. Loess: definition, characteristics and significance
    - 1.2. Loess deposits in Northern Italy and the Po Plain Loess Basin
    - 1.3. Need for improved spatial characterisation of loess-related deposits in the Piacenza sector
    - 1.4. Geospatial approaches for mapping loess-related deposits
    - 1.5. Research questions, aim and objectives
2. Study Area
    - 2.1. Location and general description
    - 2.2. Geological Setting
    - 2.3. Geomorphological setting
    - 2.4. Climate
    - 2.5. Soils
    - 2.6. Land use and vegetation
    - 2.7. Erosional processes in the study area
3. Material and Methodology
    - 3.1. Overall Workflow
    - 3.2. Reference Framework: Cremaschi (1987) Stratigraphic Classification
        - 3.2.1. Rationale for adopting Cremaschi's units as the reference classification
        - 3.2.2. Description of target units – D3.1, D4 and D5
        - 3.2.3. Context classes – D2, D6 and D7
    - 3.3. Predictor Variables
        - 3.3.1. Conceptual framework: why terrain and spectral variables?
        - 3.3.2. Initial predictor pool and multicollinearity screening
        - 3.3.3. Terrain variables and their relevance to this thesis
        - 3.3.4. Spectral variables and their relevance to this thesis
        - 3.3.5. Terrain-only vs. terrain with spectral models: rationale for two models
    - 3.4. Field Data and Laboratory Analyses
        - 3.4.1. Design of field sampling
        - 3.4.2. Legacy validation point dataset
        - 3.4.3. Spectroradiometer analysis

3.4.4. Particle-size (texture) analysis
3.5. Data Preprocessing and Alignment
3.5.1. Derivation of Bare-soil point
3.5.2. Value-range masking
3.6. Model Training
3.6.1. Algorithm specification
3.6.2. Construction of spatial cross-validation fold
3.6.3. Final specification of Model A and Model B
3.7. Evaluation of Model
3.7.1. Evaluation metrics
3.7.2. Permutation importance procedure
3.7.3. Partial dependence plot procedure
3.8. Integration with Independent Geological Evidence
3.8.1. Analytical strategy statement
4. Results
4.1. Overview of Reporting Approach
4.2. Spatial Cross-Validation Performance
4.2.1. Comparison of overall performance
4.2.2. Confusion matrices
4.2.3. Per-class performance
4.3. Variable Importance (Permutation Importance)
4.3.1. Ranked importance, Model A and Model B
4.4. Partial Dependence Plot (PDP) Results
4.4.1. Model A (terrain-only)
4.4.2. Model B (terrain with spectral)
4.5. Spectral Mineralogy Results (SAM)
4.5.1. Overall mineral-match frequency
4.5.2. SAM angle statistics
4.5.3. Per-class mineral association
4.5.4. Soil reflectance spectra
4.5.5. Mineralogical interpretation
4.6. Particle-Size (Texture) Results
4.6.1. Class-mean texture

4.6.2. Sample-level detail and specific outliers
4.6.3. USDA texture classification
4.7. Spatial Prediction Maps
4.7.1. Categorical severity maps
4.7.2. Point-level correctness maps
5. Discussion
5.1. Model Performance and the Role of the Predictors
5.2. Geological Reading of the Units
5.3. Limitations and Future Perspectives
6. Conclusion

Abstract

This thesis maps the spatial distribution of three stratigraphic units along the Apennine fringe of the Po Plain (Northern Italy) - D3.1 (a buried vetusol developed on the Pede-Apennine fluviatile formation, which predates loess deposition), D4 (the Borzano gravels, a braided-river valley-fill deposit cut into the same formation) and D5 (a post-tectonic erosional surface, or piedmont glacis) - all three of which are subsequently capped by the polygenic Ghiardo loess. The pedostratigraphic classification by Cremaschi (1987) was adopted as the reference framework. Two Random Forest classifiers were run using a spatially structured, class-balanced five-fold cross-validation setup, specifically to limit spatial autocorrelation from artificially inflating the accuracy scores. The first, a terrain-only model, was trained on 600 points using slope, aspect, profile and general curvature, distance to the channel network and the LS factor. The second combined the same terrain predictors with four spectral variables, bands B3, B6, and B11 plus the ferrous index. However, we considered only the 346 points that fell within bare-soil locations, since the spectral bands are meaningless where vegetation or other cover obscures the ground.

Adding spectral data into the terrain model paid off as Out-of-fold accuracy climbed from 56.7% to 63.0%, a gain of 6.3 percentage points, while Cohen's kappa rose from 0.350 to 0.436 and multiclass AUC improved from 0.774 to 0.816. Both models performed very well and cleared the no-information baseline by far: the terrain-only model reached 56.7% against a 33.3% baseline, and the combined model reached 63.0% against a 37.9% baseline, the higher baseline here simply reflecting how unevenly the classes were represented once the data was narrowed down to bare-soil points. Both differences were statistically significant at $p < .001$. Ordinal severity error (RMSE) fell from 0.786 to 0.743 with the addition of spectral data. Distance to the channel network and the LS factor emerged as the two dominant predictors in both models via permutation importance. Partial dependence analysis showed D5's predicted probability rising consistently with slope, consistent with its documented origin as an erosional surface, while D4 showed a preference for concave curvature consistent with its valley-fill origin, and D3.1 showed terrain responses consistent with a stable, in-place buried profile.

These statistically derived patterns were further cross-checked against spectral mineral matching (Spectral Angle Mapper against the USGS Spectral Library) and Malvern particle-size analysis of field soil samples ($n = 18$ core samples across six stratigraphic units, plus 6 supplementary samples). There was broadly similar, loess-consistent mineralogy and grain-size signatures in D3.1 and D4, plausibly reflecting the shared Ghiardo loess cover common to both units, while D5 showed a distinct mineral assemblage consistent with its status as an erosional surface exposing older substrate. These results demonstrate that the combination of terrain and spectral remote sensing data within a spatially aware machine learning framework measurably improves the identification of loess-derived stratigraphic units and that the resulting classification patterns are geologically interpretable rather than purely statistical artefacts.

1. Introduction

1.1. Loess: definition, characteristics and significance

The term “Loess” is derived from the German word Löss or Löß, which means “Loose” (Višnić et al., 2013). Loess is an aeolian sediment composed predominantly of silt-sized particles (4-63 μm), usually sorted poorly and homogeneous in structure, which were deposited by wind over large portions of the Earth’s land surface during glacial and stadial periods (Pye, 1995; Muhs, 2013). When compared to well-sorted dune sand or the very fine dust that travels further from its source, loess tends to appear somewhere in the middle on sorting, moderate at best, often poor and this ultimately comes down to how loess actually reaches the places where it ends up: a mix of saltation plus suspension carried over both short and long atmospheric journeys (Muhs, 2013). In terms of minerals, quartz, feldspar, mica, clay minerals, carbonates and heavy minerals in varying amounts are finally a part of the deposit, which mostly tells us something about the rock from which the dust originally came and what happened to it along the way (Pye, 1995; Muhs, 2013). The deposit can appear different in different locations: sometimes it is barely a few centimeters of patchy cover, other times it forms a stack of over tens of metres, depending on the amount of dust available, the wind behaviour, the shape of the land, vegetation cover in the area and whether later erosion left it alone or chewed through it (Muhs, 2013; Lehmkuhl et al., 2021).

Loess's environmental importance and geomorphological behavior are much dependent on its physical properties. Fresh loess is usually porous, calcareous, silt-rich and weakly cemented; a massive structure with vertical joints or columnar fracture patterns caused by compaction, weathering, and shrinkage is observed in loess (Pye, 1995; Zhan et al., 2024). The high porosity of loess facilitates water infiltration and retention, although loess can lose strength when wet, particularly in case where the sediments contain very instable aggregates, macropores, or carbonate with weak bonds (Zhang et al., 2014). In the case of thick loess deposits, wetting can lead to structural collapse, subsidence, internal erosion, and slope instability, which proves the importance of this material not only for soil science and Quaternary studies, but also for land use planning and geological engineering (Zhang et al., 2014). The composition of minerals, degree of carbonate leaching, clay movement, intensity

of weathering, and formation of soil differ significantly in different loess deposits and provide insight into environmental conditions that took place during and after the deposition of sediments (Pye, 1995; Muhs, 2013).

Loess is found on all continents except Antarctica and occupies vast regions of Eurasia, North America, South America, Australia, New Zealand, Africa, and the Middle East (Muhs, 2013). The Chinese Loess Plateau, the European loess belt and the central United States are the most extensive loess regions, where accumulation of dust has been closely linked with Quaternary glaciation, large fluvial systems, arid source regions and patterns of changing atmospheric circulation (Muhs, 2013; Lehmkuhl et al., 2021). One of the world's most prominent loess regions is the Chinese Loess Plateau, which contains thick and laterally extensive sequences that document long-term changes in transport of dust, monsoon circulation in Asia, vegetation, weathering and landscape evolution through the Quaternary and late Cenozoic (Maher, 2016). In Europe, loess is distributed from southern England and northern France across Belgium, Germany, Poland, the Danube Basin, and Eastern Europe, with differences across regions in thickness, grain size, pedogenesis and preservation which reflects variation in glacial influence, periglacial processes, continentality, aridity and topographic setting (Antoine et al., 2001; Lehmkuhl et al., 2021). In North America, extensive loess deposits occur specifically in the Mississippi and Missouri river basins, where glacial grinding, outwash processes, floodplain sediment storage and subsequent wind deflation supplied large volumes of silt during Quaternary cold stages (Muhs, 2013).

One of the most important terrestrial archives of reconstructing Quaternary environmental change are the loess-paleosol sequences as they preserve alternating phases of accumulation of aeolian dust and soil development (Muhs, 2013; Maher, 2016). Usually, a loess layer marks a stretch when production of dust, atmospheric transport and deposition all improved, while a palaeosol tends to show up during quieter periods, while stronger weathering, higher effective moisture, thicker vegetation and soil formation did their work (Maher, 2016; Lehmkuhl et al., 2021). This is the reason why researchers dig into particle size, carbonate content, magnetic signals, geochemistry, isotopes, fossils and features of pedology derived from these sequences, because collectively they provide information about past wind strength, the source of sediment, rainfall and temperature patterns, shift in vegetation and how the soil itself developed (Zhisheng et al., 2014; Maher, 2016). These

processes did not happen in one continuous and tidy motion because individual layers can get reworked afterward through pedogenesis, freeze-thaw cycles, burrowing, dissolution, erosion or general disturbance, so understanding a loess sequence as a flawless, unbroken record of climate would be misleading (Stevens et al., 2007; Lehmkuhl et al., 2021). Therefore, understanding the palaeoenvironmental interpretation correctly requires a combination of pedology, stratigraphy, chronology, geomorphology and mineralogy all at once, and not depending on a single proxy and hoping it tells the whole story (Stevens et al., 2007; Maher, 2016).

On a practical note, the silt-dominated texture of loess-derived soils facilitates smoother spread of roots through them. Moreover, water holding capacity is very suitable for intensive farming in many parts of the world (Pye, 1995; Wang et al., 2014). However, just the loess does not guarantee the fertility of a given patch as organic matter, nutrient stores, carbonate status, clay mineralogy, drainage position on the slope, land-use history and its erosion history account as much as the parent material itself (Wang et al., 2014; Khan et al., 2022). Loess landscapes has significance in archaeology too due to the same reason they matter to paleoclimate work: Hence, old land surfaces can be preserved by a stratified layered loess, providing places where people once settled, animal remains and artefacts. All archaeological specimens are placed within a sequence that can be understood stratigraphically (Muhs, 2013; Xiong et al., 2023). The scientific, cultural, educational and scenic significance of loess has made it valuable to geological heritage, specifically where they preserve well-exposed loess-palaeosol sequences and archaeological records associated with it (Bollati&Zerboni, 2021).

Across the loess-covered areas, land degradation is a genuine concern, mainly due to the silt-rich material that is loosely bound together, which means it falls apart easily under runoff, concentrated flow or mass movement once vegetation cover thins out, slopes get steeper or the internal structure of soil is weakened by water infiltration (Zhang et al., 2024; Xiong et al., 2023). Sheet erosion, rill cutting, gullying and failure of slope can each reduce how thick, continuous and well-preserved a loess deposit remains and that in turn can cause decline in how well the soil functions both in terms of ecology and agriculture (Zhang et al., 2024; Xiong et al., 2023). In this thesis, erosional processes are treated as a background that shapes how well loess-related deposits survive and show up at the surface, rather than as something this research directly answers.

1.2. Loess deposits in Northern Italy and the Po Plain Loess Basin

The Po Plain stands as Italy's biggest stretch of alluvial lowland, essentially the surface footprint of a foreland basin situated between the Alps to the north and west as well as the Northern Apennines to the south, where tectonic movement, subsidence, sediment supply and river reworking have been the reason for how the landscape took shape across the Quaternary (Zuffetti et al., 2018). This region went through repeated environmental swings that were connected to glacial-interglacial cycles, shifts in how far ice extended, the behaviour of rivers, the amount of sediment moving, vegetation cover, soil formation and slope processes all changed as a result during the Late Quaternary (Cremaschi et al., 2015; Zerboni et al., 2015). The left-over of these processes is a layered, fairly intricate mix of fluvial, fluvioglacial, colluvial, aeolian and pedogenic deposits across the plain and its surrounding foothills, which is mainly a record of fluctuation in climate playing out against local tectonics and geomorphology (Zuffetti et al., 2018). The aeolian deposits residing within this setting belongs to the wider loess basin of Po Plain, which stretches across northern Italy and reaches into parts of the northern Adriatic and Dalmatian area (Bollati and Zerboni, 2021; Costantini & Carnicelli, 2018). The southern edge of the European loess belt is marked by this basin and what makes it distinct is that the loess here built up under a climate influenced by both continental European and Mediterranean regimes at once (Bollati & Zerboni, 2021; Zerboni, 2018).

The formation of loess in Northern Italy is generally tied to the cold, dry, windswept stretches of the Pleistocene, when thin cover of vegetation and a surplus of loose sediment let wind erode exposed alluvial, fluvioglacial and glacial material more easily (Cremaschi et al., 2015; Zerboni et al., 2015). The Po River system, its tributaries and glacial or fluvioglacial deposits along the Alpine and Apennine margins provided potential sources of fine mineral material that could be deflated and redeposited in topographically favoured settings (Costantini & Carnicelli, 2018; Zerboni, 2018). The principal phases of Upper Pleistocene loess deposition in many Northern Italian sequences are associated with Marine Isotope Stages 4-2, although the onset and duration of deposition differ among localities (Bollati & Zerboni, 2021; Zerboni et al., 2015). As shown by the recent chronological evidence from Monte Orfano, some loess accumulation in Northern Italy began before MIS 4, which demonstrates that regional aeolian sedimentation may have started during the later

part of MIS 5 (D'Amico et al., 2021). These differences in chronology emphasize that the Northern Italian record of loess cannot be treated as a single homogeneous depositional event, but instead reflects repeated phases of dust accumulation, surface stability, formation of soil, erosion and local sediment reworking through time (Cremaschi et al., 2015; D'Amico et al., 2021).

Loess in Northern Italy differs markedly from the thick and laterally continuous loess blankets that characterise major Central and Eastern European loess regions, because it commonly occurs as thin, discontinuous and spatially fragmented bodies across a variety of geomorphological settings (Costantini & Carnicelli, 2018; Zerboni, 2018). Loess deposits are distributed along the flanks of the Po Plain on dissected fluvial and fluvioglacial terraces, glacial deposits, isolated tectonic hills, karst plateaus, erosional surfaces, slopes and basins of secondary valleys (Costantini & Carnicelli, 2018; Zerboni, 2018). During glacial periods, these locations commonly served as sediment traps because topographic irregularities interrupted near-surface winds and favoured the accumulation of transported silt (Zerboni et al., 2015; Bollati & Zerboni, 2021). However, subsequent pedogenesis, bioturbation, colluviation, erosion and anthropogenic disturbance has strongly influenced the preservation of loess in Northern Italy, modifying or partly obscuring the original aeolian sedimentary characteristics (Costantini & Carnicelli, 2018; Cremaschi et al., 2015). Consequently, many deposits consist not of simple loess-paleosol couplets but of complex polygenetic pedosedimentary sequences in which successive events of sedimentation and soil-formation phases are superimposed within the same profile (Cremaschi et al., 2015; Zerboni et al., 2015). This spatial discontinuity and complexity in geomorphology make traditional extrapolation from isolated field exposures challenging and provide a strong rationale for combining field observations with modern spatial methods capable of incorporating both surface spectral information and context of terrain (Zerboni, 2018; Costantini & Carnicelli, 2018).

Several well-studied localities highlight the palaeoenvironmental and stratigraphic significance of loess in the Po Plain Loess Basin. Monte Netto, located in the central Po Plain, contains a complex loess-palaeosol sequence developed above older fluvial and fluvioglacial deposits, with accumulation of loess principally dated to MIS 4-2 (Zerboni et al., 2015). The Monte Netto sequence records repeated changes in environment during the Upper Pleistocene through changes in sedimentation, formation of soil and archaeological

evidence, which illustrates the value of isolated reliefs for preserving stratigraphic records that may be absent from the adjacent alluvial plain (Zerboni et al., 2015; Delpiano et al., 2019). The Ghiardo Plateau is situated on the southern margin of the Po Plain near Reggio Emilia, which contains loess profiles that accumulated during cold and dry phases of MIS 4 and MIS 3 and are associated with palaeosols and evidence of Middle Palaeolithic occupation (Cremaschi et al., 2015). Another important Northern Italian reference section is the Val Sorda sequence near Lake Garda, where loess overlies a truncated rubified palaeosol and consists of multiple buried Chernozem-type palaeosols that indicate recurrent phases of landscape stability and development of soil (Ferraro, 2009). At the regional scale, Bollati and Zerboni identified Monte Netto, Val Sorda, the Gajum section, Ghiardo Plateau, Valenza section and the Torino Hills as the most important known loess outcrops of the Po Plain Loess Basin, while the Romanengo Plateau was recognised as the benchmark site due to its inclusion in the Italian Inventory of Geosites (Bollati & Zerboni, 2021). Together, these sites show that Northern Italian loess sequences have considerable values in terms of palaeoclimate, palaeoenvironment, archaeology and geoheritage, while also displaying substantial amount of local variability in stratigraphy, thickness, pedogenesis, preservation state and setting of geomorphology (Bollati & Zerboni, 2021; Cremaschi et al., 2015).

Cremaschi provided a fundamental contribution to the understanding of Quaternary landscape evolution in the central Po Plain, who integrated lithostratigraphic, pedostratigraphic and geomorphological evidence to reconstruct the distribution and relative chronology of Quaternary formations and paleosols (Cremaschi, 1987; Zuffetti et al., 2018). Cremaschi's Map *of Quaternary Formations in the Central Po Plain*, published as an appendix to the monograph *Paleosols and Vetusols in the Central Po Plain*, provides the legacy cartographic and stratigraphic framework from which the mapped unit labels used in the present study were derived (Cremaschi, 1987). The map distinguishes Quaternary formations according to their sedimentary facies, position of geomorphology, pedostratigraphic characteristics, degree of soil development and relative context of chronology, rather than defining all units exclusively on the basis of occurrence of loess (Cremaschi, 1987; Zuffetti et al., 2018). The D2 – D7 labels used in the present study should therefore be understood as **legacy Quaternary depositional and pedostratigraphic map units**, not automatically as independent or uniformly primary loess classes (Cremaschi, 1987). For instance, the units are associated with legacy descriptions including coarse-textured fluvial formations, alluvial-fan gravels and sands, erosional surfaces, deeply

weathered vetusols and younger deposits characterised by different degrees of pedogenic development, which shows that the mapped categories consist a range of parent materials and landscape histories (Cremaschi, 1987). Although, loess may occur as a cover deposit, a pedogenically altered mantle, or a locally reworked component associated with some of these units (D3.1, D4 and D5), its occurrence and preservation must be verified through observations in the field, by interpretation of stratigraphy and sedimentological characterisation rather than inferred solely from the class label of legacy units (Costantini & Carnicelli, 2018; Cremaschi et al., 2015). In this thesis, Cremaschi's map is consequently used as a source of legacy reference classes for training data and evaluating spatial predictions. Instead, the field survey and laboratory analyses provide complementary evidence for assessing whether these classes correspond to distinguishable modern spectral, pedological and geomorphological characteristics.

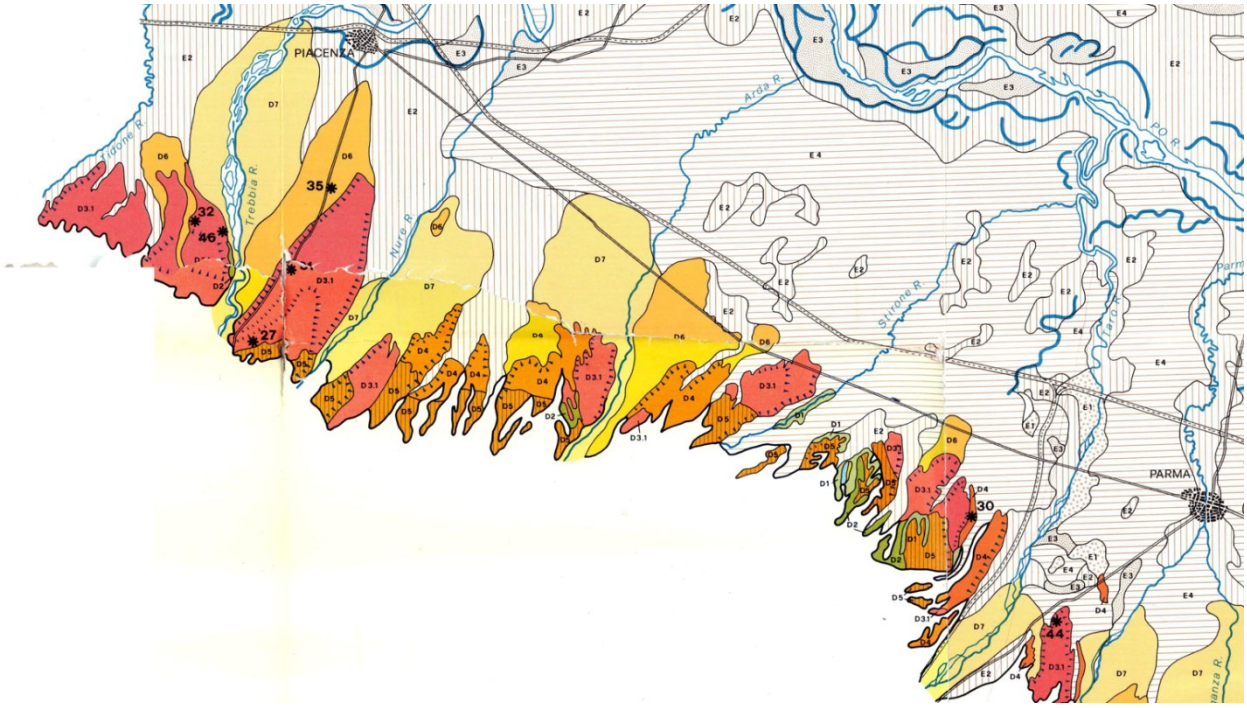


Figure 1.2: Extent of the Cremaschi (1987) Quaternary geological map of the central Po Plain and Apennine fringe, showing the location of the Piacenza study area and the distribution of the six loess units (D2–D7) investigated in this thesis.

Although the available loess in Northern Italy has major scientific values, its discontinuous distribution, local pedogenic overprinting, reworking of geomorphology and incomplete spatial characterisation remain important constraints for regional synthesis and conservation (Bollati & Zerboni, 2021; Zerboni, 2018). Along the Po Plain-Northern Apennines transition, the Piacenza sector occupies a strategically relevant position, where alluvial

deposits, terraces, foothill relief and Quaternary surfaces provide a potentially favourable setting for the occurrence and preservation of loess-related deposits and palaeosols (Cremaschi, 1987; Costantini & Carnicelli, 2018). However, the present-day boundaries, surface expression or spatial separability of the mapped units cannot be resolved by a legacy map alone due to the modification of the landscape by pedogenesis, land use, vegetation, redistribution of sediment and natural geomorphological processes since the original survey (Cremaschi et al., 2015; Zuffetti et al., 2018). These limitations create a need for spatially explicit approaches that combine legacy geological knowledge with new field observations, multispectral satellite imagery and terrain derivates to investigate the contemporary distribution and geomorphological context of loess-related Quaternary deposits in the Piacenza sector (Costantini & Carnicelli, 2018; Zerboni, 2018).

Loess Unit	Name	Altitude (m a.s.l.)	Lithology	Sedimentary Facies	Pedology (Depth of B/C boundary, Hue B horizon)	Loess Cover	Age
D2	Pedeapennine Fluvial formation (coarse-textured unit)	270–90	Gravels and gravelly sands	Alluvial fans	-	-	Early Middle Pleistocene
D3.1	CollecchioVetusol	245–60	Mainly weathered gravels	-	Vetusol, 5 m, 5 YR–2.5 YR	+	Middle Pleistocene
D4	Borzano Gravel	125–100	Gravels	Alluvial fans	-	+	Late Middle Pleistocene
D5	Piedmont Glacis	426–	-	Erosional	-	+	Late

		166		surface			Middle Pleistocene
D6	Cavriago Gravel	133–60	Gravels and gravelly sands	Alluvial fans	Vetusol, 1.5 m, 5–7.5 YR	-	Late Pleistocene
D7	Savignano Gravel	120–50	Gravels and sands	Alluvial fans	Ap/B soil, 0.50 m, 10 YR	-	Early Holocene

Table 1.2: Summary of the six loess units (D2–D7) identified in the Piacenza study area, showing age, formative process, oxidation/weathering status, and loess cover, as recorded in the legend of Cremaschi's (1987) Quaternary geological map (Appendix 6).

1.3. Need for improved spatial characterisation of loess-related deposits in the Piacenza area

There are several persistent methodological challenges in mapping the spatial distribution of loess and loess-related deposits, even where sediment sequences have been described in detail for individual outcrops. Loess bodies along the Po Plain margin, including the Piacenza area are typically patchy and thin, which as discontinuous mantles over terraces, isolated hills and erosional surfaces rather than as a continuous laterally extensive cover (Costantini & Carnicelli, 2018). Many of these deposits have suffered extensive pedogenic overprinting, as repeated processes of soil formation have altered or influenced partially their original sedimentary and stratigraphic signal, while some have also been affected by hillslope processes including colluviation, solifluction and slope wash, which represented additional hindrances for their stratigraphic continuity and spatial delineation (Costantini & Carnicelli, 2018; Cremaschi et al., 2015). This indicates that loess-related deposits in this region cannot be considered spectrally or morphologically uniform classes any more as original, pedogenized and reworked materials can coexist in the short distances, thus showing transitions between them rather than clear boundaries.

Furthermore, remote sensing mapping introduces additional uncertainties. The reflectance of bar soil can change depending on the amount of vegetation covering it, moisture content in the soil, the type of organic matter it possesses and the minerals present, thus even a small amount of vegetation can change the spectral response from the underlying soil or sediments making it impossible to get a clean signal from the pixel that reflects a mixture of both (Sadeghi et al., 2017; Buma et al., 2024). Soil moisture in particular has an outsized effect here, which shapes reflectance across the visible, near-infrared and shortwave-infrared ranges: as moisture increases, overall reflectance tends to decrease and the absorption features that researchers rely on to understand the texture and mineral content change in both depth and position (Sadeghi et al., 2017).

Furthermore, source of uncertainty arises from the legacy cartography itself. Legacy geological and soil maps, including those compiled prior to the widespread availability of GPS-based positioning often consist of positional errors on the order of tens to a few hundred metres. In addition to variability in mapping scale, classification criteria and the completeness of field verification are underlying the original survey (Rossiter, 2019; Batjes et al., 2023). Such positional and classification uncertainty can propagate into the derived model outputs, where a legacy map is subsequently used as a source of training or reference data for spatial modelling, particularly at the fine spatial resolution required to resolve patchy and discontinuous deposits (Batjes et al., 2023; Shi et al., 2024). These combined challenges, which comprises of heterogeneous deposit preservation, spectral confusion introduced by vegetation, moisture and land management and inherited uncertainty in legacy cartography, signify that the spatial characterisation of loess-related deposits cannot rely on any single source of data in isolation.

This thesis addresses this challenge for the Piacenza area of the Po Plain-Apennine transition, where the map of Cremaschi (1987) provides a valuable starting point for stratigraphy and cartography but has not yet been evaluated using current field and remote-sensing methods. The situation of present day's spatial expression and spectral separability in relation to the legacy units have not yet been systematically evaluated using an integrated framework which combines terrain derivates, Sentinel-2 imagery, field observations and machine-learning classification. To address this gap, there is a need to combine the stratigraphic and geomorphological information already contained in the legacy map with independently collected evidence from field and remotely sensed data. Thus, we can test

whether the mapped units retain a coherent and separable spatial and spectral identity under present-day conditions. Geomorphological processes influence the preservation and surface characterisitcs of loess-related deposits including, runoff-driven erosion and reworking of local hillslope. Thus, terrain derivates are relevant not only to mapping but also to interpret the distribution and preservation state of the mapped units. This connection is considered further in the methodological framework presented below.

1.4. Geospatial approaches for mapping loess-related deposits

Digitising and re-evaluating legacy geological cartography within a GIS environment is a well-established technique to extend point- and outcrop-based stratigraphy knowledge into a spatially continuous framework suitable for further analysis (Lagacherie, 2008). Field mapping and stratigraphic profiling remain the primary source of ground-truthed information on deposit genesis, age and internal structure, since pedosedimentary sequences observed in outcrops or soil pits can be correlated across sites using morphological, textural and chronological criteria (Cremaschi et al., 2015). However, since such field-based methods are inherently limited to point- or outcrop-scale observations, legacy maps compiled based on decades of prior field surveys provide a valuable, spatially extensive complement once their content has been digitized and georeferenced (Lagacherie, 2008).

Laboratory characterisation of samples collected in field is helpful in independently verifying and interpreting mapped units and is well supported in the literature. Laser diffraction particle-size analysis is a widely accepted technique used internationally for texture determination of sediment, and it has been in use for several years to characterize deposits and pedogenic horizons in Quaternary and soil studies (Callesen et al., 2018). Also, the ASD FieldSpec equipment provides data about reflectance spectroscopy in the field of VIS-NIR-SWIR, permitting analytical characterization in a rapid and non-destructive manner since some clay minerals along with carbonates and iron oxides show distinct absorption features in this spectral range (Clark, 1999). An established approach for identifying the dominant mineral phases in a sample is to compare measured spectra against reference libraries such as the USGS Spectral Library using the Spectral Angle Mapper (SAM) technique, specifically within the 2000-2450 nm regions where clay and hydroxyl-bearing minerals show their most diagnostic absorption features (Kruse et al., 1993; Clark,

1999). Particle-size and spectral-mineralogical characterisation of this kind are typically used in the literature as descriptive and interpretive evidence to support the identification and discussion of mapped units, which complement rather than replace spatial classification models (Clark, 1999).

As a covariate source for mapping surface soil and lithological properties, multispectral satellite imagery is widely used in the literature across broad areas that cannot be exhaustively field-sampled. This issue can be effectively addressed by using the Sentinel-2 ground observing system because it features many operating bands located in the visible, near-infrared, red-edge and shortwave-infrared spectrum with spatial resolution equivalent to 10-20 m and because its bands in the shortwave-infrared spectrum are considered significant in remote sensing and can detect clay, hydroxy mineral and iron oxide presence by means of unique band ratios (Pour et al., 2023). In view of the established fact that vegetation cover and soil moisture conditions are responsible for changing the spectral response of the soil and sediments below, it is appropriate to apply cloud filtering, temporal composites and bare soil masking with the help of the vegetation index which is recommended by the literature (Sadeghi et al., 2015).

Digital elevation models derive terrain attributes, which are similarly well establishd as covariates for representing the geomorphic controls on occurrence, preservation and reworking of deposit, since a substantial body of geomorphometric literature has demonstrated that variables such as slope, aspect, curvature and channel-related indices can differentiate depositional and erosional landscape positions such as terraces, alluvial fans and hillslopes (Moore & Burch, 1986; Desmet & Govers, 1996). As many terrain derivatives are mathematically related and therefore highly correlated with one another, it is recommended practice in the wider modeling literature to conduct a correlation-based screening prior to model development for reducing multicollinearity and improving the stability of the resulting statistical model (Dormann et al., 2013). The slope length-steepness (LS) factor which was originally developed within erosion-modelling research, is also used more broadly in terrain-analysis studies as a compound covariate, which summarises the combined influence of slope length and steepness on surface flow processes, independent of it specific application in estimation of soil-loss (Moore & Burch, 1986; Desmet & Govers, 1996).

One of the most widely applied supervised classification algorithms in remote sensing and digital soil mapping is Random Forest, mostly due to its ability to accommodate non-linear and correlated predictor relationships without the need for strict distributional assumptions (Belgiu & Drăguţ, 2016). Moreover, it is possible to conduct internal diagnostics because this equipment has variable importance measures that can be directly applied to the selection of important predictors (Belgiu & Drăguţ, 2016). The literature on statistical learning recommends permutation importance measures over impurity-based measures (e.g., Gini), since permutation importance is better able to measure the significance of the variables when they are correlated (Breiman, 2001; Strobl et al., 2008). Partial dependence tools (PDP) area a further established tool for diagnosis, which is used to visualise the marginal relationship between an individual predictor and the predicted outcome, helping to understand non-linear model behavior beyond a single importance ranking (Friedman, 2001). Whenever spatial data is used to derive training samples, the result is often autocorrelated, thereby the wider spatial-modelling literature recommends spatially blocked cross-validation, in which nearby sample locations are grouped together before being split into training and validation folds, as a way to avoid artificial inflation of accuracy estimates (Roberts et al., 2017).

The thesis draws on this body of established methodology to justify a combined approach in which the digitized legacy map, Sentinel-2 spectral variables and terrain variables derived from DEM are combined with a Random Forest classification framework, while particle-size and spectral-mineralogical laboratory analyses are used as complementary, descriptive evidence to support the interpretation of the mapped units. This combination reflects standard practice across the digital soil mapping, remote sensing and geomorphometric literature reviewed above, applied here to the specific problem to evaluate the spatial and spectral coherence of legacy loess-related map units under present-day conditions.

1.5. Research questions, aim and objectives

The overall aim of this thesis is to evaluate the potential of integrating a legacy Quaternary map, Sentinel-2 multispectral imagery and terrain derivatives within a Random Forest classification framework to improve the spatial characterisation of loess-related deposits

and legacy Quaternary units in the Piacenza sector of the Po Plain, using field-collected soil as an interpretive bridge to the original legacy cartography of Cremaschi (1987, 1990).

Research questions

- To what extent can Sentinel-2 multispectral imagery and terrain derivatives, combined within a Random Forest classifier trained on a legacy map, predict the spatial distribution of the legacy Quaternary units associated with loess deposits in the Piacenza sector?
- Which spectral and topographic predictors most effectively discriminate between loess deposits classes of different genesis, preservation state and degree of reworking?
- Does a classification model combining terrain and spectral predictors perform better than a model based on terrain predictors alone?

Objectives

The objectives of this thesis are:

- **To digitize, characterise, and interpret the legacy Quaternary map.**
  This includes georeferencing and digitizing the map of Cremaschi (1987) for the Piacenza sector, preparing labelled reference data for spatial analysis, and using field-collected soil samples and laboratory particle-size and spectral characterisation as an interpretive bridge connecting the original map units and their description in *Paleosols and vetusols in the central Po Plain* (Cremaschi, 1987) to the spatial classification results, rather than as direct inputs to the classification model.

- **To develop and compare terrain-only and combined terrain-spectral classification models.**
  This includes using a digital elevation model to derive terrain variables, and extract Sentinel-2 spectral bands and indices. Additionally, training a Random Forest classifier separately on terrain predictors alone and on terrain-plus-spectral predictors, and evaluating whether the combined model improves classification performance relative to the terrain-only model.

- **To identify key predictors and interpret their significance.**

  To assess which spectral and terrain predictors contribute most strongly to discriminating between mapped classes, interpreting these predictors in relation to the geomorphological and pedostratigraphic setting of the legacy units, and discussing the implications of the mapped distribution patterns for deposit preservation and potential surface reworking, considering possible erosion sensitivity as a contextual implication rather than as a principal thesis output.

2. Study Area

2.1. Location and general description

The study area sits in Piacenza Province, towards the western edge of Emilia-Romagna in Northern Italy, the area where the Po Plain, the Lombardy region and the northern edge of the Apennine chain all meet (Castaldini et al., 2019). Piacenza itself, the provincial capital, is situated at roughly 45°03′N, 9°42′E, just south of the Po River and close to where it meets with Trebbia (Provincia di Piacenza, 2016). The province is the westernmost of the nine provinces that make up Emilia-Romagna, which covers around 2,586 km² with Lombardy along its border to the north, Parma to the east, Liguria to the south and Piedmont along the western border (Provincia di Piacenza, 2016). In general, the province splits into two very different zones running north to south: a flat stretch up north that's part of the Po Plain and a hilly-then-mountainous southern two-thirds that increase gradually into the Apennines (Provincia di Piacenza, 2016).

The study area falls within low elevation portion of the Po Plain, generally under 100 metres above sea level and the city of Piacenza itself is situated at an average elevation of around 61 metres (Provincia di Piacenza, 2016). The land gives way to the Piacenza hills in the south, which are the first foothills belonging to the Ligurian Apennines, starting about 15 kilometres south of the city where the terrain first turns hilly (Provincia di Piacenza, 2016). Further south, the ground rises into proper ridgelines of Apennine, which reaches their maximum within the province at Monte Bue, at roughly 1,780 metres and marks the highest point in Piacenza Province (Provincia di Piacenza, 2016). This three-part shift, low-lying plain margin, then a belt of hills, then higher Apennine ridges, lines up with the broader morphostructural pattern already documented elsewhere along the boundary of Po Plain-Northern Apennines, where flat alluvial margins similarly give way to folded thrust-faulted marine sedimentary hills before climbing into more tectonically uplifted Apennine terrain (Bosino et al., 2019).

A well-developed fluvial network belonging to the Po River basin drains the Piacenza area, with the Po itself forming the principal drainage axis running west to east along the northern boundary of the study area (Castaldini et al., 2019). The main tributary rivers

draining the Apennine sector of the province follow a south-to-north directional flow before merging with the Po. The Trebbia River is the most prominent of these, which drains a good chunk of the northern Apennine relief west of the city of Piacenza (Provincia di Piacenza, 2016). Furthermore, minor watercourses i.e., the Nure torrent, drain the hilly and mountainous parts of the province and contribute to the dense and structurally influenced drainage pattern characteristic of the wider Po Plain-Apennine margin (Castaldini et al., 2019). Such a drainage network comprises of a morphological transition, from plain-to-mountain. This makes the Piacenza study area a landscape setting widely comparable to other well-studied sectors of the Po Plain Loess Basin along the Apennine margin, such as Oltrepò Pavese and the Ghiardo area, which share similar geomorphic and hydrographic characteristics relevant to erosion dynamics and preservation of loess (Cremaschi et al., 2015; Bosino et al., 2019).

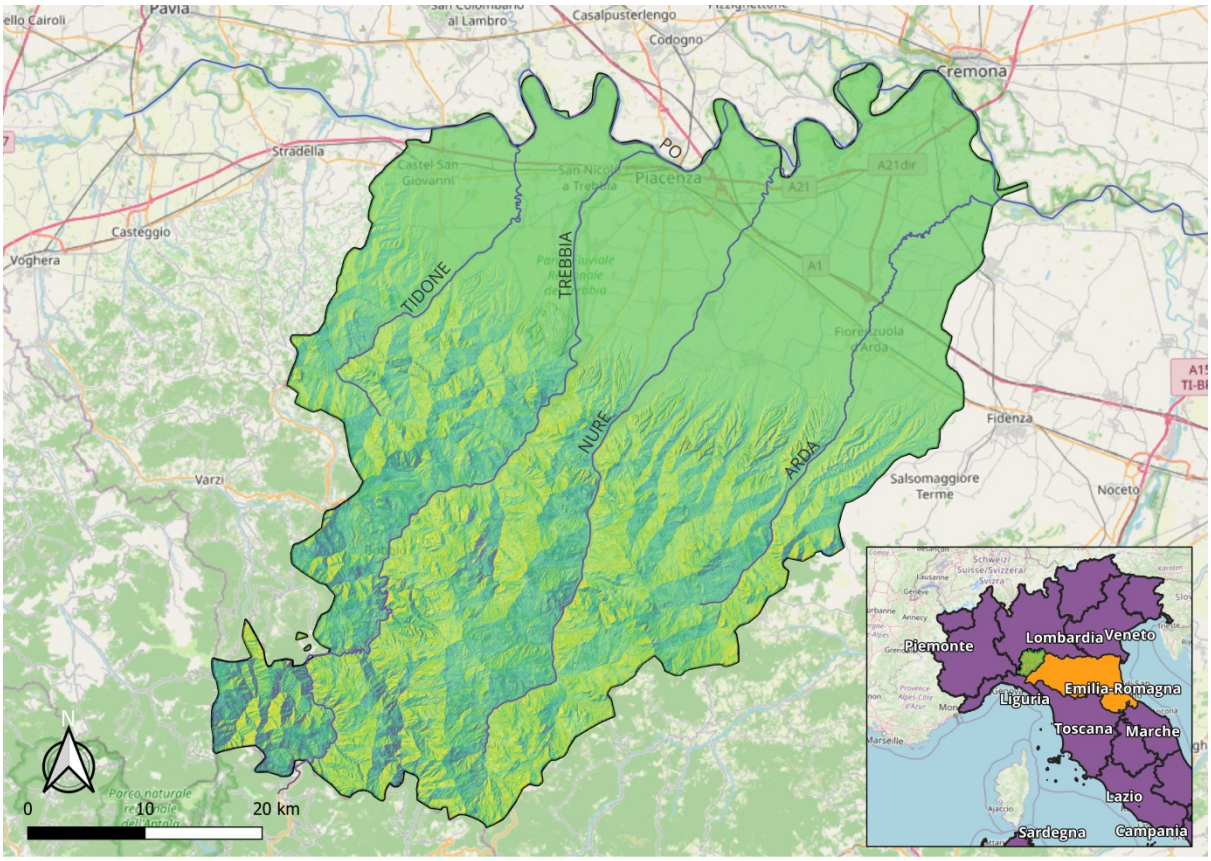


Figure 2.1: Location of the Piacenza study area at the boundary between the Po Plain and the Northern Apennines. The inset shows its position within northern Italy.

2.2. Geological Setting

The Piacenza sector of the Po Plain is situated within a syn-tectonic sedimentary wedge, filling the Pliocene-Pleistocene Apennine foredeep, and generating a basin by the activity of buried outer thrusts, which propagate in a north-eastern direction beneath the plain (Antonielli et al., 2016). In this area, the outcropping bedrock units belong mainly to the Messinian evaporites and the post-evaporite marine succession that are overlying, which comprises of the Tetto Formation, the Colombacci Formation and the ArgilleAzzurre Formation, all of which are sealed by Po Plain's Pleistocene continental deposits (Antonielli et al., 2016). The light blue clays and the overlying yellowish Imola Sands form the ArgilleAzzurre Formation, constituting the Lower Pleistocene substratum onto which younger Quarternary units were deposited across this margin (Andreetta et al., 2023). The base of the overlying Emilia-Romagna Super-Synthem is marked by an erosional unconformity, which is further divided into the Lower Emilia-Romagna Synthem (AEI) and the Upper Emilia-Romagna-Synthem (AES), which spans an age range from approximately 820,000 to 424,000 years before present for the lower unit and from 424,000 years before present to the recent for the upper unit (Andreetta et al., 2023).

The geological sequence of Piacenza Province has been described as having been deposited across marine, transitional and continental environments, with exclusively unconsolidated deposits (through locally cemented or densely packed) derived from the disaggregation of the rocky formations of the Apennine sector in the plain sector (Provincia di Piacenza, 2016). There are gravelly, sandy, silty and clayey materials present in these plain deposits, which are transported and deposited by Quarternary alluvial processes, forming the fluvial terraces and alluvial plains that have a strong presence in the northern part of the study area (Provincia di Piacenza, 2016). The morphological Apennine margin, which migrates progressively northeastward over time, is believed to have been stationary in its current position only from the Early Pleistocene onward, which marks the onset of the modern Quarternary depositional phase in this sector (Provincia di Piacenza, 2016). The so-called "Marine Quaternary Supersynthem" is corresponded by this later sedimentation phase, itself subdivided into three synthems (Qm1, Qm2 and Qm3) which were previously identified as Castell'Arquato Formation (Qm1) and the "Yellow Sands" (Qm2 and Qm3) on lithostratigraphic grounds (Provincia

di Piacenza, 2016). Above these units, the deltaic, marginal-marine and continental facies were developed, primarily dominated by fossiliferous sands and silts of Plio-Pleistocene transitional age, followed in the Early to Middle Pleistocene by gravelly, sandy, silty and clayey deposits of markedly variable composition, with a predominance of continental alluvial sedimentation (Provincia di Piacenza, 2016). Therefore, the current geological configuration that is observed across the province is the product of a complex sequence of marine sedimentation, uplift and emersion in the structure of the Apennine chain and subsequent alluvial infilling of the Po Plain beginning approximately 650,000 years ago (Provincia di Piacenza, 2016).

Soil-stratigraphic studies have identified two principal pedostratigraphic markers within this broader Pede-Apennine margin, that are used to constrain the timing of recent activity of tectonic plates: Collecchiopaleosol is an older, deep, reddish paleosol, associated with either the AES2 or AES3 sub-synthems, and a younger loess level that unconformably covers different underlying surfaces and hosts a distinct paleosol known as the Ghiardo Soil (Andreetta et al., 2023). Considering the continuity of the Pedo-Apennine Thrust system and the broadly consistent Quarternary stratigraphy from Reggio Emilia to Piacenza, the same loess level which lies over the Emilia-Romagna Synthem surfaces is expected to occur, in a comparably patchy and discontinuous form, across the Piacenza sector, which is consistent with the general distribution pattern described for loess bodies along the Po Plain margin on fluvial terraces, isolated hills and erosional surfaces (Costantini&Carnicelli, 2018).

A strong control is exerted by the lithological and mineralogical composition of the geological substrate on both erosion susceptibility and preservation of loess across this margin. The clay-dominated ArgilleAzzurreFormation and the associated fine-grained marine sediments underlying much of the Apennine foothill belt confer high inherent erodibility and low permeability to derived soils, such a combination favours concentrated erosion features and runoff generation on the surface once vegetation cover is reduced (Persichillo et al., 2017). Within the Quarternary marine, calcareous components are present and they contribute to the formation of calcic soil features and influence soil structure and aggregate stability along with continental units, these factors further modulate the resistance of loess-derived soils to detachment by precipitation and downhill water movement (Bordoni et al., 2019). Since, loess itself is a poorly cemented,

friable, silt-dominated structure, its susceptibility to erosion is compounded when it directly overlies or is reworked into these clay-rich parent materials, since the combination of a loosely structured surface mantle and a low-permeability, erodible substrate creates conditions that are specifically conducive to sheet, rill and badland (calanchi) erosion on steeper slopes of the Pedo-Apennine margin (Bosino et al., 2020).

2.3. Geomorphological setting

The transition between the low-relief Po Plain and the more dissected foothills and ridges of the Norther Apennines is occupied by the Piacenza study area, which forms part of the Pede-Apennine margin where continental deposits of the foredeep basin lies next to the Apennine chain (Castaldini et al., 2019). The characteristic features of the Po Plain sector is a gently sloping, low-gradient surface (the Po Plain Main Level) cut by different orders of fluvial terraces that record Late Pleistocene and Holocene incision and aggradation along the main trunk river and its tributaries (Castaldini et al., 2019; Zuffettiet al., 2018). Close to the Apennine boundary, this plain surface is interrupted by systems of coalescent fluvial fans that develop at the Apennine foothills. Thus, Later Pleistocene bajada are formed related to the large sediment supply generated under Last Glacial Maximum conditions (Castaldini et al., 2019). Moving south, the relief rises into low terraces and gentle hills that mixes upwith alluvial fans, ultimately giving way to steeper Apennine slopes and ridges incised by valleys aligned moreover perpendicular to the structural grain of the mountain front (Castaldini et al., 2019; Conti et al., 2020).

The Po River dominates the regional drainage network, which flows from west to east across the middle of the plain, additionally numerous transverse tributaries drain the Alpine and Apennine chains into the foreland basin (Castaldini et al., 2019). Watercourses reaching the plain have built up alluvial fans at the Apennine margin that extend northwards and these fans coalesce to form broad depositional aprons beneath the foothills (Castaldini et al., 2019). The foothills belt and adjacent Apennine slope's relief is strongly dissected, with valley systems incised into lithologies rich with clay and marl that favour the development of steep slopes, headwater hollows and localised structural terraces (Bosino et al., 2019, Conti et al., 2020). This configuration of geomorphology i.e., gently sloping main plain surface, fluvial terraces, coalescent fans at the margin and

dissected hillslopes and valleys upslope is typical of the Po Plain-Northern Apennines border and provide the framework for morphology structure within which loess bodies and associated erosion processes are represented (Zuffetti et al., 2018; Zerboni et al., 2015).

In general, loess bodies in the Po Plain are tiny and discontinuous, often draping older glaciofluvial or alluvial surfaces and polygenetic paleosols developed in a variety of parent materials, specifically where topographic obstacles interrupt the low-gradient plain surface (Zerboni et al., 2015; Zuffetti et al., 2018). Such topographic obstacles are invariably associated with the thickest loess deposits in the basin – terraces along the Alpine and Apennine margins and isolated hills within the plain – which traps sediment in cold, dry, windy glacial conditions and later preserve complex sequences of loess-paleosol at their summits (Zerboni et al., 2015; Ferraro, 2009). In the southern Po foredeep, pedostratigraphic work on isolated tectonic reliefs has shown that loess-paleosolsequences are best preserved on stable paleo-highs uplifted during thrusting phases, while intervening structural lows experience valley incision, terracing, soil truncation and redeposition, which emphasizes the role of geomorphology in modulating both reworking and preservation of loess deposits (Zuffetti et al., 2018).

In this context, the primary units of geomorphology in the Piacenza study area - fluvial terraces, coalescent alluvial fans at the margin and dissected hillslopes and valleys systems in the foothill belt – jointly condition the presence and vulnerability of loess deposits (Castaldini et al., 2019; Zerboni, 2018). Loess mantles draping terraces, fans, and isolated hills are specifically prone to erosion where steep slopes, sparse vegetation and substrates that are rich in clay coincide, which favours the development of gullies, dry valleys and calanchi, which in turn become primary conduits for export of sediment from loess landscapes (Bollati&Zerboni, 2021; Bosino et al., 2020). Therefore, it is fundamentally important to understand the spatial arrangement of these geomorphological units and their associated drainage and slope features for both mapping loess distribution and assessing erosion hazard in the Piacenza area (Zerboni, 2018; Bosino et al. 2020).

2.4. Climate

According to the Köppen system, the climate of the Piacenza territory is classified as a temperate warm climate of type “C”, which is characterised by mean temperatures of the coldest month ranging between −3°C and +18°C (Provincia di Piacenza, 2016). The plain and hilly sectors of the study area show a temperate sub-continental climate within this broad classification, with mean annual temperatures ranging between 10°C and 14.4°C, mean temperatures of the coldest month around −1°C and +3.9°C, one to three months which exceeds a mean temperature of 20°C and a yearly thermal range greater than 19°C (Provincia di Piacenza, 2016). The sector of the province accommodating the Apennine mountain is characterised by a cooler temperate climate, with mean annual temperatures between 6°C and 10°C, mean temperatures of the coldest month between 0°C and +3°C and mean temperatures of the warmest month around 15°C and 20°C (Provincia di Piacenza, 2016). In a broader sense, the city of Piacenza itself is mentioned in regional climatological records as having a humid subtropical climate with no separate dry season, which corresponds to the Köppen subtype "Cfa”, with hot and sultry summers (Provincia di Piacenza, 2016).

Based on averages calculated over the 1940-2025 period, Piacenza’s long-term climate records indicate a mean annual temperature of approximately 13.0°C and mean annual precipitation of approximately 980 mm (Piacenza climate normals, 2026). In the wider Po River basin, mean annual precipitation is estimated at approximately 1000-1200 mm, with a complex pattern of spatial precipitation subdivided into distinct regimes across the basin (Wani et al., 2025). Piacenza is situated within the central plain sector of the basin and falls under the “sub-littoral Padano” precipitation regime, characterised by an equivalent bimodal distribution with two rainfall peaks during the year (Wani et al., 2025). This bimodal pattern is supported by the official characterisation of climatology of the Piacenza territory, which describes a typical “sub-littoral” Apennine or Po Plain pluviometric regime which features two maxima in a monthly precipitation, occurring in spring and autumn, and two minima, which occurs in winter and summer, with the autumn maximum and summer minimum being the more pronounced of the two pairs ((Provincia di Piacenza, 2016). An intense autumn rainfall peak follows this seasonal structure, which is marked by a pronounced late-summer rainfall deficit, is characteristic

of the broader Po Plain-Apennine climatic transition and has direct relevance for erosion dynamics, since intense autumn storms follows periods of summer drought thus creating conditions conducive to surface crusting, reduced vegetation cover, and subsequent high-intensity runoff and erosion when rainfall resumes (Provincia di Piacenza, 2016).

As per the latest climatology analysis of the Po River basin and Northern Italy, there has been a statistically significant increase in mean temperature over recent decades, even where corresponding trends in total precipitation remain feeble or spatially inconsistent (Mombrini et al., 2025). At the same time, several independent studies converge on the finding that, although total annual precipitation in the Po Valley has shown a declining trend since long-term, with some assessments measuring a reduction of the order of 20 percent over the past decades, the intensity of extreme precipitation has been increasing in this region, with the Po Valley and Upper Adriatic identified as the Italian areas where this contrast between declining totals and intensifying extremes is most pronounced (Caporaliet al., 2020; Amadio, 2013). Consistently, an overall intensification of short-duration heavy rainfall events is reported by analyses of daily and sub-daily precipitation extremes across the wider Po River district, albeit with spatially uneven patterns across the basin (Tanda et al., 2025). In the Po Valley, the 2022 drought event has further shown to be unprecedented in the past two centuries and to form part of a longer-term trend toward increased frequency and episodes of drought severity, specifically over recent decades (Mombrini et al., 2025).

This integration of rising temperatures, a tendency leading to more frequent and severe drought periods, and an intensification of extreme events of rainfall, even where there is uniformity or decline in total annual precipitation, is particularly relevant for erosion hazard in loess and landscapes that are rich in clay such as the Piacenza area, since prolonged dry spells reduce soil cohesion and vegetation cover, while subsequent rainfall episodes of high-intensity produce disproportionately large amounts of surface runoff and detachment of sediment (Caporaliet al., 2020; Provincia di Piacenza, 2016). Considering that loess itself is a friable, silt-dominated structure and highly erodible once its natural cohesion is disturbed by drying and cracking, this emerging climatic pattern of “less frequent but more intense” rainfall is expected to cause erosional processes i.e., sheet, rill and gully across the exposed and reworked loess bodies of the Piacenza sector in the coming decades.

2.5. Soils

In the past, researchers have explored the micromorphology of middle Pleistocene paleosols in the Northern Italy, which gave insights about the long-term soil formation processes in the region. Also, various pedogenic units were identified in the study that represented different stages of soil development, suggesting that the contemporary soils found in the region likely overlier older pedogenic horizons (Kühn et al., 2006).

The soils present in the Piacenza area, situated at the transition between the Po Plain and the Northern Apennines, show an A-B-C horizon sequence, although the degree of development and the horizon differentiation differs depending on the topographic position, parent material and the history of land management (Bordoni et al., 2019). Truncated profiles with minimum horizons are developed on the steeper slopes due to accelerated erosion, whereas in the valley floors and gently sloping hillsides fully developed pedogenic profiles are described (Bordoni et al., 2019). According to the World Reference Base for Soil Resources (WRB) classification system, the soils in the region are classified as Cambisols, Luvisols, Vertisols and Regosols (ERSAF, 2024).Cambisols are characterised by a cambic (Bw) horizon, which shows evidence of structural development and moderate weathering without significant illuviation of clay, are usually found on moderate slopes where erosion and deposition remains comparatively balanced, which allows enough time for horizon differentiation without excess truncation (Nachtergaele, 2017; Schad, 2023). A diagnostic horizon sequence of Ah-Bw-C is displayed by these soils, which reflects alteration of the parent material through oxidation, structural aggregation and moderate weathering while retaining sufficient similarity to the substrate lying below to be distinguished from one intensely developed profile (Schad, 2023).

In Northern Italy, Luvisols represent the diagnostic soil type that is most closely associated with loess and loess-derived parent materials (Schad, 2023). In this horizon, there is an increase in clay content as compared to the overlying A horizon due to the translocation (illuviation) of the fine clay particles from upper horizon (Bordoni et al., 2019). Clay coatings (clay skins or argillans) on ped surface and lining pore spaces were

revealed in microscopic examination, providing evidence of clay translocation (Morelli et al., 2025). The increased storage of clay leads to higher bulk density, which can reduce water movement and root penetration, especially when agricultural machinery has compacted the horizon (Bordoni et al., 2019). Luvisols that have well-developed argic horizon are associated with older and more stable geomorphic surfaces where long-term pedogenesis has resulted in clay migration and accumulation (Morelli et al., 2025).

A decisive control on erosion susceptibility is exerted across the Piacenza-type Apennine margin by the interaction between soil properties, slope and land use. A horizons with fine-textured, which is dominated by silty-clay or clay-loam material derived from Tertiary marine sediments, are vulnerable to compaction by agricultural machinery and resulted in reduced organic matter content under conventional tillage, both of which leads to decline in structural stability and increase in vulnerability to surface erosion (Bordoni et al., 2019).On steeper slopes, accelerated erosion generates truncated profiles of soil with minimal development of horizon, which exposes less weathered B or C horizon material at the surface, whereas profiles that are fully developed are preserved only on valley floors and terrains with gentle slopes where erosion and deposition remain in approximate balance (Bordoni et al., 2019). An equal strong influence is exterted by land use: vineyard managed with intensive tillage and bare inter-rows have proven to be comparatively more prone to shallow slope failure and surface erosion than vineyards that are maintained with permanent grass cover in the inter-rows, since mechanical and hydrological reinforcement is provided by root systems of cover vegetation that increases the critical slope angle at which failure occurs, i.e., from approximately 21-25 degrees for tilled vineyards to 28-33 degrees for vineyards with permanent grass cover or woodlands (Bordoni et al., 2019). Considering that Luvisols derived from loess and associated Cambisols in this setting combine inherently erodible silty textures with subsoils enriched with clay that are prone to compaction and reduced permeability, their erosion resistance is strongly affected by the presence or absence of protective vegetation cover, which reinforces the rationale for assessing erosion hazard jointly through soil, terrain and land-cover parameters (Bordoni et al., 2019; Bosino et al., 2020).

2.6. Land use and vegetation

The Piacenza study area comprises of a land-use mosaic characteristic of Northern Italian Apennine landscapes, which is dominated by a combination of intensive arable cultivation in the plain area and viticulture, mixed cropland, grassland, and forest cover across the mountainous zones (Malandra et al., 2018). One of the most widespread and economically important perennial land uses are represented by the vineyards on the hill slope of this Apennine margin, in alignment with regional patterns documented across comparable Northern Italian areas of wine production such as the Oltrepò Pavese, where viticulture constitutes the dominant hillslope land cover (Bordoni et al., 2019). According to a meta-analyses of land-use change over the past seventy years at the broader Apennine scale, there is long-term trend of cropland contraction, with an average decline of approximately 49 percent, along with a reduction in grassland and pasture of around 19 percent and a marked expansion of forest cover of nearly 78 percent, which is driven mainly by abandonment of agricultural practices in margin and steep terrain (Malandra et al., 2018). Complex and counterproductive environmental outcomes have been produced as a result of this abandonment-driven forest expansion, since land abandonment followed by unmanaged natural reforestation has been associated with net decline in overall environmental quality in several case studies in Central Apennine, which includes measurable increases in soil degradation despite gains in carbon sequestration (Marchetti et al., 2025).

A decisive influence on erosion susceptibility is exerted by vegetation cover across this landscape, with the presence or absence of permanent ground cover which represents the most important management-related determining factor of soil loss in agricultural lands on slopes (Biddoccu et al., 2020). Across multiple wine-growing regions in Europe, comparative erosion monitoring has showed that permanent cover crops account for the most effective soil-protection measure for attaining sustainable erosion rates, and a fourteen-year monitoring experiment in Northern Italy found that the conversion from conventional tillage to permanent grass cover has reduced average annual soil loss by an order of magnitude, from approximately 13.85 t ha^{-1} yr^{-1} (tilled management) to approximately 1.8 t ha^{-1} yr^{-1} (permanent grass cover), which corresponds to a 74-91 percent reduction in erosion (Biddoccu et al., 2020). At the european scale, perennial

crops such as vineyards have been identified as having the highest average soil erosion rates among all land uses, which accounts for approximately 9.47 t ha^{-1} yr^{-1} and roughly 10 percent of total soil losses across Europe, underscoring the specific vulnerability from erosion of vineyard-dominated hillslopes such as those found in Piacenza appenine margin (Schütte et al., 2022). Further studies on complementary plot-scale confirmed that soil compaction and erosion in vineyard inter-rows are caused mainly by the presence and persistence of vegetation cover rather than by the specific botanical composition of that cover, since, bare, tilled inter-rows consistently shows comparatively higher compaction and erosion than vegetated inter-rows regardless of species mixture (Pornaro et al., 2022).

In terms of specific crops and land management practices relevant to erosion risk, several tillage and vegetation management systems have been documented across Italian vineyard landscape within direct implications for soil conservation. In the past, the dominant practice for weed control and soil aeration used to be theconventional tillage of the vineyard inter-row, which showed increased erosion rates compared to any form of permanent or seasonal ground cover, and repeated disturbance in soil from tillage further degrades the structure of soil and organic matter content over time (Pornaro et al., 2022; Biddoccu et al., 2020). As a counter-measure, the adoption of permanent grass cover or sown cover-crop mixtures between vine rows has become an increasingly popular conservation practice in Northern Italian viticulture, shown to reduce loss in soil organic carbon caused by erosion while simultaneously improving water infiltration and aggregate stability (Pornaro et al., 2022; Biddoccu et al., 2020). The selection of species for cover crops has also been shown to affect the effectiveness of erosion control, with persistent, low-growth-rate grass species such as tall fescue (*Schedonorus arundinaceus*) which provides particularly high and stable protection against soil erosion throughout the year in comparison with less persistent mixtures that are susceptible to weed invasion (Pornaro et al., 2022). In vineyard systems on steep-slope, cultivation practices such as planting rows across the slope (contour orientation) and, where feasible, terracing have been employed particularly to mitigate surface erosion and reduce the risk of slope failure triggered due to intensive soil disturbance during establishment of vineyard and mechanised cultivation (Guidoni et al., 2012).As a whole, these region-specific findings on land use, vegetation cover and management practices indicate that erosion hazard

across the hillslopes dominated by vineyard and cropland in the Piacenza Apennine margin is likely to vary substantially based on the local prevalence of bare or tilled soil versus permanent vegetative cover. This relationship is directly relevant to interpret land-cover related erosion hazard patterns in this thesis (Biddoccu et al., 2020; Schütte et al., 2022).

2.7. Erosional processes in the study area

The Piacenza are is affected by different kinds of erosional processes in the Northern Apennine margin, which includes sheet and rill (interrill) erosion, development of gully, formation of badland (calanchi) and shallow landslides triggered by rainfall, all of which are strongly conditioned by Plio-Pleistocene marine substrate - rich in clay - that characterizes this part of the Apennine foothill belt (Regione Emilia-Romagna, 2024).Badlands are locally known as *calanchi*, which are characteristic erosional landforms spread across Piacenza's foothill zone, where grey-blue Pliocene marine clays outcrop and give rise to steep, bare slopes dissected into narrows valleys by rill-wash erosion and further separated by thin crests, commonly organised in herringbone, radial or parallel-line patterns(Regione Emilia-Romagna, 2024). These badland basins are documented and explicitly include areas within the Piacenza territory to cover extensive areas in several valleys of the Emilia Apennine, and are locally exemplified in gully systems such as those observed along the Stirone torrent, where deep-sea clayey sediments form a complex tangle of furrows and steep, cause accelerated erosion on bare slopes (Regione Emilia-Romagna, 2024). Two interacting factors determine this morphology of gully; the clayey nature of the geological substrate and the erosive action of rainfall on this poorly cohesive material, a combination which is directly analogous to the erosion susceptibility mechanisms in the neighbouring Oltrepò Pavese portion of the Northern Apennines documented for calanchi and rill-interrill erosion (Parco RegionaledelloStirone e del Piacenziano, 2011; Bosino et al., 2020).

In addition to badland and gully erosion, the Piacenza area, together with the adjacent Parma sector is highly susceptible to rainfall-driven shallow landslides and earth flows, representing the most widespread kind of mass movement in this part of the Northern Apennines (Panizza &Piacente, 2008). Substantial amounts of rainwater or spring water

can be absorbed in this setting by clayey soils until they reach a plastic or liquid consistency, which generates earth-flow bodies that can extend for several kilometers along the slope (Panizza &Piacente, 2008). In the Piacenza and Parma provinces, documented debris-flow events have been linked to intense, short-duration rainstorms, with one well-characterised event triggered by rainfall peak on hourly basis exceeding 80 mm and even durations of approximately six hours in the Piacenza portion, which produces 113 debris flow, 89 debris slides, four mudflows and 29 features of bank-erosion across a survey area of roughly 350 km² spanning the catchments of Trebbia, Nure and Aveto (Ciccarese et al., 2016). These findings closely align with the extensively studied rainfall-landslide relationships established for the neighbouring Oltrepò Pavese, where shallow landslide occurrences are predicted byempirical and physically based rainfall thresholds based on antecedent pore-water pressure and cumulative event rainfall, with rainfall events of 30-134 mm cumulated over four to 105 hours triggering widespread slope instabilities during the wet season (Bordoni et al., 2019). Considering the comparable clay-rich lithology, rainfall regime and land use on hillslope (including vineyard and mixed agricultural cover) shared between Piacenza and the Oltrepò Pavese sector, rainfall-triggering mechanisms of similar magnitude for shallow landslides and debris flows can reasonably be expected to occur across the Piacenza study area(Ciccarese et al., 2016; Bordoni et al., 2019).

In regards to this thesis, the loess bodies occurring on the terraces, isolated hills and hillslopes of the Piacenza sector are the most critical implication of these regional erosion patterns and are likely to be exposed to the same combination of sheet, rill and gully erosion, badland development and shallow mass movement documented for the wider clay-dominated margins of Apennine, particularly where loess directly lies over or is locally reworked into erodible Plio-Pleistocene clay formations (Regione Emilia-Romagna, 2024; Bosino et al., 2020) .This convergence of a friable, silt-dominated surface mantle with and inherently unstable, clay substrate with low-permeability, combined with a rainfall regime prone to short, high-intensity storms, provides the process-based rationale to evaluate the erosion hazard across the loess landscape of Piacenza using an integrated framework of parameter based on terrain, soil and land-cover, consistent with the maximum-entropy and terrain-based susceptibility modelling

approach already validated for calanchi and rill-interrill erosion in the analogous setting of Oltrepò Pavese (Bosino et al., 2020).

3. Material and Methodology

3.1. Overall Workflow

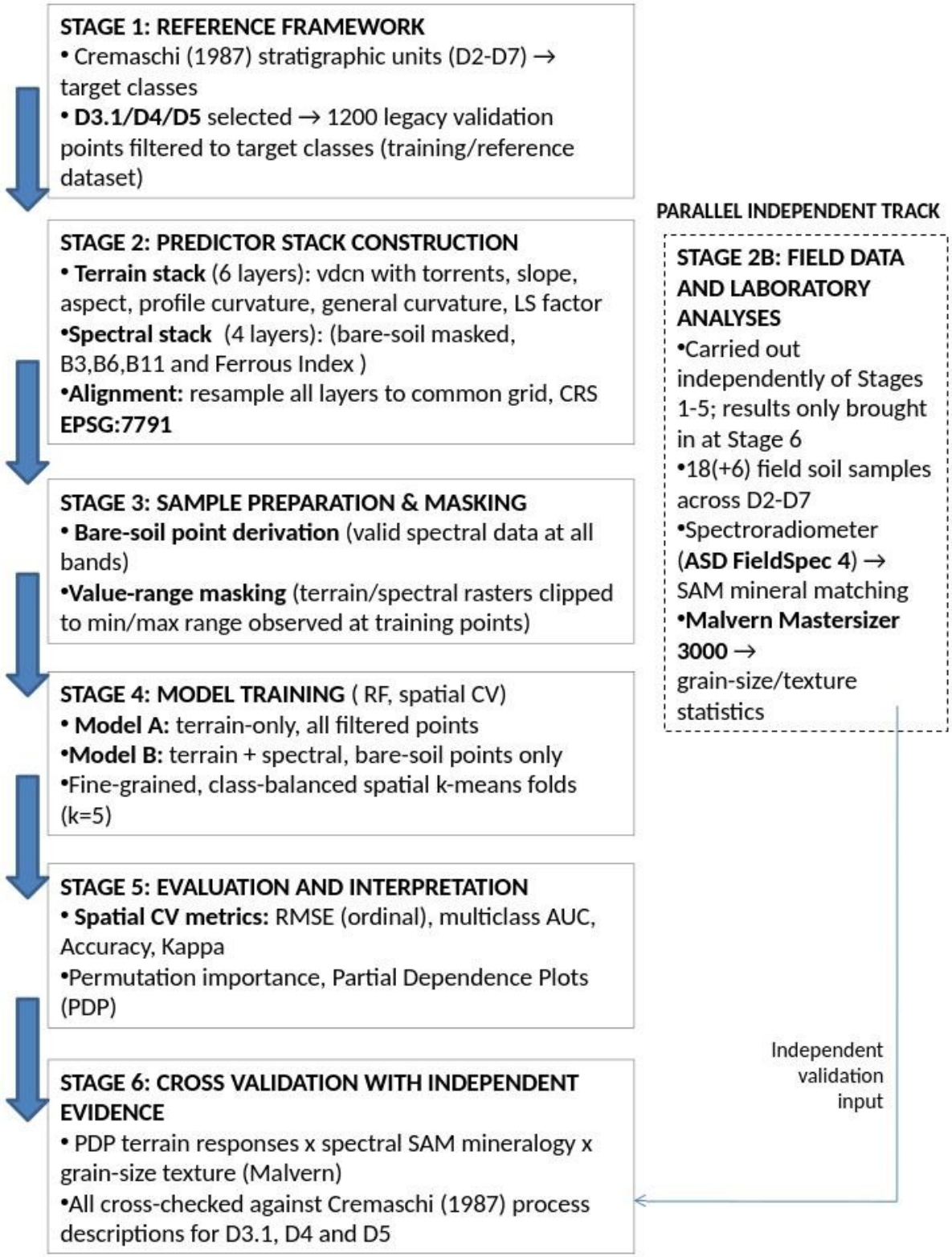


Figure 3.1: Diagrammatic representation of methodological workflow of this thesis.

The work carried out in this thesis followed a sequence of stages, as summarised in Figure 3.1 above and expanded on section by section for the remainder of this chapter. The starting point was not the data itself but the classification scheme used to label it: the stratigraphic units defined by Cremaschi (1987) for the loess sequence in Po Plain were adopted as the reference framework against which everything else in this study is evaluated and three of these units – D3.1, D4 and D5 as mentioned in Table 1.2 – were selected as the specific classes to be modelled due to the presence of loess cover in these units. A larger dataset covering the study area was then filtered down to these three classes, which forms the reference dataset used throughout the modelling stages that follow (Stage 1).

Alongside this, a separate and independent dedicated fieldwork was conducted to collect soil samples from across the full range of stratigraphic units within the study area (D2 through D7), which were later analysed in the laboratory for their spectral reflectance and particle-size properties (Stage 2b in Figure 3.1). The results of the laboratory work are only analysed much later at the point where the statistical model outputs are checked against independent geological evidence and is not used during the modelling or training of either classifier.

With the reference classes established, the next task was to build a set of spatial predictor layers capable to distinguish between them (Stage 2). This meant to assemble two separate stacks of raster data: a terrain stack derived entirely from a digital elevation model, covering variables such as slope, aspect, curvature, distance to the drainage network and the LS factor and a spectral stack built from satellite-derived bands and indices, but restricted only to locations identifiable as bare soil, since vegetation cover would otherwise mask the reflectance signal that the spectral variables depend on. Furthermore, another preparatory step (Stage 3) checked which of the points from the legacy units actually fell on usable, non-masked spectral data and applied a value-range mask so that models would only be asked to predict within the range of conditions actually represented in the training data, rather than extrapolating into unfamiliar ranges.

From there, two separate Random Forest classifiers were trained (Stage 4): one using only the terrain variables and a second using terrain and spectral variables together but restricted to the bare-soil subset of points. Training was carried out under a spatially structured cross-validation scheme rather than a simple random split, since points that are close together on the ground tend to share very similar characteristics purely by the tendency of their proximity

and ignoring this can make a model look far more accurate than it would actually be on genuinely new locations (Roberts et al., 2017). The output of both models were then evaluated in several complementary ways (Stage 5): through standard classification metrics computed out-of-fold, through permutation importance and partial dependence plots to see to the ranking of variables on which the models were actually relying on and how (Meyer & Pebesma, 2021).

The final stage (Stage 6) is where the two separate tracks – the statistical modelling on one side and the laboratory analyses on the other are finally brought together. Instead of just treating the model outputs as a self-contained result, the patterns identified through partial dependence and variable importance were compared against the mineralogical evidence from the spectroradiometer samples, the grain-size evidence from the Malvern texture analysis and process descriptions given in Cremaschi's (1987) original stratigraphic work. This final stage allow the discussion chapter to ask not just whether the models perform well statistically, but do they perform the way that makes geological sense.

This overall structure is an established classification framework which feeds a modelling pipeline, broadly follows the logic of a standard digital soil mapping workflow in which environmental covariates are linked to point-based reference data to produce spatial predictions that are then assessed for both accuracy and plausibility against field evidence (McBratney et al., 2003). Simultaneously, an independent fieldwork was conducted and it converges with the results of the modelling pipeline at the very end. The following sections work through each of these stages in turn.

3.2. Reference Framework: Cremaschi (1987) Stratigraphic Classification

3.2.1. Rationale for adopting Cremaschi's units as the reference classification

A taxonomic classification tells us what a soil looks like at the time it is sampled, largely independent of how it got that way or where it happens to be positioned in the wider landscape. Cremaschi's scheme works differently: each unit is defined mainly by its place in a reconstructed sequence of depositional, erosional and pedogenic events, which are tied to a specific chronology and a certain position within the Apennine fringe of the Po Plain

(Cremaschi, 1987). This align with what is commonly known as pedostratigraphic approach by soil geomorphologists , where soils and their associated deposits act as markers of relative age and landscape history rather than being classified just on the basis of their own morphology (Birkeland, 1999). Considering that the aim is to model how well a surface is preserved or disturbed (intact loess cover, cover removed by erosion or an older horizon buried underneath), thereby a scheme based on process and relative age suited the problem better than a purely descriptive classification.

On a practical note, Cremaschi's units were mapped and described from field profiles across the same physiographic setting this thesis works within, so the class definitions are not something imported from a different location and then forced onto this study area – they are based in the same geological system that the terrain and spectral predictors are actually sampling. Keeping the modelling target connected to the same literature that is later used to understand the results (Section 4) avoids a translation step between an external taxonomy and the stratigraphy of a specific region that ultimately explains the observed patterns.

3.2.2. Description of target units – D3.1, D4 and D5

Among the units presented in the Apennine fringe as per Cremaschi, loess cover was present in D3.1, D4 and D5, which is the reason why these units were selected, taken together and they represent three genuinely different kinds of landscape history: one unit that has stayed buried and largely undisturbed since it formed, one that represents an infill event within a pre-existing valley and one that represent the outright removal of material rather than its accumulation. Each is described below in terms of age, whether the material is in place or has been eroded and reworked, and its oxidation and weathering status, all sourced from Table 1.2 (Cremaschi 1987).

D3.1

This unit is the buried paleosol – specifically a vetusol, which means a deeply and maturely weathered profile – that developed in the top of the Pede-Apennine formation, and it is the same unit Cremaschi (1978, 1982) named the Collecchio paleosol after the area where it was first documented (Cremaschi, 1987). Since it is formed on the top of the older formation and is later buried beneath the loess described below, its age is within the Middle Pleistocene, which predates everything that comes to rest on top of it. In terms of whether the material is

in place or reworked, D3.1 is unambiguously an in-situ profile: the sequence of horizons Cremaschi (1987) describes is coherent from top to bottom, with the kind of internal consistency you would expect from a soil that formed exactly where it now lies, rather than one that has been picked up and redeposited somewhere else. Its status of oxidation and weathering is really what sets it apart as the profile shows strong rubefaction – the reddening that comes from accumulation of iron oxide over long periods of well-drained weathering – together with thick ferri-argillan coatings, essentially built-up skins of iron and clay on the faces of soil structural units, a feature that only really develops through sustained in-situ pedogenesis (Cremaschi, 1987). In profiles where the parent material contained ophiolitic rock fragments, content of free iron reaches to unusually high values, though Cremaschi (1987) is careful to attribute this specifically to the parent material's lithology rather than to an especially long weathering history at those particular sites – which is a distinction to keep in mind before treating free-iron content as a simple stand-in for age.

D4

This unit corresponds to the Borzano gravels, described by Cremaschi (1987) as poorly bedded or discontinuously planar-bedded gravel deposits, with occasional sand lenses and toward the top of the sequence, lenticular pelitic bodies. These are interpreted as braided-river deposits and they particularly occupy valleys cut into the older fluviatile formation of Pedo-Apennine, sometimes completely infilling them (Cremaschi 1987). No absolute data is available on its own for this unit, but its position of stratigraphy – sitting in valleys incised into a formation already established as Middle Pleistocene – places it within that same period. Process-wise, D4 is depositional rather than in-place weathered material, though it is worth being precise about the kind of deposition: it is fluvial infill of a pre-existing valley, not the aeolian loess that later covers it. That loess sheet is known as the Ghiardo loess, which is a separate and later-forming unit – a polygenic aeolian cover roughly one metre thick, made up of at two phases of deposition, which systematically overlies the Borzano gravels (D4), the fluviatile formation beneath D3.1's paleosol and the erosional surface described next as D5 (Cremaschi, 1987). At the base of this loess occurs an Acheulean lithic industry, dating its onset to the end of the Middle Pleistocene (Cremaschi, 1987) – which means D4 itself is somewhat older than loess draping it, even though both are conventionally grouped together as "loess-covered" in field mapping. Cremaschi's own cross-section of the Borzano terrace additionally records a fine-textured sediment layer which sits directly on top of the gravel, immediately below the loess – a detail that matters for interpreting any near-surface sample

taken at a D4 location, since it could plausibly represent the gravel, this intervening fine-textured layer or the loess cap itself, which depends on exactly how deep the sample was taken. On oxidation, D4's own gravel body is not separately characterised by a strong weathering profile in the way D3.1 is; whatever pedogenic development shows up in near-surface samples at D4 locations more likely reflects the loess cover which sits on top of it than the gravel itself.

D5

In a fairly fundamental sense, this unit is the odd one out among the three: it is not a depositional or in-place weathering profile at all, but an erosional surface – described as a piedmont glacis, produced when the older Pede-Apennine fluviatile formation, already folded, faulted and titled by tectonic activity, was subsequently planed down by erosion (Cremaschi, 1987). According to the chronology, this places D5 in the Middle Pleistocene as well, prior to the deposition of the Ghiardo loess that later covers parts of it – consistent with, rather than contradicting, D4's own Middle Pleistocene age, since both predate the same later loess event. In the terms asked for here, D5 is the one unit among the three genuinely defined by material being removed from the landscape rather than accumulating or weathering in place – a "washed away" surface rather than an in-place or newly deposited one. On oxidation status, Cremaschi (1987) does not separately describe a lithology or pedology for D5 at all, since the unit is defined purely by the erosional process rather by a depositional or weathering characteristic of its own. Any oxidation or mineralogical signature observed for this class in the fieldwork of the present study should therefore be considered as this thesis's own empirical finding rather than something already confirmed in the original literature.

3.2.3. Context classes – D2, D6 and D7

D3.1, D4 and D5 were not picked in isolation and is part of a broader unit sequence, sitting at a specific point along a longer chronology running from the oldest unit to the youngest as mentioned in Table 1.2 (Cremaschi 1987).

D2, together with D1, corresponds to the Pede-Apennine fluviatile formation as a whole (the same unit that D3.1's vetusol and D4's valley-fill gravels are both cut into or developed upon) and represents gravelly, sandy, silty and clayey continental deposits which spans across several fluvial facies, dated to the end of the Early Pleistocene through the beginning of the

Middle Pleistocene on paleomagnetic grounds (Cremaschi, 1987) – which makes it the oldest unit in the sequence and one that consist of no loess cover of its own. D6 and D7, by contrast are both younger than the three modelled classes: D6 corresponds to the Cavriago gravels, which is a Late Pleistocene piedmont alluvial fan deposit with only a thin, weakly rubefied soil at its surface, while D7 is overall the youngest unit, which consist of Holocene alluvial plain sediments that, in strongly subsiding areas, bury the southern margins of the D6 fan (Cremaschi, 1987). Neither D6 nor D7 carries a loess cover. Seen together the sequence runs from an old, non-loess-covered fluviatile formation (D2), through a phase in which a buried paleosol formed on top of it and a nearby valley was infilled with gravel (D3.1 and D4), through a separate erosional interruption of that same older surface elsewhere in the landscape (D5), all three of which where later covered by the same Ghiardo loess and finally to younger, non-loess alluvial fan surfaces with progressively less-developed soils (D6, then D7) as the sequence approaches the present.

3.3. Predictor Variables

3.3.1. Conceptual framework: why terrain and spectral variables?

A useful way to think about this comes from the framework of SCORPAN, which frames the prediction of a soil property or soil class as a function of soil, climate, organisms, relief, parent material, age and spatial positions, taken together (McBratney et al., 2003). Measuring ever one of these factors is not practical at the scale of this thesis, but two of them map quite naturally onto the data actually available here. SCORPAN framework has received validation from terrain characteristics as far as relief context is concerned because of the importance of the contour of the land surface in determining movement of hot water, sediment and weathering materials over it (McBratney et al., 2003). On the other hand, spectral indices can be used as proxy for the parent material and surface soil properties because the reflectance of the exposed soil or sediment provides information about its mineral composition, moisture and organic matter.

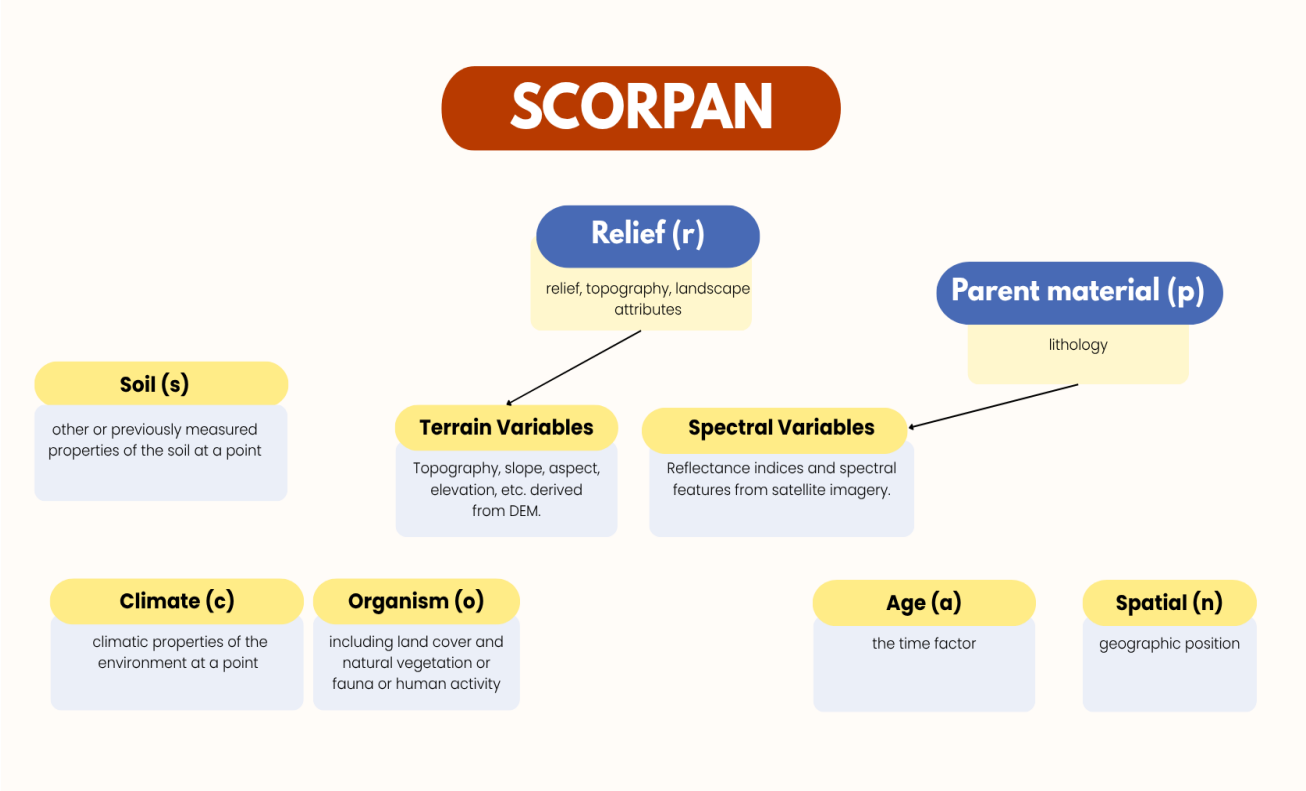


Figure 3.3.1: SCORPAN framework in relation with terrain and spectral variables.
Software used: Canva

3.3.2. Initial predictor pool and multicollinearity screening

The variables described below are not the full original list considered – they were filtered after a deliberate step of reduction and it is more transparent to show that reduction than to present the final variable list as though it had been decided on directly from the outset.

The initial list consisted of:

1. Eleven terrain variables: elevation, slope, aspect, general curvature, profile curvature, terrain ruggedness, the LS Factor, the Topographic Wetness Index (TWI), the Stream Power Index (SPI) and two versions of vertical distance to channel network (one limited to the Po river itself and one including the Po river and four of its tributaries – Tidone, Trebbia, Nure, Arda)
2. Eleven spectral variables: Sentinel-2 bands (B3 – green band, B5 – vegetation red edge 1 band, B6 – vegetation red edge 2 band, B11 – shortwave infrared 1 band and B12 – shortwave infrared 2 band) along with six commonly derived indices: the

Normalized Difference Vegetation Index (NDVI), the Normalized Difference Water Index (NDWI), the Soil-Adjusted Vegetation Index (SAVI), the Bare Soil Index (BSI), a Clay Index and the Ferrous Index.

All the twenty-two variables were analysed in Random Forest model that would risk redundancy, since many terrain derivatives are related to one another based on mathematics and several of the vegetation and soil-brightness indices are known to be strongly correlated with each other and with their constituent raw bands. A Random Forest model is not broken outright by highly correlated predictors, but they can dilute estimates of variable importance across correlated groups and make it harder to interpret which variable is actually the most responsible for a given pattern, which matters for a thesis that leans heavily on interpreting permutation importance and partial dependence results.

To address this, a pairwise correlation matrix was computed across all twenty-two candidate variables and the 'findCorrelation()' function from the 'caret' package (Kuhn, 2008) was implemented to identify variables which exceeded a correlation threshold of 80 ($|r| \geq 0.80$). Using the exact greedy removal method rather than the faster approximate algorithm, this ensures that even the smallest possible set of variables was flagged for removal at each step. Elevation itself was additionally added to the drop list by hand, on the basis that it is a common ancestor variable to nearly every other derivative of terrain in the candidate pool - slope, curvature, TWI, SPI, and both distance-to-channel variables are all computed from the same underlying elevation surface, so raw values of elevation were expected to correlate strongly with several of these regardless of what the automated threshold check happened to detect directly.

Out of the twenty-two original candidates, these ten variables survived the correlation screening:

1. Terrain (six) - slope, aspect, general curvature, profile curvature, the torrents-inclusive vertical distance to channel network, and LS factor.
2. Spectral (four) - B3, B6, B11, and the Ferrous Index

3.3.3. Terrain variables and their relevance to this thesis

The terrain variables used in the final models are discussed in relation to what they measure and why they were expected to help in the identification and classification of D3.1, D4 and D5, drawing on the process descriptions already explained in Section 2.2.2.

Vertical distance to the channel network (VDCN) - including torrents/tributaries

This variable measures how far a given point sits, in terms of elevation, from the nearest mapped watercourse and works as a proxy for exposure to active fluvial incision. This is directly relevant to D5, which is defined particularly as a surface produced by post-tectonic erosional truncation (Cremaschi, 1987) – a closer location to active drainage is mechanically more likely to have experienced this kind of history related to erosion than one sitting well above and away from the channel network. Of the two candidate versions of the variable in the original pool, only the torrents/tributaties-inclusive version survived the screening of correlation.

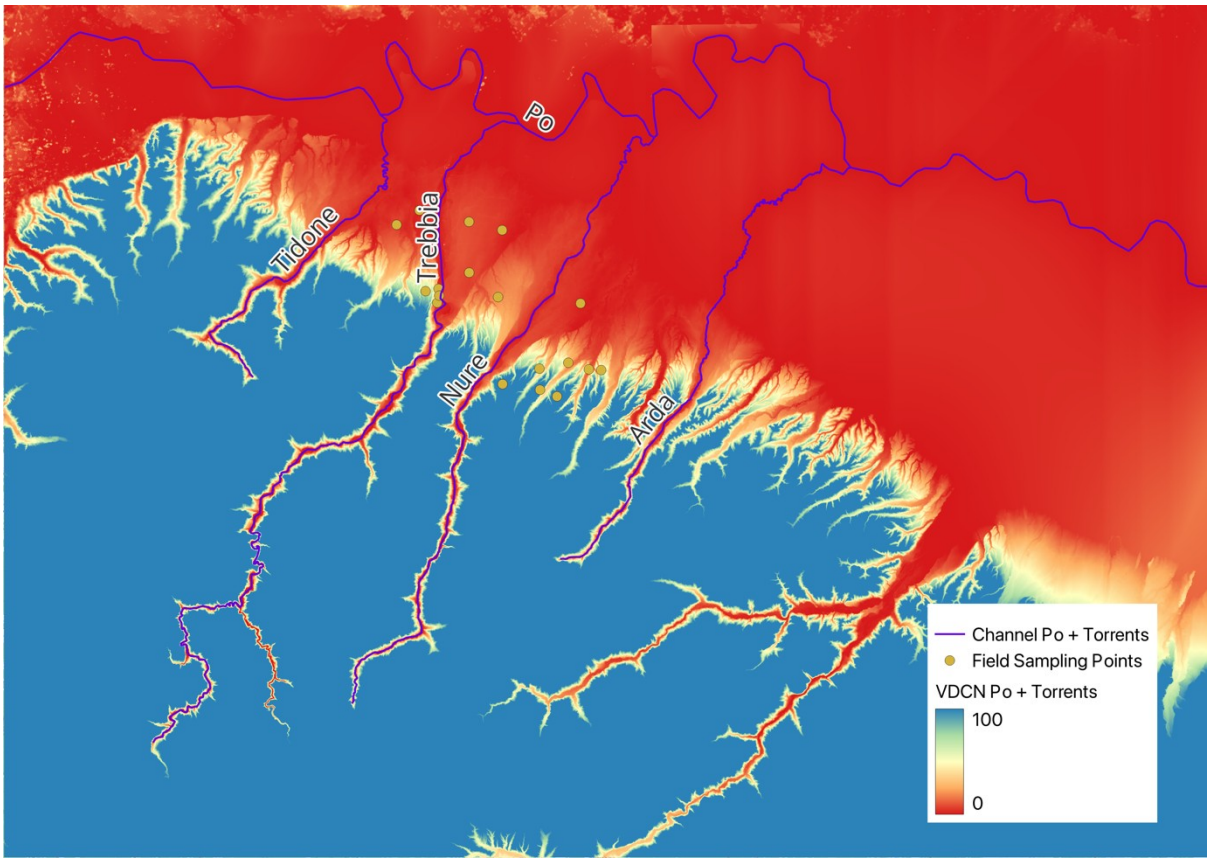


Figure 3.3.3. VDCN Po + torrents draped with channel network Po + torrents

Slope

The steeper the ground, the faster the water sheds, holds less of it in place and is usually more likely to having surface material stripped away rather than preserved. This implies that distinguishing between D5, which is an erosional unit, and D3.1 and D4 makes sense because both consist of material which originated in one place and is then buried under the later loess.

Aspect

This variable measures the slope in terms of the amount of solar radiation received; it has a cascading effect on soil moisture, microclimate and vegetation. It can influence long term weathering rates, and the role of this variable in the analysis is more indirect than that of the other terrain variables. In particular, it is more of a supplementary factor than one of the main reasons why one can distinguish D3.1/D4/D5.

Profile curvature

The profile curvature tells us how the slope changes along the line of steepest descent. Thus, following the path water would take running straight downhill. The flow speeds up and the cell tends toward erosion in places where the surface is convex along that line. In concave places, flow slows down and transported material is most likely to settle (Moore et al., 1991). In this thesis, profile curvature was calculated from the elevation model in SAGA GIS (Conrad et al., 2015). It is meant to separate positions where material is being stripped on the way down - as expected for the erosional surface D5 – from positions where flow loses energy and sediment can collect.

General curvature

This curvature determines how much the surface bends overall, whatever the direction, so it combines the bending down the slope and across it into one value. It shows whether a point sits on a locally covex form such as a ridge or shoulder, or on a concave one such as a hollow or valley floor, but it does not tell in which direction the bending happens (Moore et al., 1991). This makes it different from profile curvature, which only works downhill. General curvature was also calculated in SAGA GIS (Conrad et al., 2015). This curvature is relevant

to D4, the Borzano gravels, which is described by Cremaschi (1987) as braided-river deposits filling valleys cut into the older fluvial formation. Valleys are concave forms, so general curvature gives a direct way of picking up that kind of setting.

LS factor (slope length-steepness)

The LS factor itself was computed using the algorithm developed by Desmet and Govers (1996) for terrains that are topographically complex and is a well-established proxy for cumulative erosion potential along a flow path, which combines slope length and steepness rather than treating slope as a single point measurement (Renard et al., 1987). The LS factor more directly operationalises erosion-process theory than a generic relative-elevation index does – combination of empirical and theoretical grounds when, taken together, made LS factor the more defensible choice for distinguishing an erosional surface (D5) from depositional ones (D3.1, D4).

3.3.4. Spectral variables and their relevance to this thesis

The spectral predictors were drawn from Sentinel-2 Surface Reflectance imagery (Copernicus / S2_SR_HARMONIZED), restricted to locations identified as bare soil.

B3 (Green, ~560 nm)

A band of visible-region, used here mainly as a general indicator of brightness and colour at the surface, since combinations of visible bands are commonly used in geological remote sensing as a broad proxy for iron oxide staining and overall differences in soil colour (Hao et al., 2019).

B6 (Red Edge 2, ~740 nm)

B6 is present in the red-edge portion of the spectrum, which is mainly sensitive to chlorophyll content and vegetation vigour rather than soil mineralogy directly. Its role here is mainly as a secondary check on how genuinely bare a pixel is, since residual vegetation tends to leave a distinct signature in this band even where other masking criteria for bare-soil have been met.

B11 (SWIR 1, ~1610 nm)

B11 sits in the shortwave infrared, a region known and well documented as sensitive to clay minerals, micas and hydroxyl-bearing mineral phases throughout characteristic absorption features (Clark, 1999). This is directly relevant considering the clay-content differences documented across D3.1's B-horizons in Cremaschi (1987) and given that clay content was itself a key differentiator indentified in this thesis's own Malvern texture results.

Ferrous Index (B11 / B8)

This index is derived by dividing the SWIR1 band by the near-infrared band (B8, ~842 nm), which corresponds closely to the classic "ferrous minerals ratio" used in remote sensing of geology since early works which differentiated iron-bearing minerals, later adapted to other sensors with equivalent-range bands (Van der Meer et al., 2014). It is important to be precise about what is actually detected by this index: it is sensitive to ferrous iron, which means iron in its reduced Fe^{2+} state, typically bound in silicate minerals such as pyroxenes and amphiboles is not the same things as the iron oxide minerals identified through Spectral Angle Mapper matching against the USGS Spectral Library discussed elsewhere in this thesis, which are oxidised Fe^{3+} minerals such as goethite. These are different chemistries of iron and any apparent disagreement between findings involving the Ferrous Index and findings involving SAM-matched goethite or hematite mineralogy should be understood as a difference in what is being measured, not a contradiction in the underlying data.

Bare-soil masking rationale

Spectral indices of this kind are only meaningful where they measure exposed soil or sediment directly, which is why Model B's predictor set and training data were restricted to locations with valid, non-vegetated spectral reflectance across all bands simultaneously – the reason Model B's usable point set (n=346) is considerably smaller than Model A's terrain-only point set (n=600).

Sentinel-2 Bands	Central Wavelength (nm)
B1 – Coastal aerosol	443

B2 – Blue	490
B3 – Green	560
B4 – Red	665
B5 – Vegetation Red Edge	705
B6 - Vegetation Red Edge	740
B7 - Vegetation Red Edge	783
B8 - NIR	842
B8A - Vegetation Red Edge	865
B9 – Water vapour	945
B10 – SWIR - Cirrus	1375
B11 – SWIR	1610
B12 – SWIR	2190

Table 3.3.4: Table showing the different bands present in Sentinel-2. Source: Satellite Imaging Corporation

3.3.5. Terrain-only vs. terrain with spectral models: rationale for two models

Two separate RF classifiers were trained rather than one. Model A consist of only the terrain variables described in Section 3.3.3 and is trained on the full filtered training-point set (n = 600), since terrain data is available continuously regardless of vegetation cover or soil exposure. Model B combines the terrain variables with spectral variables as described in Section 3.3.4, restricted to the smaller bare-soil subset of points (n=346).

This design of two models exists to answer a direct empirical question: does adding mineralogical and surface-composition information quantitatively improve the ability of the model to tell D3.1, D4 and D5 apart, over and above terrain shape alone? Structuring the analysis around two parallel models, evaluated under the same spatial scheme of cross-validation, makes it possible to isolate and measure that specific contribution, presented later in the results section.

3.4. Field Data and Laboratory Analyses

3.4.1. Design of field sampling

Field verification of the mapped units required a sampling scheme that could physically test the classes actually present on the ground, rather than assuming the full scheme of six-class documented in Cremaschi (1987) would be equally reachable everywhere within the larger mapped extent. For the primary field study zone, the Piacena area was selected because it is the sector of the broader Cremaschi map where all six loess units under investigation (D2 through D7) occur together within a single field region that is logistically manageable. Working within an area where every target class is physically present in one place, rather than being present across several disconnected sectors of the original map in a scattered way, made it possible to build a coherent, sample set which is comparable across all classes under broadly similar field and access conditions.

Eighteen core samples were collected within this chosen area, structured as three replicate samples for each of the six units (D2, D3.1, D4, D5, D6 and D7). The selection of these eighteen site locations was not chosen randomly in the field; they were instead pre-selected on GIS software ahead of the field campaign, using the digitised extent of each Cremaschi unit within the Piacenza sector as a guide. This step based on pre-selection reflects a fairly standard practice in field-based digital soil mapping campaigns, where locations of candidate samples are identified in advance from existing spatial layers and then physically checked and adjusted on the ground rather than located blind (Brus, 2019). The decision to select three points per class, rather than one, was intended to give atleast a minimal sense of the internal variability that might exist within a single mapped unit, since a unit boundary drawn on a decades-old geological map cannot be assumed to correspond to a texturally or spectrally homogeneous surface at every point within it.

Apart from these eighteen planned points, six additional samples were collected during the same field campaign. These were not pre-decided like the other samples; they were added in response to conditions observed directly in the field, such as an unsually clear or fresh exposed section, a locality that appeared to be present at a boundary between two mapped units, or an outcrop which offers a depth of exposure. It is a recognised practice to incorporate such additional samples with pre-planned design in field-based soil and geomorphological surveys (Brus, 2019). This is because the fixed logistics of a single field season rarely allow every genuine informative location to be identified only from a desk-based plan beforehand (Brus, 2019).

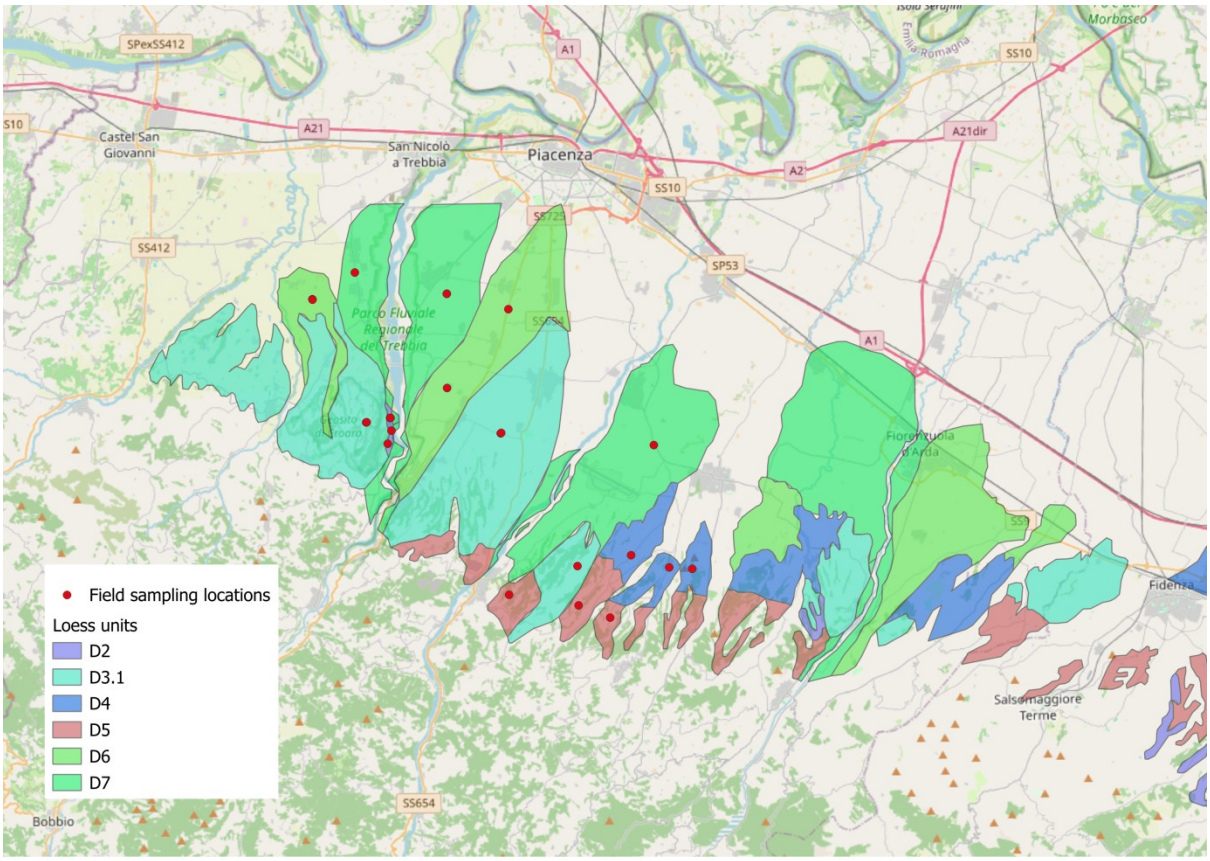


Figure 3.4.1: Field sampling locations within the Piacenza study area, showing planned (n = 18) sample points across the six investigated loess units.

3.4.2. Legacy validation point dataset

Completely separate from the eighteen physically sampled field points, a much larger point-based reference dataset was built to support the training of model and validation across the full spatial extent of the study area in Piacenza. This dataset consists of a total of 1200, which are generated by randomly placing 200 points within each of the six target classes (D2 through D7) by using the tool vector creation inside QGIS, constrained to the digitised polygon boundaries of the corresponding Cremaschi unit. This is a form of stratified random sampling, in which the strata are defined by the mapped geological unit rather than by environmental covariate, which ensures an exact balanced representation of all six classes regardless of how unevenly those units are actually distributed across the study area (Brus, 2019).

After generating the 1200 points and confirming their placement within their intended class polygons, the full terrain and spectral covariate stack described in Section 3 was extracted at each point location. This produced a predictor dataset in tabular form that underlies both Model A and Model B, prior to any of the correlation-based filtering discussed in Section 3.2 or the restriction of bare-soil applied to the spectral variables in Model B specifically. These 1200 points come directly from the pre-existing Cremaschi polygon boundaries as shown in Figure 1.2 (Cremaschi, 1987). The purpose is to give the models a spatially dense and class-balanced sample of the terrain and spectral conditions associated with each mapped unit, with enough information to train and coss-validate a classifier across the full extent of study area.

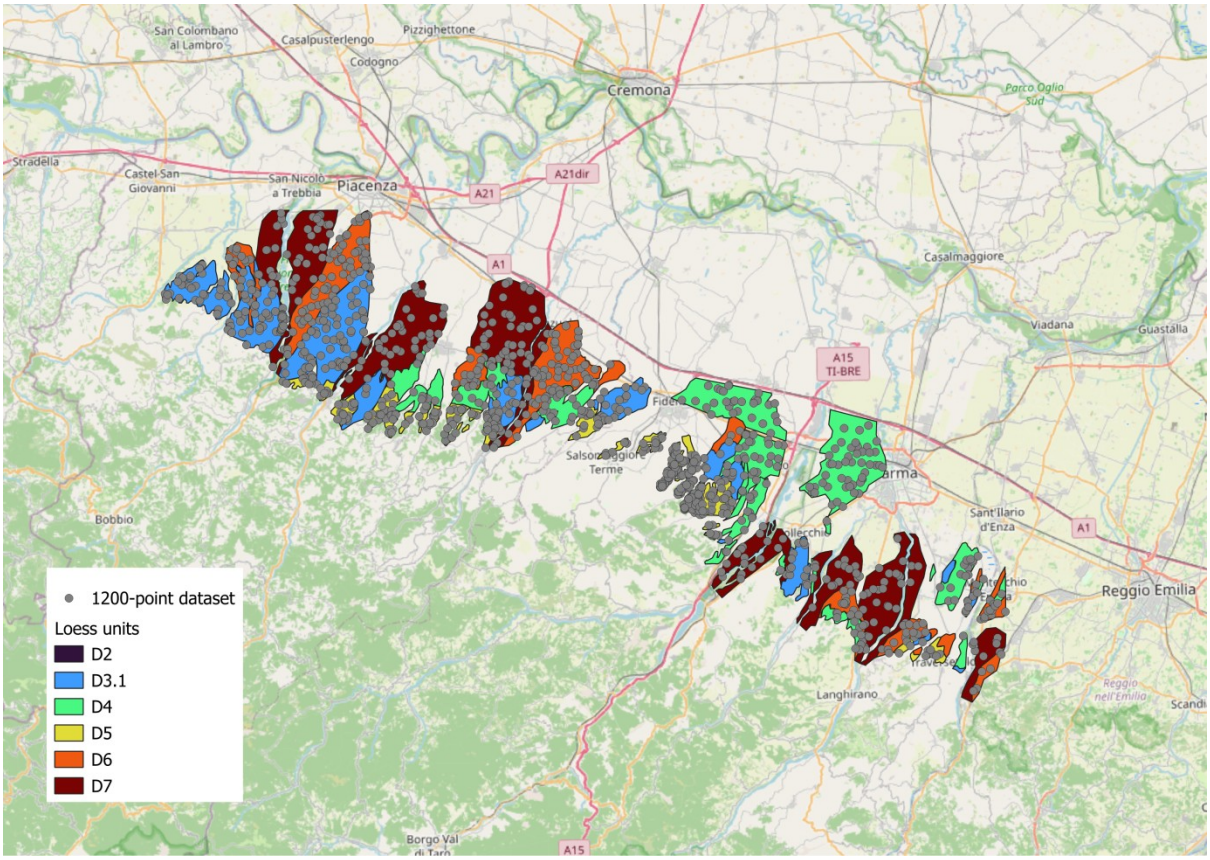


Figure 3.4.2: Spatial distribution of the 1,200-point stratified random reference dataset (200 points per class) across the Piacenza study area.

3.4.3. Spectroradiometer analysis

3.4.3.1. Soil sample preparation and spectral acquisition

Soil samples were prepared and analyzed under controlled laboratory conditions following commonly applied procedures for visible, near-infrared and shortwave-infrared soil

spectroscopy (Stenberg et al., 2010; Ge et al., 2020). To prepare samples for spectral measurements, they were air-dried and subjected to a 2 mm sieve. The sieving removes coarse fragments and plant residues from the samples and helps achieve better homogenization and representative subsamples for analysis. Air-drying and sieving to 2 mm are widely used as standard pretreatment procedures for laboratory Vis–NIR soil spectroscopy (Stenberg et al., 2010; Ge et al., 2020).

Previous studies have also shown that a 2-mm particle size is generally sufficient for soil Vis–NIR measurements, with finer grinding not necessarily providing additional benefits for spectral prediction (Nduwamungu et al., 2009). ASD FieldSpec® 4 Standard-Resolution spectroradiometer was used to acquire the spectral measurements (Analytical Spectral Devices Inc., Boulder, CO, USA), which covers the spectral range 350–2500 nm. The instrument was installed in a fixed laboratory configuration, and the prepared soil samples were positioned directly against the instrument measurement port. This contact configuration minimized variations in measurement geometry and reduced the influence of external illumination, allowing the spectra to be acquired under controlled and reproducible conditions. The use of controlled laboratory conditions is particularly relevant for soil reflectance measurements because moisture, surface structure, roughness, illumination and sensor–sample geometry can substantially influence the measured spectral response (Stenberg et al., 2010; Gholizadeh et al., 2015).

Prior to spectral acquisition, the instrument was calibrated using its white reference standard following the manufacturer's measurement procedure. The white reference was used to characterize the instrument response and establish the reflectance baseline prior to measurement of the soil samples. The calibration was performed under the same measurement configuration used for the soil spectra.

For each soil sample, three independent spectral measurements were acquired at different positions of the prepared sample. Replicate measurements were performed to account for small-scale spatial heterogeneity within the sample and measurement variability. The three spectra were subsequently averaged wavelength by wavelength to obtain a single representative reflectance spectrum for each sample. Replication and averaging of spectral measurements have been used to improve the representativeness and reproducibility of laboratory soil spectroscopy measurements (Barthès et al., 2006; Stenberg et al., 2010).

The spectra produced incorporated all the wavelengths ranging from 350 to 2500 nm in order to understand the overall spectral response of the materials. However, for mineral analysis, the evaluation was limited between the wavelengths of 2000 and 2450 nm as this region encompasses valuable absorption characteristics related to clay minerals, carbonates and other minerals containing hydroxyl groups and water. The VNIR and SWIR ranges of the spectrum are considered to be sensitive to various minerals because it relies on electronic transits and angular vibration processes of molecules (Clark, 1999; Hunt, 1977).

3.4.3.2. Spectral mineralogical assessment

In order to define probable minerals, the obtained spectra of the soil samples were compared with the spectra provided by the USGS spectral library (Version 7) (Kokaly et al., 2017). The USGS Spectral Library contains a huge number of reflectance spectra obtained in laboratory and field conditions. Since the USGS spectra cover the region of wavelengths from 0.35 to 2.5 μm, being compatible with the ones obtained in this research, the possibility of using the library for the purposes of the current research cannot be underestimated (Kokaly et al., 2017).

Before initiating the comparison of the corresponding spectral data, the reference dataset of USGS was modified to include only those mineral phases that have some possibility. The candidate set included illite, muscovite, smectite, montmorillonite, kaolinite, chlorite, calcite, dolomite, gypsum, goethite, hematite, quartz and feldspar. This geological filtering was applied solely to constrain the reference search space and should not be interpreted as evidence for the occurrence of each candidate mineral in the analyzed samples.

The USGS reference spectra were imported from their original ASCII files and restricted to the 2000–2450 nm interval. Because the wavelength sampling of the reference spectra and the FieldSpec measurements may differ, the USGS spectra were linearly interpolated onto the wavelength grid of the measured soil spectra before spectral comparison. No spectral transformation or continuum removal was applied prior to the primary matching analysis, allowing the measured reflectance spectra to be compared directly with the original USGS reference spectra.

Spectral Angle Mapper (SAM) was used to determine the spectral similarity. SAM is a widely established spectral matching approach for hyperspectral and reflectance spectroscopy (Kruse et al., 1993). The measured and reference spectra is represented by SAM as vectors in multidimensional spectral space, calculating the angular distance between them. The SAM angle was calculated as:

$$\text{SAM angle} = \arccos[(x \bullet r) / (||x|| \times ||r||)]$$

Where x represents the measured soil reflectance spectrum and r represents the corresponding USGS reference spectrum. Smaller angular values indicate greater spectral similarity between the target and reference spectra. Because the method is based on the angle between spectral vectors, SAM is relatively insensitive to differences in overall reflectance magnitude and primarily evaluates similarity in spectral shape (Kruse et al., 1993).

For each soil sample, all candidate USGS spectra were ranked according to their SAM angle. The reference spectrum yielding the lowest SAM angle was designated as the first spectral match, whereas the spectrum yielding the second-lowest angle was designated as the second spectral match. The corresponding mineral identity, USGS reference spectrum and SAM angle were retained for each sample. Additionally, the difference between the first- and second-ranked SAM angles was calculated as an auxiliary measure of the distance between the two best spectral matches.

The spectral matches can be understood as indicating the similarity between the investigated samples and reference materials in terms of their spectra, and should not be interpreted as the quantitative assessment of the mineral content in the samples. The differentiation between these two interpretations is important, as soil and loess samples are mineral mixtures and their spectra in fact represent mixed responses of different mineral phases rather than the spectrum of one individual mineral. The USGS Spectral Library itself includes both individual mineral specimens and natural or synthetic mixtures, which reinforces the need to interpret library matching in terms of spectral compatibility rather than direct quantitative mineralogical composition (Kokaly et al., 2017).

Finally, two complementary spectral representations were generated. First, the complete 350–2500 nm reflectance spectra of all samples were plotted to characterize their overall spectral behavior. Second, the 2000–2450 nm SWIR region was plotted together with the original

USGS reference spectra corresponding to the first-ranked spectral matches. This second comparison was used to visually evaluate whether the numerical SAM results were consistent with the overall shape and diagnostic absorption features observed in the measured soil spectra.

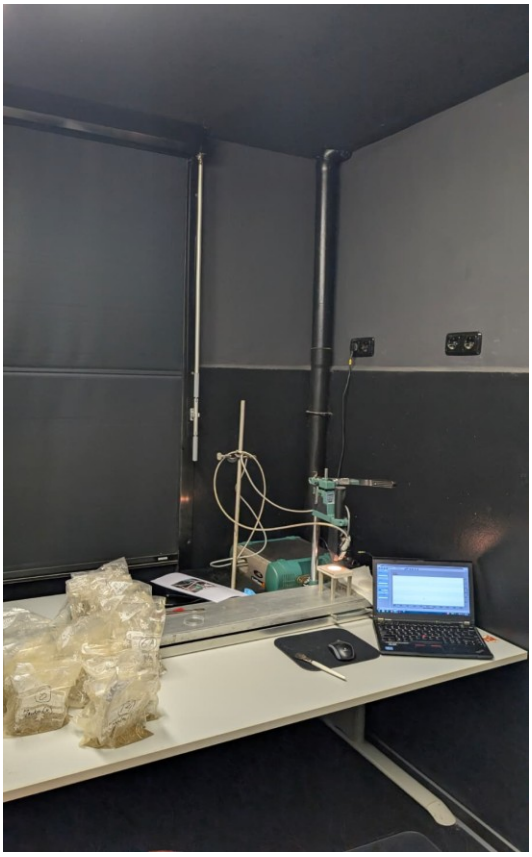


Figure 3.4.3.2: ASD FieldSpec 4 spectroradiometer setup shown during white-reference calibration, with the fiber-optic contact probe positioned over the reference panel inside the light-controlled measurement enclosure, prior to acquisition of the soil sample spectra.

3.4.4. Particle-size (texture) analysis

Malvern Mastersizer 3000 laser diffraction particle size analyser was used for determining the particle-size distribution for the eighteen core samples, following the standard procedure of wet dispersion used for soil and sediment samples of this kind. Laser diffraction works by passing a beam of laser light through a dilute suspension of the sample and measuring the light's angle and intensity scattered by the suspended particles; smaller particles scatter light through wider angles than larger ones and this pattern of scattering is converted into a volumetric particle-size distribution using the theory of Mie scattering, the optical model on which the Mastersizer's calculations are based (Eshel et al., 2004).

General-purpose analysis model was used for analysing each sample, with particles treated as non-spherical for the purposes of the underlying optical model, rather than assuming the idealised spherical particle shape that some laser diffraction defaults use. This choice affects on how the resulting grain-size data should be read, specifically for the clay fraction. Natural soil particles, specifically platy clay minerals, deviate substantially from a spherical shape and laser diffraction instruments infer particle size from the way a particle scatters light, which is itself dependent on shape; the same physical particle can therefore return a different apparent size under a spherical assumption than under a non-spherical one. Even with the non-spherical setting applied, laser diffraction has been known to show in the literature to underestimate the clay-sized fraction relative to classical sedimentation-based methods such as the pipette method, an effect attributed specifically to the platy, non-equant shape of clay particles, which causes them to be registered as coarser than their true size (Konert & Vandenberghe, 1997). This caveat is necessary for this thesis specifically, since the resulting texture classifications are compared later against figures of clay-content reported in Cremaschi (1987), which were obtained using classical sedimentation-based grain-size methods rather than laser diffraction; any such comparison should account for this known systematic offset between the two techniques rather than treating the clay percentages from both sources as directly equivalent (Konert et al., 2004).

SiO2 (quartz) was used for configuring the optical model itself as the reference material, with a refractive index of 1.457, an absorption index of 0.01 and a density of 1 g/cm³ entered for the particle properties, while the dispersant was set to water, with a refractive index of 1.33. These optical parameters, specifically the assumed refractive and absorption indices of the particulate material, directly affect the diffraction pattern the software expects to see from a particle of a given size and inappropriate values for these parameters are a known source of discrepancy between laser diffraction results and other particle-size methods (Eshel et al., 2004). Considering that quartz is typically the dominant mineral phase by volume in the sand and silt fractions of such material, thereby a quartz-based optical model is a common and reasonable default for terrestrial soil and sediment samples, even though the true optical properties of a natural, mineralogically mixed sample will envitably differ somewhat from those of pure quartz.

Each cycle of sample measurement consisted of a 50-second background measurement followed by a 30-second sample measurement, for both the red and blue light sources used by the instrument; the Mastersizer 3000 uses two laser wavelengths, which gathers scattering data across a wider range of angles than a single-wavelength system and thereby improves sizing accuracy across a broader range of particle-size, particularly for the finer end of the distribution (Callesen et al., 2023). Each sample was run through five repeat measurements, with a delay of 5-second between each and no additional pre-measurement or pre-alignment delay, and the sample was continuously agitated at a stirrer speed of 3,500 RPM throughout, in order to keep particles in suspension and prevent settling or reflocculation during measurement. An obscuration range between 5 percent to 30 percent was accepted for measurements, which is a standard quality-control window ensuring that the sample concentration in the measurement cell was neither too dilute, which would produce a weak and noisy scattering signal, nor too concentrated, which would introduce effects of multiple-scattering that distort the resulting size distribution (Callesen et al., 2023).

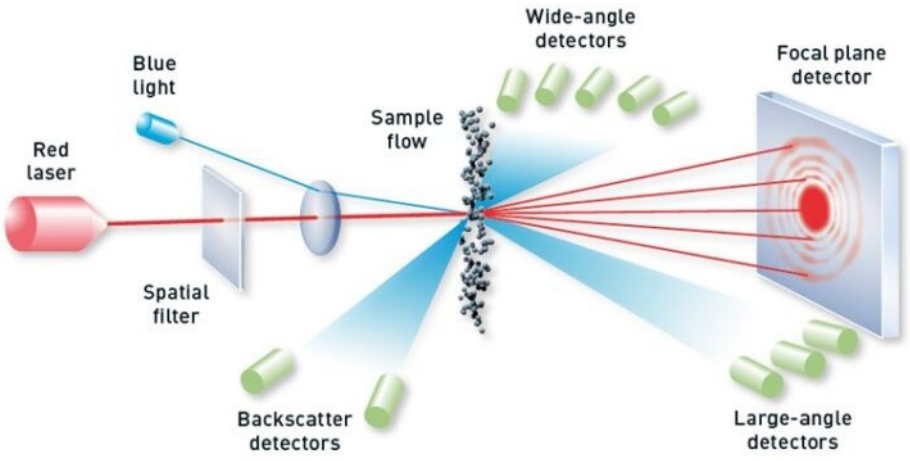


Figure 3.4.4: Illustration of a laser diffraction measurement using the Mastersizer 3000, Source: Reproduced from Malvern Panalytical (n.d.).

From the results of volumetric particle-size distribution, standard descriptive statistics were derived for each sample, which includes the modal particle diameter, the Dv10, Dv50 (median) and Dv90 percentile diameters, the percentage volume falling within the clay, silt and sand size fractions as defined by the particle-size classification scheme of USDA and derived shape statistics for the distribution itself, namely skewness, kurtosis and sorting. These percentage fractions were subsequently used to categorise each samples a USDA soil

texture class, which follows the standard USDA texture triangle classification based on the relative proportions of clay, silt and sand.

3.5. Data Preprocessing and Alignment

3.5.1. Derivation of Bare-soil point

Since the spectral predictors used in Model B are only physically meaningful over exposed soil, a binary bare-soil mask was created to identify which pixel and by extension which reference points, fall within the inclusion for the spectral analysis at all. This mask was built by combining three spectral indices, each targeting a different possible source of contamination in the signal of bare-soil: vegetation and open water.

The first two indices jointly form what can be thought of as a detection gate of bare-soil. The Normalised Difference Vegetation Index (NDVI), derived from the near-infrared and red bands, is one of the most commonly used and long-established indicators of live vegetation cover, with higher values denoting denser, healthier chlorophyll-bearing vegetation and values near zero or below typically signifying bare or sparsely vegetated ground (Tucker, 1979). A pixel was passed for Model B as a candidate only if its NDVI value fell below a threshold of 0.30, a cutoff broadly consistent with published ranges distinguishing bare soil from vegetated surfaces (Tucker, 1979). Alongside this, the Bare Soil Index (BSI), which combines the shortwave-infrared, red, near-infrared and blue bands into a single index designed specifically to improve the spectral contrast between exposed soil and other land cover types, was required to exceed a threshold of -0.10 (Mzid et al., 2021). Implementation of both indices together, rather than relying on NDVI alone, reduces the chance of misclassifying surfaces that happen to have low vegetation greenness but are not actually exposed soil, such as certain non-vegetated but non-soil land covers, since BSI particularly targets the reflectance signature of soil rather than simple the absence of chlorophyll.

The Modified Normalised Difference Water Index (MNDWI), calculated from the green and shortwave-infrared bands, was used as a third component to exclude any residual open-water pixels from the mask, which applies the standard threshold of zero, above which a pixel is conventionally classified as water (Xu, 2006). This water check was applied as a second,

independent safeguard, since cloud and water pixels had already been excluded upstream during the initial Sentinel-2 cloud-masking step; which includes this additional MNDWI-based filter reduces the risk that a small number of water pixels slipping through the initial cloud mask would be misread as valid signals of bare-soil and bare-earth.

A pixel was included in the final binary bare-soil mask only if it fulfilled the three conditions: NDVI below 0.30, BSI above -0.10 and MNDWI below zero. This layered and multi-index approach reflects a broader and well-recognised limitation of bare-soil detection in remote sensing, namely that no single spectral index alone can reliably distinguish bare soil from every other possible land-cover confounder on its own, since vegetation indices alone can be fooled by dry or senescent non-soil surfaces and soil indices alone can be fooled by certain built or rocky surfaces, which makes combined, multi-condition masking a more defensible strategy than any single threshold in isolation (Demattê et al., 2018). It is this bare-soil mask, applied at the pixel level, that finally decides which of the reference points were eligible for inclusion in Model B's training and validation set, which explains the reduction from the full sample size of 600 points used in Model A down to the sample size of 346 points usuable in Model B.

3.5.2. Value-range masking

The final step of preprocessing addressed a specific risk in applying a trained RF model back onto the full raster extent of the study area: a model can only be expected to make predictions reliably within the range of predictor values it was actually trained on, and applying it to raster cells who covariate fall far outside that range of training amounts to extrapolation rather than genuine prediction (Meyer & Pebesma, 2021). To overcome this, the minimum and maximum value of every retained predictor, as observed specifically at the training points, was calculated separately for Model A and Model B, and the corresponding prediction rasters were subsequently clipped to these observed ranges before generating the final classified surfaces.

This masking based on range was computed independently for each model rather than using a single shared range across both, because the two models are trained on point sets that are genuinely different – Model A on the full n = 600 point dataset and Model B on the smaller n = 346 bare-soil-limited subset – and the ranges of the observed covariate differ measurably

between them as a direct consequence. This difference is visible clearly in the training data itself: the LS factor, for instance, ranges from approximately 0.031 to 5,218.9 across the training data of Model A, but only from approximately 0.097 to 4,313.5 across Model B's smaller, bare-soil-limited training set. Applying a single shared range across both models would therefore either incorrectly restrict Model A's prediction surface to the narrower range actually observed in Model B's point or conversely allow Model B to be applied to combinations of terrain conditions it never actually encountered during training, which undermines the very purpose of this masking step.

3.6. Model Training

3.6.1. Algorithm specification

Random Forest algorithm was used to build both classifiers, implemented in R through the 'randomForest' package and trained via the 'caret' package's unified 'train()' interface (Kuhn, 2008). RF operates by growing a large ensemble of individual decision trees, each fitted on a bootstrap-resampled subset of the training data and each considering only a randomly restricted subset of the available predictors at every internal split, before combining the predictions of every tree through majority voting for classification (Breiman, 2001). This integration of bootstrap aggregation and random predictor restriction is what gives the algorithm its resistance to overfitting relative to a single decision tree, since the prediction errors of many weakly correlated trees tend to cancel out once averaged across the full ensemble (Breiman, 2001). A fixed random seed (123) was set before training the model, which ensures that the bootstrap resampling inside the forest, along with the spatial fold construction described in Section 3.6.2, is exactly reproducible if the same script is re-run.

We used a fixed 500 trees (ntree = 500) as the forest size for both models. This is a widely implemented default in RF applications, which reflects the observation that out-of-bag error of a forest typically stabilises well before 500 trees have been grown, so that adding further trees beyond this point will result in little additional gain in predictive performance while increasing computational load (Breiman, 2001). The amount of predictors considered at each split (mtry) was left to 'caret' 's own internal tuning procedure rather than being fixed manually or searched across a custom grid; since no 'tuneGrid' or 'tuneLength' argument was

explicitly supplied to ‘train()’, ‘caret’ defaulted to its standard tuning behaviour, which automatically tests a small default set of candidate mtry values around the conventional square-root-predictors heuristic used for classification random forests and selecting whichever values performed best under cross-validation (Kuhn, 2008).

The selection of model was based on the Area Under the Curve (AUC), specified directly as the target metric passed to ‘train()’, rather than Accuracy or Kappa. In order to make this possible, ‘trainControl’ was configured with ‘classProbs = TRUE’, so that probabilities of class rather than only hard class labels were retained at each fold of cross-validation and with **‘caret::multiClassSummary’** set as the summary fuction, computing AUC and other performance statistics appropriately extended to the three-class classification problem addressed here (Kuhn, 2008). Using AUC as the tuning criterion, rather than raw classification accuracy, reflects an intentional choice to select the mtry value that produces the best probabilistic class separation across all three classes jointly, rather than the value that just maximises the proportion of correctly labelled points, which can be a less informative criterion when a model’s predicted class probabilities are themselves later used for downstream analyses such as partial dependence plots.

3.6.2. Construction of spatial cross-validation fold

Spatially structured cross-validation folds were used to evaluate both models rather than conventional random k-fold cross-validation, to avoid the well-documented problem of spatial autocorrelation inflating cross-validated accuracy estimates. A model can effectively exploit spatially autocorrelated similarity between a training point and a nearby test point when nearby points are randomly split across training and testing folds because neighbouring locations tend to share highly similar terrain and spectral conditions simply due to proximity; this produces accuracy estimates that overstate a model’s true ability to generalise to genuinely new, spatially distant locations (Roberts et al., 2017).

The procedure of specific fold-construction used here goes a step further than a single, direct k-means clustering step in five groups. For each of the three target classes separately, k-means clustering was first applied to that class’s point coordinates using a comparatively large number of clusters than the final number of folds, specifically five times the fold count (twenty-five clusters per class, or fewer if a class had fewer available points than this). This

led to many small, spatially compact micro-clusters within each class, rather than five large, coarse regions. All of the resulting micro-clusters, pooled together across all three classes, were then sorted by size from largest to smallest, and assigned one at a time whichever of the five folds currently held the smallest running total of points. This greedy, size-ordered assignment strategy is a direct application of the longest-processing time (LPT) approach to multiway number partitioning , a classic result in combinatorial scheduling theory which shows that assigning the largest remaining item to the currently least-loaded group, in descending size order, produces a reliably well-balanced partition even though it does not guarantee the mathematically optimal one (Graham, 1969).

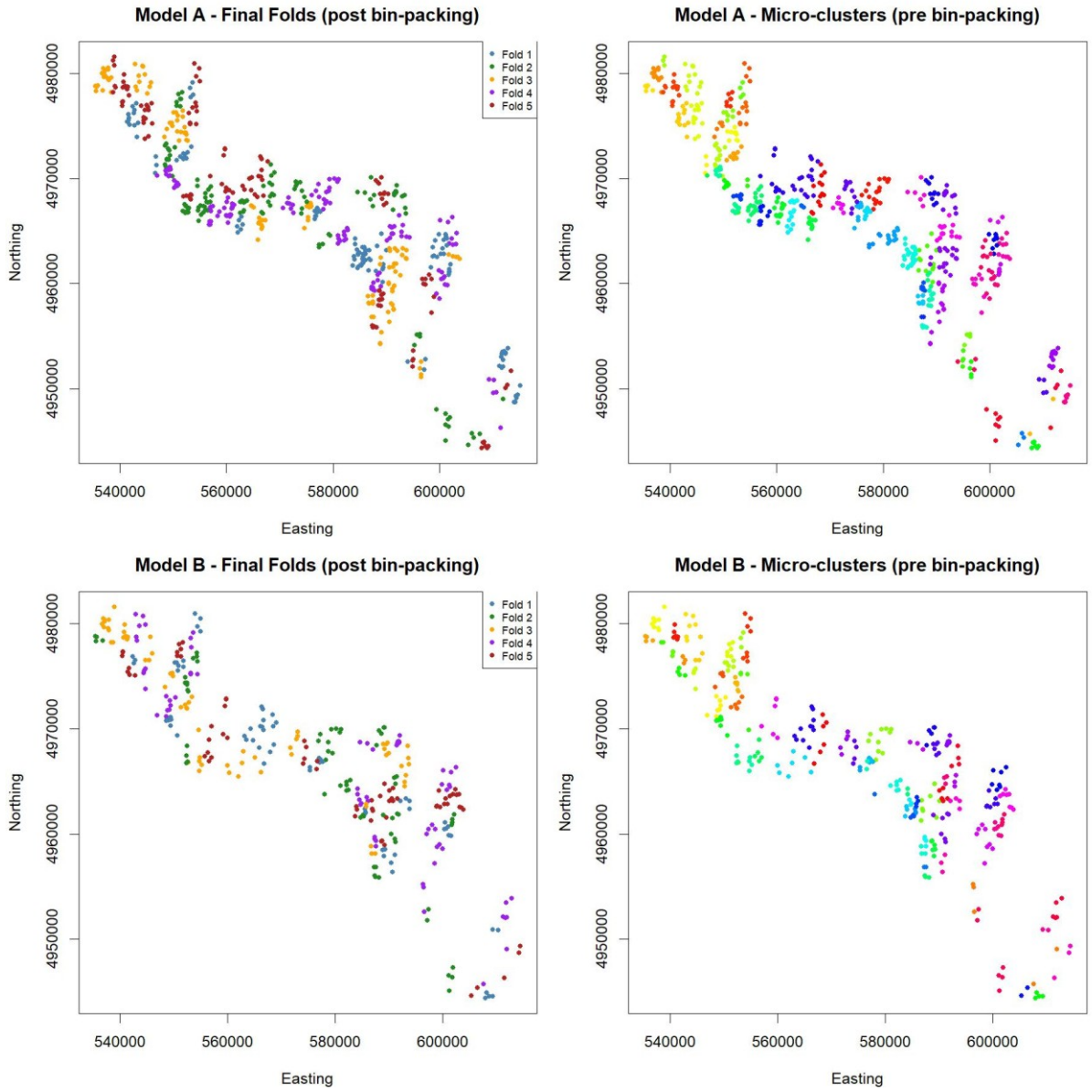


Figure 3.6.2: Spatial distribution of the five bin-packed cross-validation folds derived from fine-grained, class-stratified k-means clustering, shown separately for Model A and Model B.

The combination of these two steps addresses a specific difficulty in constructing folds for problems of spatial classification: fine-grained spatial clustering on its own keeps individual micro-clusters geographically compact, but does not guarantee that the five final folds end up similar in size or composition of class, while a simple balancing step applied to individual points, without first respecting spatial grouping, would undo the spatial separation the whole exercise is meant to achieve. Carrying out the clustering step separately within each step before pooling and bin-packing the resulting clusters ensures that greedy balancing step distributes spatial units, not raw points, while still maintaining the proportion of class across folds close to the same balanced ratio present in the underlying training dataset. This entire procedure of fold-construction was conducted independently for Model A's training data (n=600) and Model B's training data (n=346), as different point sets are used for training the two models, which produces two separate sets of fold assignments used respectively in each model's 'trainControl' configuration via a custom 'index' argument, rather than relying on 'caret' 's own routine of automatic fold-generation.

3.6.3. Final specification of Model A and Model B

Following the multicollinearity screening described in Section 3.3.2, the final set of predictors used to train each model was as follows.

Model A, the terrain-only classifier, was trained on six predictors of terrain: vertical distance to channel network (including torrents), slope, aspect, profile curvature, general curvature and the LS factor. This model used the full n = 600 points training dataset, since the terrain covariates are available continuously across the study area regardless of vegetation cover.

Model B, the terrain with spectral classifier, was trained using the same six predictors as Model A, together with four spectral predictors derived from Sentinel-2 imagery: B3, B6, B11 and the Ferrous Index. Since these spectral predictors are only physically meaningful over exposed, non-vegetated ground, Model B was trained on the smaller n=346 point subset that passed the bare-soil masking criteria described in Section 3.5.3.

The formula interface in 'caret::train()' was used for fitting of both models, which predicts the reference class ('ref_class', restricted to the three focal classes D3.1, D4 and D5) from their respective predictor sets, which uses the "rf" method, the model-specific spatial cross-validation control object described in Section 3.6.2, AUC as the tuning metric and 500 trees. Structuring both models with a same six-variable terrain baseline, differing only in the addition of the four-variable spectral block in Model B, was an intentional design choice; it ensures that any difference in performance of classification reported later in the results can be attributed specifically to the addition of spectral information, rather than to some incidental difference in the terrain covariates each model happened to use.

3.7. Evaluation of Model

3.7.1. Evaluation metrics

For each model, four complementary metrics were computed and all of them were derived exclusively from out-of-fold predictions generated during the spatial cross-validation procedure described in Section 3.6.2, rather than from predictions the models are already familiar with during training. Restricting every reported metric to out-of-fold predictions matters because performance of a model on the same data it was fitted to is a poor proxy for how it will behave on genuinely new locations and reporting only out-of-fold results keeps the evaluation consistent with the spatially honest cross-validation design established earlier in this thesis.

The confusion matrix built from the pooled out-of-fold class predictions across all five spatial folds was used to compute the overall Accuracy and Cohen's Kappa. Kappa is reported along with raw Accuracy because Accuracy alone can be misleadingly high on dataset with unequal class representation, whereas Kappa adjusts for the level of agreement expected by chance alone, which gives a more conservative and arguably more honest picture of how much the performance of a classifier actually reflects genuine class-separating skill (Cohen, 1960).

Multiclass Area Under the Curve (AUC) was computed using the generalisation of the standard two-class AUC statistic proposed by Hand and Till (2021), extending the Receiver Operating Characteristic framework to problems with more than two classes by averaging

pairwise class comparisons across all class pairs, rather than requiring an arbitrary reduction of the three-class problem down to a series of a one-versus-rest binary comparisons. This multiclass AUC was calculated directly from the probabilities of predicted class retained at each out-of-fold prediction, which uses the same probability outputs that were also used to tune the mtry hyperparameter described in Section 3.6.1, so that the criteria of model selection and the final reported performance metric are drawn from a consistent probabilistic basis throughout.

An ordinal Root Mean Squared Error (RMSE) was included as the fourth metric specifically because the three focal classes in this thesis are not simply unordered categories but instead form a sequence that is genetically meaningful tied to relative landscape age and process, as established in Section 2. Treating a genuine ordinal classification problem as though it were a purely nominal one discard information about how far off a wrong prediction actually is; a model that mistakes D3.1 for D5 is making a more serious error, in process terms, than one that mistakes D3.1 for D4 because D3.1 and D4 sit closer together in the depositional-erosional sequence than D3.1 and D5 do. To understand this, each class was assigned a numeric rank (D3.1 = 1, D4 = 2 and D5 = 3) and the ordinal RMSE was calculated as the root mean squared distance between each point's expected rank, computed as the probability weighted average of the ranks of the three class using the model's own predicted class probabilities and its true observed rank. Using RMSE for ordinal classification problems of this kind is a documented and empirically supported choice in the evaluation literature of machine-learning, which has shown that metrics based on RMSE correlate more closely with genuine ordinal predictive skill than simpler agreement-based statistics do, particularly because RMSE penalises predictions that are further from the true class more heavily than predictions that are only one rank removed (Gaudette & Japkowicz, 2009).

3.7.2. Permutation importance procedure

To evaluate the dependency of each model on individual predictors, permutation importance was computed for every terrain and spectral variable in both Model A and Model B. The underlying logic of this method is model-agnostic: rather than relying on any internal splitting statistic specific to Random Forest, a variable's importance is determined directly by measuring how much the predictive accuracy of a model deteriorates once that variable's values are randomly shuffled across the dataset, thereby destroying whatever real relationship

that variable originally had with the outcome while leaving every other variable and the overall structure of the data, untouched (Fisher et al., 2019). A variable on which the model depends heavily will produce a substantial drop in accuracy once permuted, since the model is still being fed with what it treats as a meaningful predictor, only now with the wrong values attached to each point, whereas a variable the model barely uses will show little or no accuracy change when permuted, since the model was not relying on it in the first place.

In this thesis, this permutation-and-measure cycle was repeated ten times independently for every variable, rather than performed only once and the value of importance reported for each variable is the drop in mean accuracy across these ten repeats, alongside the standard deviation of that drop. Repeating the permutation multiple times per variable, rather than relying on a random shuffle one time, accounts for the fact that any one particular random permutation is itself a somewhat arbitrary reordering of the data and a single unlucky or lucky shuffle could over or understate the true importance of a variable; whose averages across repeats could produce a more stable and statistically defensible importance estimate, along with a variability measure that shows how consistent that importance actually is across different random reordering (Fisher et al., 2019). This approach based on general resampling to variable importance traces back to the original literature on Random Forest, in which permutation importance was first proposed as a way to interpret which predictors a fitted forest depends on, independent of the specific criteria of tree-splitting used internally (Breiman, 2001).

It is important to describe how this thesis interprets permutation importance results, since it is easy to over-read them. A high permutation importance value shows that a model found a variable statistically useful for producing predictions that are accurate across the specific spatial cross-validation folds used here; it does not, on its own, prove that the variable is casually responsible for the outcome, nor does a low importance value necessarily has to mean that a variable is geologically irrelevant, since correlated predictors can sometimes mask one another’s individual importance within a RF.

3.7.3. Partial dependence plot procedure

For every predictor in both models, the partial dependence plots (PDPs) were computed to visualise the direction and shape of each variable’s relationship with the predicted

probabilities of class, which holds the influence of all other variables constant in aggregate. The method follows the approach originally proposed by Friedman (2001): for a given variable, a fine grid of values which spans that variable's observed range in the training data is constructed, and for each value on this grid, every observation in the training dataset has that one variable's value temporarily replaced with the current value of the grid, while every other variable in each observation is left at its own original, observed value. The model then generates a probability of predicted class for every observation under this temporary substitution, and these predictions are averaged across all observations to produce a single average predicted probability for that grid value. Repeating this process across the full grid produces a curve showing how the average of the model predicted probability for a given class changes as the variable of interest moves across its observed range, effectively marginalising out the influence of every other predictor by averaging over their naturally occurring joint distribution in the data, rather than fixing them at some artificial reference value such as their mean (Friedman, 2001).

In this thesis, each variable's grid was constructed using fifty evenly spaced points which spans the minimum to maximum value observed for that variable within the relevant model's own training data, which means Model A's PDPs are built from the terrain-only dataset and Model B's PDPs are built from its own terrain-plus-spectral, bare-soil-limited dataset. Since both models consist of three target classes rather than two, a full PDP curve was generated for each class separately at every grid point, so that the PDP output of a single variable shows three simultaneous probability curves, one per class, which allows a direct visual comparison of how a given terrain or spectral variable pushes the model's predicted probability toward one class and away from the others as the value of that variable changes.

It is important to point out one general limitation of the partial dependence approach: since PDPs average over the observed joint distribution of the remaining variables rather than genuinely holding them fixed, the resulting curve can be somewhat misleading if the variable being plotted is strongly correlated with one or more of the variables being averaged over, since some of the combinations generated during this step of averaging may not correspond to realistic or physically plausible combinations of terrain or spectral conditions actually found in the landscape (Friedman, 2001). This is a standard caveat attached to PDP interpretation generally and while the screening based on correlation described in Section 3.3.2 reduces the most extreme cases of this problem by eliminating highly intercorrelated

predictors beforehand, it does not eliminate more moderate correlations between the retained variables, so PDP curves in the following results chapter should be read as showing an averaged tendency rather than a guaranteed, universally applicable relationship.

3.8. Integration with Independent Geological Evidence

3.8.1. Analytical strategy statement

Everything mention in Section 3.7 – rankings of permutation importance, partial dependence curves, cross-validated accuracy – describes how well the two RF models fit the data they were given and which variables they lean on to do so. None of that, taken alone, actually tells us whether the patterns the models found correspond to anything real about how these landscape units actually come to exist. A strong result can be achieved by a model statistically for reasons that have nothing to do with genuine process, simply by exploiting whatever incidental correlations happen to exist in a particular training sample and a purely statistics-first reading of the results risks mistaking a convenient numerical pattern for geological insight. This is a known limitation of applying machine learning in digital soil mapping specifically: field reviews have pointed out that the great majority of published studies stop at reporting accuracy of prediction, without going further step of checking whether the internal behavior of a model is actually plausible in light of independently established soil-forming processes and have argued that doing so is what separates a merely accurate map from that also deepens scientific understanding of the landscape it is describing (Wadoux et al., 2020).

This thesis undertakes that second, more demanding standard as its explicit analytical strategy for the discussion chapter that follows. Rather than treating the PDP and permutation importance results from Section 3.7 as a self-contained conclusion, this thesis cross-checks every notable statistical pattern derived from those tools against three independent, non-statistical lines of geological evidence collected earlier in this research: the spectral mineralogy derived by Spectral Angle Mapper matching against the USGS Spectral Library (Section 3.4.3), the particle-size and textural data obtained from the Malvern Mastersizer analysis (Section 3.4.4) and the documented process-level descriptions of the D3.1, D4 and D5 units given in Cremaschi's (1987) original stratigraphic study of the central Po Plain. None of these three lines of evidence were used anywhere in building, training or tuning

either RF model; they exist entirely outside the statistical modeling pipeline, which have been collected and interpreted through separate laboratories and methods based on literature. This independence is exactly what makes them useful as a check rather than a restatement of the same information the models were already trained on.

There are two directions in which the logic behind this cross-checking exercise works rather than one. First, where a PDP shows the probability of a class prediction rising sharply with, e.g., concave curvature or proximity to the drainage network, this thesis asks whether that statistical tendency has a physically sensible explanation in Cremaschi's documented work of how that specific unit actually formed, rather than accepting the pattern at face value simply because the model found it. The response of a terrain that lines up with an independently documented depositional or erosional process, such as an erosional unit showing higher predicted probability on steeper ground, is treated as a pattern with legitimate grounding of geology, whereas a strong statistical response with no plausible process-based explanation is flagged as a result which requires caution rather than confident interpretation. Second, and in the opposite direction, the evidence from textural and spectral is used to test whether the assumptions on mineralogy and grain-size implicit in importance of a spectral predictor actually hold up once checked against direct laboratory measurement; as already anticipated in Section 3.3.4, is the distinction between the specific sensitivity of Ferrous Index to reduced, ferrous iron minerals and the Spectral Angle Mapper's identification of oxidized iron minerals such as goethite, since these represent iron chemistries that are genuinely different and should not be assumed to corroborate one another on its own just because both happen to involve iron.

The role of discussion chapter is not to just narrate the statistical results a second time, but to explicitly rest each notable finding from Section 3.7 against these three independent evidence streams and report, case by case, whether the statistical and geological pictures converge or diverge in an informative way that revises the working interpretation of a unit, as happened with the relative-age reassessment of D3.1 discussed elsewhere in this thesis or whether a genuine, unresolved discrepancy remains that should be mentioned plainly rather than explained away. In this approach, convergence across independent evidence types is treated in a stronger form of support than any single line of evidence could provide on its own, as terrain statistics, mineralogy, texture and documented field stratigraphy are each sensitive to different kinds of error and bias and a pattern that shows up consistently across genuinely

independent measurement types is considered more likely to not be a coincidental artifact of any one method alone.

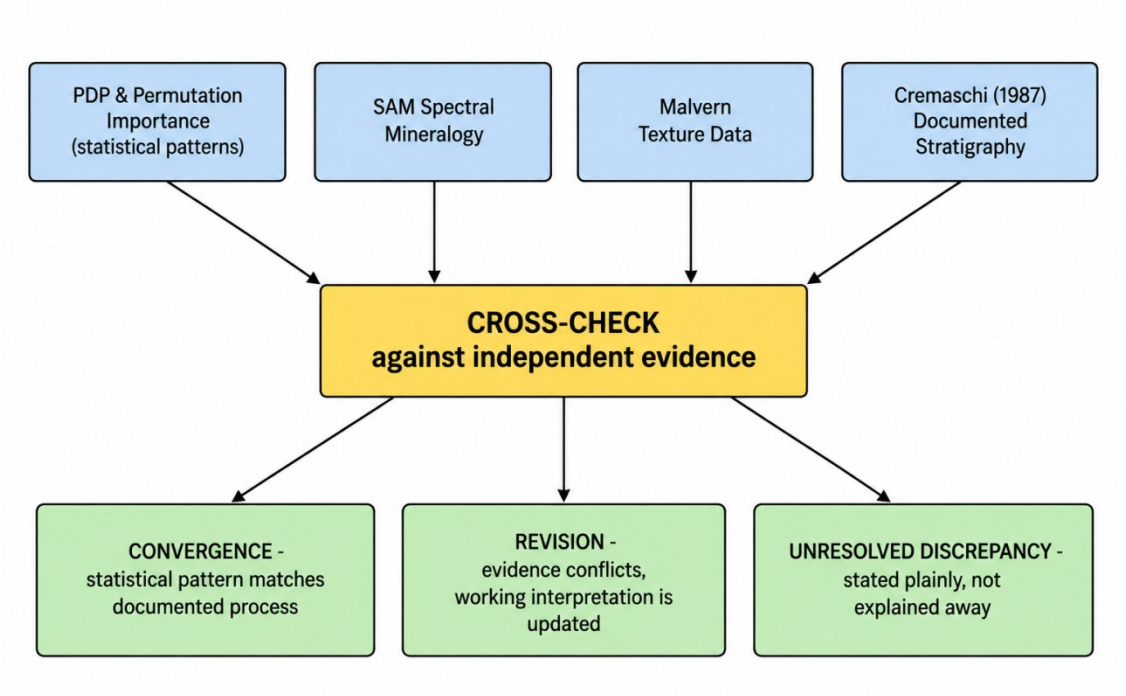


Figure 3.8.1: Analytical framework for cross-checking statistical model patterns against independent geological, mineralogical and textural evidence. Software used: Canva

4. RESULTS

4.1. Overview of Reporting Approach

In order to give Model A and Model B a complete, self-contained account of how they performed before any direct comparison between the model is drawn, the findings in this chapter are arranged model by model rather than metric by metric. Within the evaluation of each model, results are presented in the same order the evaluation itself was carried out; first the results of spatial cross-validation computed from within the Piacenza training area, so that the reader encounters the more statistically robust result. Once the predictive performance of both models has been laid out this way, the chapter turns to the spectral mineralogy, particle-size texture and results of spatial mapping, which stand somewhat apart from the classification metric themselves but provide an evidentiary basis the discussion chapter will later draw on when checking whether these statistical patterns hold up against independent geological reasoning.

4.2. Spatial Cross-Validation Performance

4.2.1. Comparison of overall performance

Table 4.2.1 below summarises the four metrics of out-of-fold evaluation defined in Section 3.7.1 computed separately for Model A and Model B under the scheme of spatial cross-validation in Section 3.6.2. Model B, which adds the four spectral predictors to the same baseline of terrain predictors in Model A, outperforms Model A on every single metric: Accuracy rises from 56.7% to 63.0%, a gain of 6.3 percentage points; Kappa rises from 0.350 to 0.436, a gain of roughly 0.086; multiclass AUC increases from 0.774 to 0.816; and ordinal RMSE drops from 0.786 to 0.743, which means Model B's misclassifications are, on average, both less frequent and closer to the correct class rank than Model A's.

Model	Accuracy	Kappa	Multiclass AUC	Ordinal RMSE
Model A (Terrain-only)	56.7%	0.350	0.774	0.786
Model B (Terrain + Spectral)	63.0%	0.436	0.816	0.743

Table 4.2.1: Out-of-fold spatial cross-validation performance, Model A versus Model B.

When compared against standard qualitative benchmarks for Kappa, Model A's (value of 0.350 falls in the range that is conventionally described as fair agreement, while the value of Model B is placed at the boundary between fair and moderate agreement (Landis & Koch, 1977). Neither model reaches a level that would be considered a strong agreement on its own and this should be stated plainly rather than downplayed: even the better performing Model B is still misclassifying more than a third of held-out points. What is mainly observed in the comparison is that adding the spectral predictor block produces a real, non-trivial improvement in both raw agreement and in how far off the remaining errors tend to be and it does so despite of Model B being trained on only 346 points against Model A's 600, a smaller training sample that would normally be expected to hurt performance rather than help it (Congalton, 1991). However, the smaller spectrally enriched dataset still outperforms the large, terrain-only one is itself a notable result and should be stated as such.

McNemar's test of Model A returned a statistically significant result ($p = 0.0059$), indicating that the pattern of errors is not symmetric across the three classes – the model is systematically biased toward directions of certain misclassifications rather than making random mistakes uniformly across all class pairs. McNemar's test of Model B, by contrast, was not statistically significant ($p = 0.224$), which suggests a more even error distribution across classes once the spectral predictors are included, consistent with the improvement in Kappa reported above (Landis & Koch, 1977).

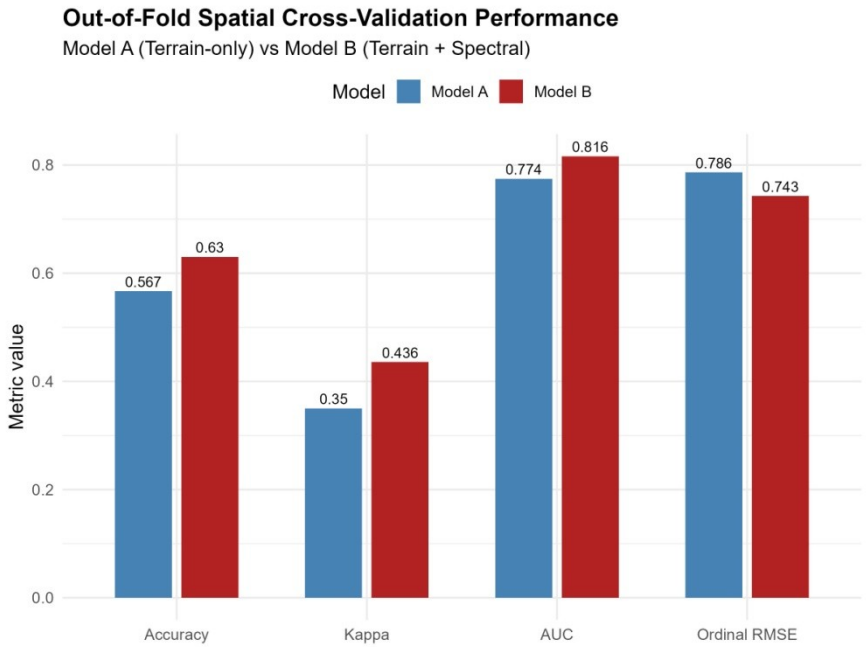


Figure 4.2.1: Out-of-fold spatial cross-validation performance metrics for Model A and Model B.

4.2.2. Confusion matrices

Table 4.2.2.1 and 4.2.2.2 reproduce the full out-of-fold confusion matrices for Model A and Model B respectively.

	Reference		
Prediction	**D3.1**	**D4**	**D5**
D3.1	**98**	**52**	**59**
D4	**28**	**118**	**17**
D5	**74**	**30**	**124**

Table 4.2.2.1: Model A out-of-fold confusion matrix (spatial CV).

	Reference		
Prediction	**D3.1**	**D4**	**D5**
D3.1	**79**	**23**	**39**
D4	**18**	**97**	**4**
D5	**33**	**11**	**42**

Table 4.2.2.2: Model B out-of-fold confusion matrix (spatial CV).

One detail in these two tables needs to be highlighted: the column totals are different from what a reader might assume given as supposedly balanced dataset of three-class. Reference totals of Model A are exactly 200 points per class, consistent with the full n = 600 stratified training set described in Section 3.4.2. Model B's reference totals, however, are 130 for D3.1, 131 for D4 and only 85 for D5 – which means D5 retained only 42.5% of its original 200 training points after the bare-soil masking step described in Section 3.5.3, compared with roughly 65% retention for both D3.1 and D4. This uneven retention is a direct, mechanical consequence of how much of each class's mapped extent actually satisfied the NDVI, BSI and MNDWI criteria of bare-soil and it becomes directly relevant to understanding the per-class results of D5 in the next subsection, since a shrunken and potentially less representative training sample for a single class can affect the classification performance of that class independently of whatever the spectral contributors themselves contribute.

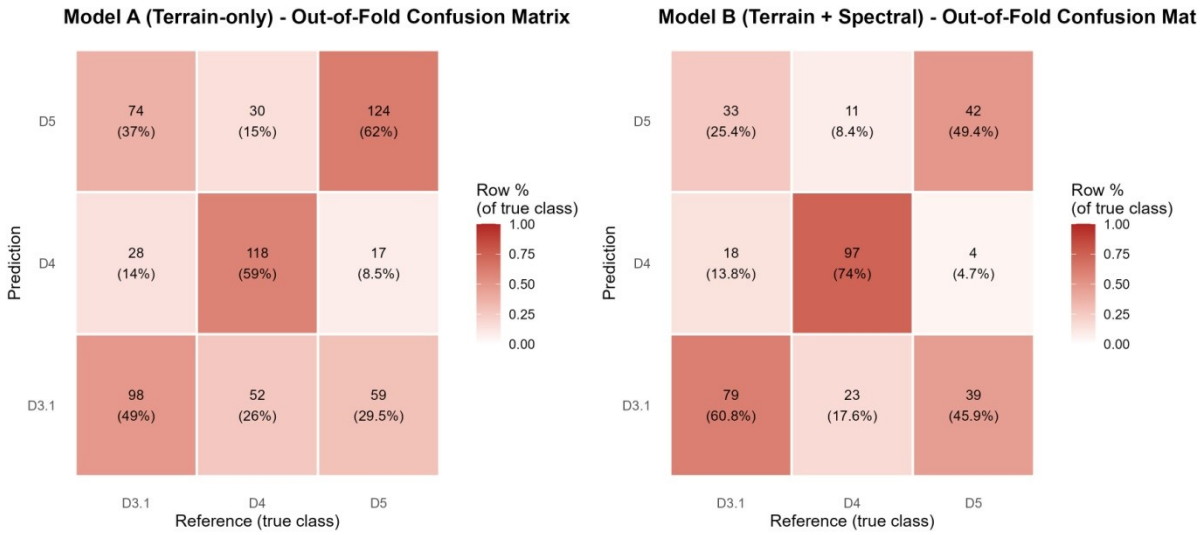


Figure 4.2.2: Out-of-fold confusion matrix heatmaps for Model A and Model B, spatial cross-validation

4.2.3. Per-class performance

Table 4.2.3 reports sensitivity, specificity and balanced accuracy by class for both models, drawn from the same output of confusion matrix.

Class	Model A Sensitivity	Model A Specificity	Model A Balanced Accuracy	Model B Sensitivity	Model B Specificity	Model B Balanced Accuracy
D3.1	0.4900	0.7225	0.606	0.608	0.713	0.660
D4	0.5900	0.8875	0.739	0.741	0.898	0.819
D5	0.6200	0.7400	0.680	0.494	0.831	0.663

Table 4.2.3: Per-class sensitivity, specificity, and balanced accuracy, Model A and Model B.

D4 is the best classified unit in Model A by every measure reported here, while D3.1 is the weakest. In Model B, D4 is still the strongest class by a clear margin, but the weakest class is changed from D3.1 to D5; Sensitivity of D5 falls from 0.620 in Model A to 0.494 in Model B, roughly a drop of 12.6 percentage points, even as D3.1's own sensitivity rises sharply, from 0.490 to 0.608, a gain of nearly 12 percentage points in the opposite direction.

It is important to clearly state this crossover rather than glossing over as a mixed result, because it points to two separate things which happen at once rather than one uniform improvement. Examining the confusion matrices directly, D3.1 and D5 are consistently each other's primary source of confusion in both models: In Model A, 37% of true D3.1 points are misclassified as D5 and 29.5% of true D5 points are misclassified as D3.1; the pattern is same in Model B with equivalent values of 30% and 38.8% respectively. In short, the same fundamental confusion exists between D3.1 and D5 even after adding spectral information – what changes is which of the two classes end up on the losing side of that confusion. Considering that D5 lost more than half of its original training points to the bare-soil mask while D3.1 and D4 lost only about a third, it is plausible that D5's declining sensitivity in Model B reflects, at least in part, a smaller and possibly less representative training sample for that specific class, rather than the spectral predictors themselves actively working against D5's separability. This hypothesis cannot be fully resolved with the evaluation metrics alone, but something to be stated clearly in this thesis; it is exactly the kind of pattern that cross-checking strategy against independent stratigraphic and mineralogical evidence is intended to help adjudicate in the discussion chapter that follows.

4.3. Variable Importance (Permutation Importance)

4.3.1. Ranked importance, Model A and Model B

As described in Section 3.7.2, permutation importance was computed using ten independent shuffles per variable and was calculated for every predictor in both models. Table 4.3.1 reports the mean accuracy drop and standard deviation for each variable, ranked from highest to lowest importance within each model.

Rank	Model A variable	Importance	SD	Model B variable	Importance	SD
1	Vdcn with torrents	0.2043	0.0121	LS factor	0.1058	0.0122
2	LS factor	0.1980	0.0115	Vdcn with torrents	0.1038	0.0128
3	Aspect	0.1022	0.0047	Slope	0.0289	0.0079
4	Slope	0.1012	0.0084	General	0.0188	0.0044

				curvature		
5	General curvature	0.0718	0.0058	Aspect	0.0150	0.0047
6	Profile curvature	0.0452	0.0070	Profile curvature	0.0095	0.0024
7	-	-	-	B3	0.0029	0.0014
8	-	-	-	B11	0.0026	0.0029
9	-	-	-	Ferrous index	0.0023	0.0023
10	-	-	-	B6	0.0003	0.0009

Table 4.3.1: Permutation importance (mean accuracy drop across 10 repeats ± SD), Model A and Model B.

In Model A, the top two predictors are vertical distance to channel network and the LS factor, which sits so close together that their confidence intervals, implied by the reported standard deviations, effectively overlap: together both of them account for approximately 62% of the combined importance across all six terrain predictors in this model. Whereas in Model B, the rankings flipped for these same two variables: the LS factor becomes the single most important predictor by a thin margin, with every other predictor including terrain or spectral falls well below both. None of the four spectral predictors come close to matching even the weakest importance of terrain variables; the strongest spectral predictor, B3, records an importance of only 0.0029, roughly forty times smaller than the value of LS factor in the same model.

One point worth mentioning plainly since it has a direct effect on the improved accuracy of Model B, reported in 4.2., should be understood. The spectral predictors are not, by this measure, doing much of the heavy work inside Model B; the terrain variable and specifically the LS factor are the dominant predictors of the classification behaviour of both models. The improvement in performance in Section 4.2 is more likely due to the combination of the spectral predictors that work alongside the terrain baseline and to the value-range and bare-soil masking refinements applied specifically to the data of Model B (Section 3.5.3 -3.5.4), rather than to any single spectral variable exerting strong independent influence of its own. This distinction matters for the discussion chapter, since it means the geological interpretation

derived from spectral variables of Model B, however their individual score are small, should not be inflated to claim they are primary drivers of the classification outcome.

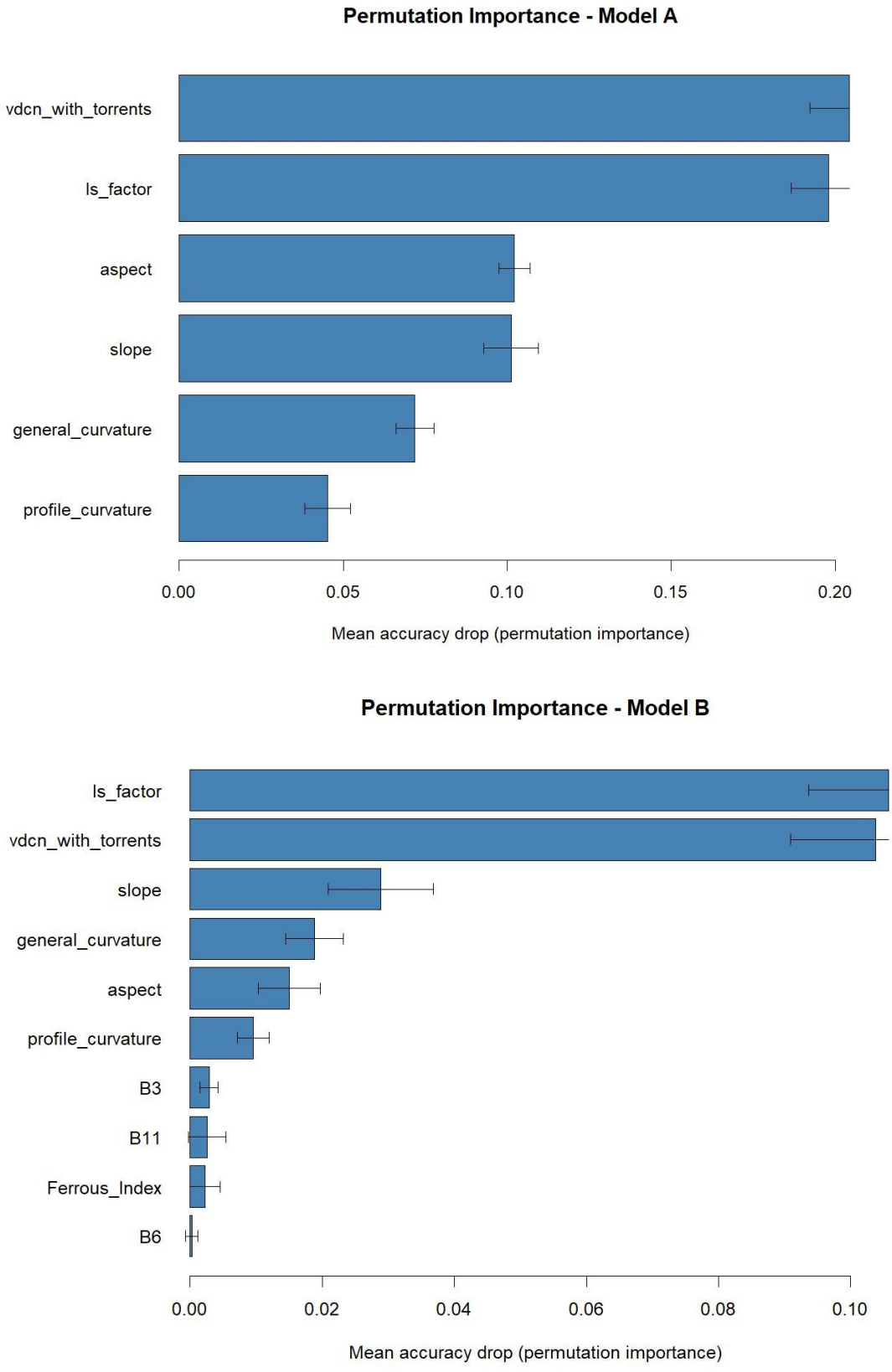


Figure 4.3.1: Permutation importance – Model A and Model B

4.4. Partial Dependence Plot (PDP)

Partial dependence curves were generated for every predictor that was retained in both models, following the procedure mentioned in Section 3.7.3 and are presented below ordered by permutation importance ranks as established in Section 4.3, from the predictor with the most influence down to the least. All values reported here were extracted from the underlying grid data rather than derived visually from the curves, to keep the reported numbers precise.

4.4.1. Model A (terrain-only)

Vertical distance to channel network (rank 1): The predicted probability of D4 is the highest very close to the channel network, which peaks at 0.574 at a distance of about 4.8 units, before falling steadily to a plateau around 0.21 beyond roughly 130 units. The D5 class shows a contrary trend, starting with a value at 0.176 before climbing to a maximum of 0.494 between 160° and 180°, remaining strong through much of the higher range. On the other hand, D3.1 remains mostly stable throughout which indicates fluctuations between about 0.29 and 0.42 without a clear monotonic trajectory. The crossover between D4 and D5 as the dominant class occurs somewhere between roughly 40 and 50 units of distance from the channel network.

LS factor (rank 2): The lowest end of the range is again dominated by D4, reaching 0.517 at the smallest observed LS factor value before dropping sharply; D5 shows the clearest and most consistent rise of the three classes, which climbs from 0.170 at the lowest value of LS factor to a peak of 0.442 at a value of roughly 8.5, before settling into a plateau around 0.40 for the remaining range. The curve of D3.1 is comparatively flat across the full range, which moves only between roughly 0.31 and 0.36. The crossover point where D5 overtakes D4 as the dominant class occurs at a very low value of LS factor, somewhere below approximately 5.

Aspect (rank 3): A noticeably less orderly pattern is produced by this variable than the two variables above: none of the three class curves show a single, simple monotonic trend across the compass range. D3.1 stands out at the two extremes, in the beginning (grid value equals to zero degrees) as well as in the end (close to 360 degrees), however, hitting local minimums

at 0.278 at roughly 118˚ degrees, while D5 class reaches a local maxima value at 0.398 between 130° and 140° respectively that allows it to defeat the other classes in this middle of the range. Although it is important to mention that this figure, which behaves like that has nothing definitive on its own – thus, there is no consistent and clear direction (such as north-south comparison etc.). It is noted as it is and will be explained in the discussion section.

Slope (rank 4): D4 once again has the highest position for the slopes close to the horizontal-axis (0.441) but then reduces to approximately 0.251 with the slope of around 12.5. Slightly better is the fifth dataset (D5) that starts from the lowest slope value of 0.210 and reaches the value of 0.390 with the slope of about 24, meaning it has surpassed D4 at some point between the slope values of around 5 and 10. D3.1 remains in a comparatively narrow band throughout, between roughly 0.34 and 0.39.

General curvature (rank 5): A sharp, narrow feature is observed in this variable, concentrated in a very small window immediately around a curvature value of zero: D3.1 rises to a local maximum of 0.383 at a curvature value of roughly 0.0036, while D5 simultaneously drops to a local minimum of 0.289 at that same point, before both curves partially reverse just a short distance further along the grid. This narrow and sharply peaked feature is worth mentioning separately, since it is concentrated in a very small fraction of the total curvature range rather than representing a broad trend and should be interpreted carefully rather than treated as a robust, wide-ranging signal.

Profile curvature (rank 6): The most concave (negative) end of the range is dominated by D4, at 0.360, while the most convex (positive) end is dominated by D5. The transition between the two is fairly abrupt, which occurs within a narrow band close to zero curvature, similar to the sharp transition witnessed for general curvature above.

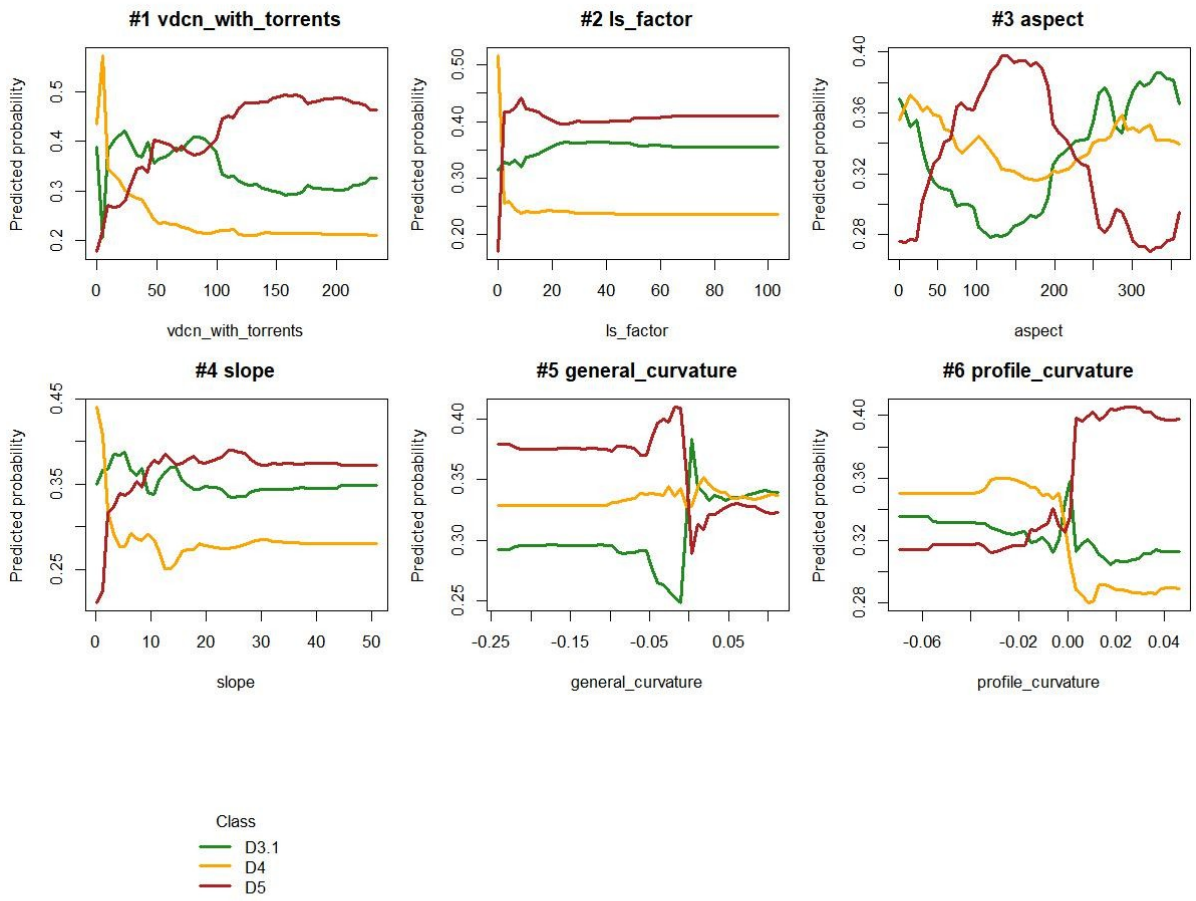


Figure 4.4.1: Partial dependence curves of Model A

4.4.2. Model B (terrain with spectral)

LS factor (rank 1): The pattern is very similar to Model A: D4 peaks at 0.528 at the lowest value of LS factor before falling sharply, while D5 rises from low of 0.159 to a peak of 0.372 around a value of roughly 8.2, which becomes the dominant class for LS factor values above roughly 5. D3.1 remains in a moderate range of 0.31 and 0.45 throughout, with a local peak of 0.446 at a low-to-moderate value of LS factor of roughly 0.44.

Vertical distance to channel network (rank 2): At the distance near zero, D4 dominates again with its peak at 0.571, before dropping to a plateau near 0.29 at larger distances. Somewhat differently from Model A, it is D3.1, not D5, that becomes the dominant class at the far end of the range in Model B, which reaches 0.472 around a distance of roughly 26 and remaining

the highest of three classes across most of the upper range, with D5 having a more gradual rise and only briefly exceeding D3.1 around a distance of roughly 197.

Slope (rank 3): At the lower slope values, D4 dominates (0.468 near zero), which drops to a low of 0.284 around a slope of approximately 5.2. D5 rises from 0.153 at the lowest slope value to a peak of 0.370 around a slope of roughly 22, which overtakes D4 as the dominant somewhere in the band between 5 and 12.

General curvature (rank 4): Similar to Model A, this variable has a sharp and narrow feature close to curvature zero: D3.1 peaks at 0.428 at a curvature of roughly 0.0044, while D5 drops at the same time to a local minimum of 0.207 at essentially the same point, again concentrated within a very narrow window of the overall curvature range and stating the same caution as mentioned for this variable in Model A.

Aspect (rank 5): Across the entire aspect range in Model B, D3.1 is the dominant class, unlike the more mixed pattern observed in Model A, which stays above other classes from the start of the range through to the end. The second most probable class throughout is D4, while D5 remains lowest across almost the whole range and only rises at a local peak of 0.280 around 141°.

Profile curvature (rank 6): D3.1 peaks at a curvature value close to zero (0.0012) with a probability of 0.411, while D4 dominates at the most negative (concave) end of the range at 0.382, and a gradual rise is observed in D5 toward the most positive (convex) end, which reaches 0.286 at the highest observed value.

B3, green band (rank 7): There is monotonic rise seen in D3.1 as B3 reflectance increases, from 0.279 at the lowest observed value to 0.404 at the highest, which overtake D4 as the dominant class somewhere around a B3 values of approximately 0.15 to 0.18. There is a fairly steady fall in D4 from 0.449 down to a plateau near 0.36. D5 remains comparatively flat and low throughout, between band 0.22 and 0.27.

B11, SWIR band (rank 8): D4 dominates at the lowest B11 values (0.423), which falls to a low of 0.369 before partially recovering to 0.379 at the highest observed value. D3.1 increases from 0.319 to a peak of 0.395 around B11’s mid-range value of roughly 0.27, then

declines slightly toward the end of the range. The curve of D5 rises gradually and close to monotonically across the full range, from 0.258 to 0.280, the most consistent upward trend of the three classes for this variable, though the overall magnitude of the change remains modest.

Ferrous Index (rank 9): It is worth mentioning this variable separately as counterintuitive, as D4, not D5, is the class most consistently favoured by rising values of the Ferrous Index, which reaches a peak probability of 0.424 at a Ferrous Index values of approximately 1.61, while the curve of D5 is comparatively flat and non-monotonic across the range, reaching a maximum of only 0.276 near the lower values of the range and never generating a clear upward trend of its own. Considering that Section 3.3.4 specified the Ferrous Index as detecting a chemically distinct form of iron mineralogy from the SAM-identified goethite discussed elsewhere in this thesis, this pattern is reported here as observed, without further interpretation; whether this reflects a genuine distinction in mineralogy, a modest and possibly unstable statistical effect given that very low permutation importance of the Ferrous Index reported in Section 4.3, or some other cause is left for thorough cross-checking.

B6, red-edge band (rank 10): As per the permutation importance results of Model B, the weakest predictor also produces the flattest PDP curves of any variable reported here: D4 declines only mildly from 0.431 to a plateau near 0.37-0.39, D3.1 rises only mildly from 0.334 to a peak of 0.398, and D5 remains uniformly low and largely flat between approximately 0.23 and 0.27 across the entire range. Among all these curves, their near-flatness is consistent with, and helps corroborate, the near-zero permutation importance values of this variable already reported in section 4.3.

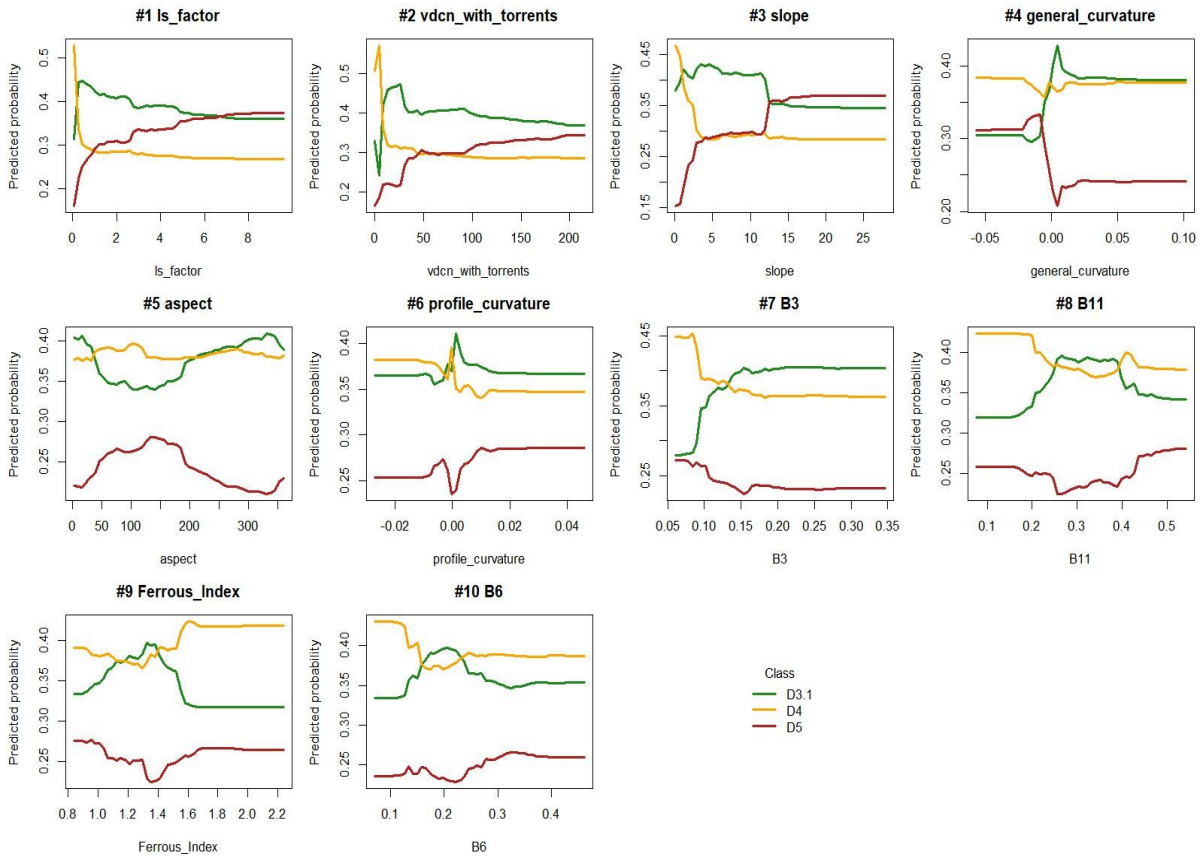


Figure 4.4.2: Partial Dependence curves of Model B

4.5. Spectral Mineralogy Results

4.5.1. Overall mineral-match frequency

As described in Section 3.4.3, Spectral Angle Mapper matching was applied to all 24 field samples against the filtered USGS Spectral Library Version 7 reference set (Kokaly et al., 2017). Table 4.5.1 reports the resulting first-match mineral frequency across the full sample set.

Sample	First Match	First SAM deg	Second Match	Second SAM deg	SAM Difference deg
1	Goethite	1.4963921651811618	Illite	2.6631917741993476	1.1667996090181858
10	Microcline	1.4608914882479338	Illite	1.5314828151565874	0.070591
11	Illite	1.6826855025001761	Illite	1.9053749833864189	0.22268948088624274
12	Montmorillonite	1.6623588517248482	Illite	2.0194649711434227	0.3571061194185745

13	Goethite	1.767509404477247	Illite	1.9951742038572775	0.22766479938003048
14	Illite	1.5397426409155264	Illite	1.7981250999633784	0.25838245904785206
15 A	Illite	1.6059935054712584	Microcline	1.6438088578793268	0.037815
15 B	Illite	1.5204045131758086	Illite	1.7207389027998057	0.20033438962399708
16 A	Goethite	1.7790691688490365	Illite	1.8935236950802194	0.11445452623118291
16 B	Microcline	1.6228673557489885	Microcline	1.6603354040499951	0.037468048301006585
17	Microcline	1.5211973796157903	Microcline	1.6243726257156317	0.10317524609984141
18	Microcline	1.7045250357717645	Microcline	1.7118519032575414	0.007327
1B	Illite	1.427975427937041	Illite	1.7068613429572228	0.2788859150201819
2	Illite	1.7100230168663437	Illite	1.8796928005494795	0.1696697836831358
3	Microcline	1.3566732074728842	Microcline	1.5629485253495539	0.20627531787666964
4	Goethite	1.7673494190326398	Illite	1.9410264336804082	0.1736770146477684
5C	Illite	1.908542496008216	Goethite	1.963801454846794	0.055259
5B	Goethite	1.8832634838418658	Montmorillonite	2.6095121732849504	0.7262486894430846
5A	Illite	1.9309447690106234	Montmorillonite	1.9867089164194611	0.055764
6A	Illite	1.4232319181037754	Illite	1.6752230859486177	0.2519911678448423
6B	Microcline	1.532282584868996	Microcline	1.6865285331628144	0.15424594829381832
7	Illite	1.4097937720896994	Illite	1.607454101068996	0.19766032897929664
8	Microcline	1.4166080580172664	Microcline	1.7334359076702281	0.31682784965296173
9	Goethite	2.0865800553388025	Montmorillonite	2.1496429496418097	0.063063

Table 4.5.1: First-ranked SAM mineral match frequency across all 24 spectroscopy samples.

Altogether, Illite and microcline account for 70.9% of all first-ranked matches, which establishes a phyllosilicate- and feldspar-dominated spectral signature as the norm across the

sample set as a whole, with goethite that represents a smaller but still notable secondary presence and montmorillonite appearing only once, in a single sample.

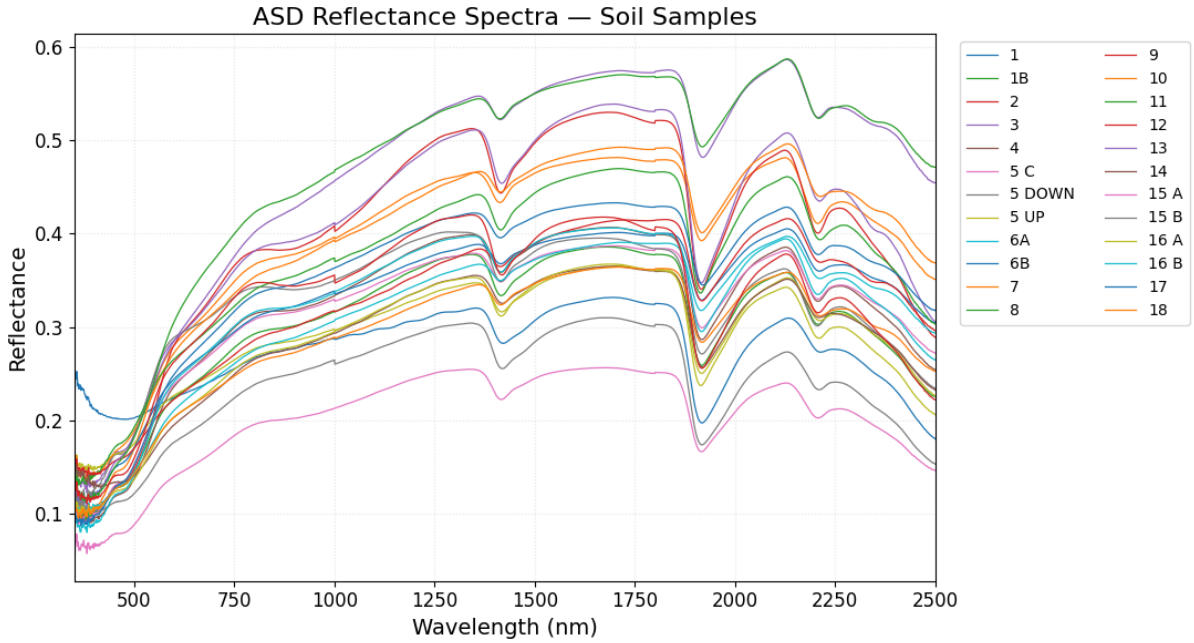


Figure 4.5.1: Full-range (350–2500 nm) reflectance spectra of all 24 field samples; The samples 5 UP and 5 DOWN refers to 5A and 5B respectively

4.5.2. SAM angle statistics

Spectral matching against the filtered USGS reference library resulted in four dominant first-match mineral groups: illite, microcline, goethite and montmorillonite (Table 4.5.1). Illite was the most frequent first match, occurring in 10 of the 24 samples (41.7%), followed by microcline in 7 samples (29.2%), goethite in 6 samples (25.0%), and montmorillonite in 1 sample (4.2%).

The distribution of first matches indicates that illite and microcline were the dominant spectral correspondences, together accounting for approximately 71% of the samples analyzed. Goethite represented an additional frequent spectral match, whereas montmorillonite was identified as the best correspondence for only one sample (12).

The first-match SAM angles ranged from 1.36° to 2.09°, with an average value of approximately 1.63°. The lowest SAM angle was obtained for 3 against microcline (1.36°), followed by 1B against illite (1.43°), 6A against illite (1.42°), 8 against microcline (1.42°),

and 7 against illite (1.41°). The largest first-match angle was observed for 9, for which goethite provided the closest reference spectrum (2.09°).

The second-ranked matches were generally dominated by the same mineral groups. Illite occurred as the second match in 13 samples, microcline in 7 samples, montmorillonite in 3 samples, and goethite in 1 sample. This strong recurrence of illite and microcline among both first- and second-ranked matches indicates that these minerals generated spectral responses that were frequently similar to those of the analyzed soil samples within the selected SWIR interval.

However, the difference between the first- and second-ranked SAM angles varied substantially among samples. For most samples, the difference was relatively small, indicating that more than one reference spectrum provided a comparable spectral correspondence. Particularly small differences were observed for 18 (0.007°), 16B (0.037°), 15A (0.038°), 5C (0.055°), 5A (0.056°), 9 (0.063°), and 10 (0.071°). Conversely, 1 showed the largest separation between the first and second matches (1.167°), followed by 5B (0.726°) and 12 (0.357°).

These results indicate that the confidence associated with the spectral assignment varied among samples. Samples with a relatively large separation between the first and second matches showed a clearer numerical preference for the first-ranked reference spectrum. In contrast, the very small differences observed for several samples indicate that the corresponding first matches should be interpreted cautiously because alternative reference spectra produced nearly equivalent SAM angles.

4.5.3. Per-class mineral association

The breakdown of first-match mineral is reported in Table 4.5.3, specifically for the three loess classes examined throughout this thesis, based on the sample-to-class correspondence confirmed against the records of field sampling (Section 3.4.1).

Class	n	Illite	Microcline	Goethite	Montmorillonitee
D3.1	4	2	1	1	0

D4	3	1	1	1	0
D5	3	1	1	0	1

Table 4.5.3: First-ranked SAM mineral matches by loess class.

There is no single dominant mineral group detected in any of the three loess classes; each returns a small, genuinely mixed spread across the available sample size, which itself is a first result worth stating plainly; with only three or four samples per class, no class in this dataset produces a clean, one-mineral signature. However, there is one class-specific zero-match pattern that does emerge cleanly is this: D3.1 and D4 both returned zero matches of montmorillonite, while D5 is the only one of three loess classes to return zero goethite matches, with its one montmotillonite match (sample 12) instead standing out as the sole occurrence of that mineral across the entire dataset of 24 samples for any of the three loess classes.

Apart from the three loess classes, the remaining context classes show somewhat more internally consistent patterns: D6 (n=4) returns illite in three of its four samples and goethite in the fourth, with zero matches of microcline and montmorillonite; D7 (n=4) shows the reverse pattern, with microcline in three of its four samples and goethite in the fourth, which return zero matches of illite and montmorillonite. These two context classes each show a considerably cleaner tendency of single-mineral than any of the three loess classes do, though the central analysis of this thesis concerns D3.1, D4 and D5 specifically, and this contrast between the loess and context classes is noted here descriptively rather than pursued further.

4.5.4. Soil reflectance spectra

The measured soil samples exhibited distinct but broadly consistent spectral responses across the 350–2500 nm range (Figure 4.5.1). The reflectance increased with the decrease of wavelengths from the visible to the near infrared but the absolute values of reflectance of the various samples appear to vary considerably. At approximately 500 nm the reflectance values differ from lower than two decimals to slightly over 0.25, while the highest reflectance values in the VNIR–SWIR region reached about 0.55–0.58 for the samples characterized by the highest brightness.

Several absorption features were consistently observed across the samples. A broad decrease in reflectance was evident near approximately 1400 nm, followed by a pronounced absorption feature around 1900 nm. These features are characteristic of water-related absorptions and are commonly observed in spectra of soil and mineral materials. The noticeable additional spectral features can be found in the range of 2000 to 2450 nm, where the differences between the samples are more pronounced and the mineral-specific absorption bands can be found.

The samples differed considerably in their overall reflectance magnitude while maintaining relatively similar spectral shapes. For example, samples with higher absolute reflectance generally exhibited the same major absorption regions as lower-reflectance samples. This indicates that differences in spectral brightness were superimposed on a common mineralogical and compositional spectral structure. The variability in overall reflectance may reflect differences in mineral composition, particle properties and other sample characteristics, whereas the absorption features provide more diagnostic information for mineralogical interpretation.

The SWIR spectra (Figure 4.5.4) showed greater separation among samples than the full-spectrum representation. In particular, differences in spectral curvature and absorption depth between approximately 2000 and 2250 nm were evident among the samples. This spectral interval therefore provided the basis for the subsequent comparison with the USGS reference spectra.

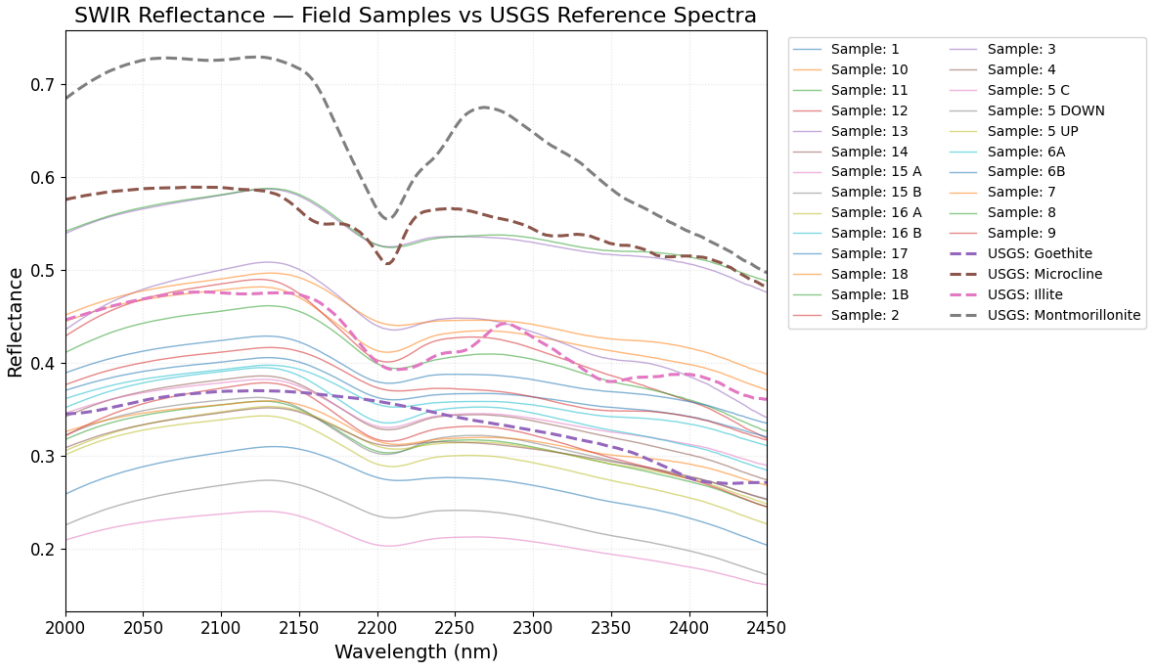


Figure 4.5.4: Shortwave-infrared (2000–2450 nm) reflectance spectra of all samples plotted against their corresponding first-ranked USGS Spectral; The samples 5 UP and 5 DOWN refers to 5A and 5B respectively

4.5.5. Mineralogical interpretation

The spectral matching results suggest that the investigated soils contain, or are spectrally influenced by, a combination of phyllosilicate, feldspar and iron-oxide spectral components. The predominance of illite among the first-ranked matches is consistent with the strong contribution of clay-mineral spectral features in the SWIR region. Illite and related mica-group minerals exhibit diagnostic absorption features associated primarily with Al–OH bonds, which occur within the SWIR domain and can therefore contribute substantially to the spectral response of fine-grained soil materials.

The recurrent identification of microcline as either the first or second match indicates an important feldspar-like component in the spectra. This result should, however, be interpreted as spectral correspondence rather than direct evidence of pure microcline. In natural soil samples, feldspars commonly occur together with quartz, clay minerals and other silicate phases, and the measured spectrum consequently represents a mixed response.

Similarly, goethite was identified as the first match in six samples. The occurrence of goethite is spectrally plausible because iron oxides can strongly influence soil reflectance, particularly in the visible and VNIR regions, through electronic transitions associated with Fe. The samples for which goethite was the first match therefore potentially reflect a stronger

contribution from iron-bearing phases compared with samples dominated by phyllosilicate or feldspar-like spectral responses.

Montmorillonite was identified as the first match only for 12. Nevertheless, it occurred as a second-ranked match for 5B, 5A and 9. This suggests that smectite-related spectral characteristics may be present in some samples but were generally less strongly expressed than the spectral characteristics represented by illite, goethite or microcline.

Importantly, the spectral results do not support the interpretation of the samples as mineralogically pure materials. The relatively small differences between the first- and second-ranked matches observed for several samples are consistent with mixed spectral contributions and/or similarities among the reference spectra. In particular, the occurrence of the same mineral as both first and second match for several samples likely reflects the presence of multiple USGS reference spectra representing the same mineralogical group rather than evidence for two independent mineral phases. Consequently, the SAM results are best interpreted as identifying the dominant spectral affinities of the samples rather than providing quantitative mineralogical proportions.

The visual comparison between the measured spectra and the USGS references further supports this interpretation. In the 2000–2450 nm interval, the reference spectra reproduce some of the broad spectral characteristics of the samples, but differences in absolute reflectance and spectral curvature remain apparent (Figure 4.5.4). Such differences are expected when comparing natural soil mixtures with individual mineral reference spectra and emphasize the importance of considering the SAM results together with the observed absorption features rather than treating the numerical ranking as a definitive mineralogical determination.

4.6. Particle-Size (Texture) Results

4.6.1. Class-mean texture

Table 4.6.1 reports the class-mean, grain-size mode and the mean clay, silt and sand percentages across all eighteen field samples, derived from the Malvern Mastersizer 3000 particle-size analysis described in Section 3.4.4.

Class	Mean mode (μm)	Mean clay %	Mean silt %	Mean sand %
D2	5.85	30.67	61.85	7.48
D3.1	14.34	30.15	63.96	5.89
D4	9.52	39.60	49.26	10.89
D5	15.24	23.24	68.77	7.47
D6	14.44	14.62	74.79	9.32
D7	12.12	21.68	69.90	7.45

Table 4.6.1: Class-mean mode and clay/silt/sand fraction percentages, all six sampled loess classes.

Limiting the focus to the three loess classes, D4 stands apart from D3.1 and D5 with a comparatively higher percentage of mean clay (39.60%) and correspondingly lower percentage of mean silt (49.26%), while D3.1 and D5 are considerably closer to one another in their class-mean values, with D5 showing the highest content of mean silt (68.77%) and lowest content of mean clay (23.24%) of the three. This order is worth flagging, D4 as the most clay-rich and D5 as the most silt-rich, as a specific and comparative statement rather than a general remark about difference in texture across classes, since it directly shapes the sample-level detail discussed next.

4.6.2. Sample-level detail and specific outliers

The individual sample values for the three loess classes are reported in Table 4.6.2, derived directly from the statistics of particle-size distribution and shape parameters computed for each sample (Section 3.4.4), calculated following the graphical method of Folk and Ward (1957) for sorting, skewness and kurtosis.

Class	Sample	Mode (μm)	Clay %	Silt %	Sand %	Skewness	Sorting
D3.1	1	5.49	31.44	68.56	0.00	Fine Skewed	Poorly Sorted
D3.1	2	0.640	45.61	48.01	6.38	Coarse	Very

						Skewed	Poorly Sorted
D3.1	3	36.9	13.41	75.30	11.29	Strongly Fine Skewed	Poorly Sorted
D4	7	6.89	22.14	61.82	15.46	Coarse Skewed	Very Poorly Sorted
D4	8	21.1	15.12	75.43	9.29	Fine Skewed	Very Poorly Sorted
D4	9	0.563	81.54	10.53	7.91	Strongly Coarse Skewed	Poorly Sorted
D5	10	21.9	22.40	70.78	6.39	Fine Skewed	Very Poorly Sorted
D5	11	17.2	27.09	65.60	7.31	Near Symmetrical	Very Poorly Sorted
D5	12	6.62	20.22	69.92	8.71	Near Symmetrical	Very Poorly Sorted

Table 4.6.2: Sample-level particle-size detail, D3.1, D4, and D5.

The clay enrichment of D4 class-level noted above turns out, at the sample level, to be driven almost entirely by a single sample rather than highlighting a uniformly clay-rich class. Sample 9 returned 81.54% clay, which is the highest clay recorded anywhere in the three loess classes by far, alongside the finest mode of the entire dataset (0.563 μm) and a strongly coarse-skewed, very leptokurtic distribution shape. The other two samples of D4, 7 and 8, are silt-dominated (61.82% and 75.43% respectively) and sit much closer to the D3.1 and D5 sample in overall character. Thus, the class mean of D4 is not representative of a typical D4 sample; it is instead an average pulled sharply upward by one atypical, extremely clay-rich

outlier sitting alongside two samples that would otherwise look unremarkable next to D3.1 or D5.

The widest internal spread among the three loess classes without a single extreme outlier of sample 9's magnitude is shown by D3.1; sample 2 returns 45.61% clay against sample 3's 13.41%, a difference of over 32 percentage points within the same nominal class, with sample 1 residing in between at 31.44%. The samples of D3.1 also showed the widest range of grain-size modes of any loess class, from 0.640 μm (sample 2) to 36.9 μm (sample 3), which spans more than two orders of magnitude.

D5 is the most internally consistent of three loess classes: its cluster of three samples within a comparatively narrow silt range (65.60% to 70.78%) and a similarly narrow range of clay (20.22% to 27.09%), with no sample approaching a similar extreme as observed in D4's sample 9 or the widespread seen across the three samples of D3.1.

4.6.3. USDA texture classification

Table 4.6.3 reports the USDA texture class assigned to each of the eighteen field samples, based on their fraction percentages of clay, silt and sand, classified according to the standard USDA soil texture scheme, itself grounded in the broader clay/silt/sand-based quantitative framework for describing soil texture (Shirazi & Boersma, 1984).

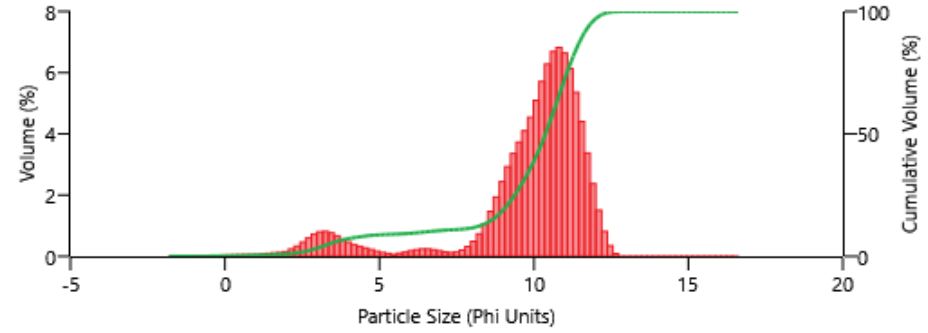
SAMPLE	LOESS CLASS	SOIL TEXTURE
1	D3.1	Silty clay loam
1B	D3.1	Silt
2	D3.1	Silty Clay
3	D3.1	Silty Loam
4	D2	Silty clay loam
5A	D2	Silty clay
5B	D2	Silty clay loam
5C	D2	Silty loam
6A	D2	Silty loam
6B	D2	Silty clay loam

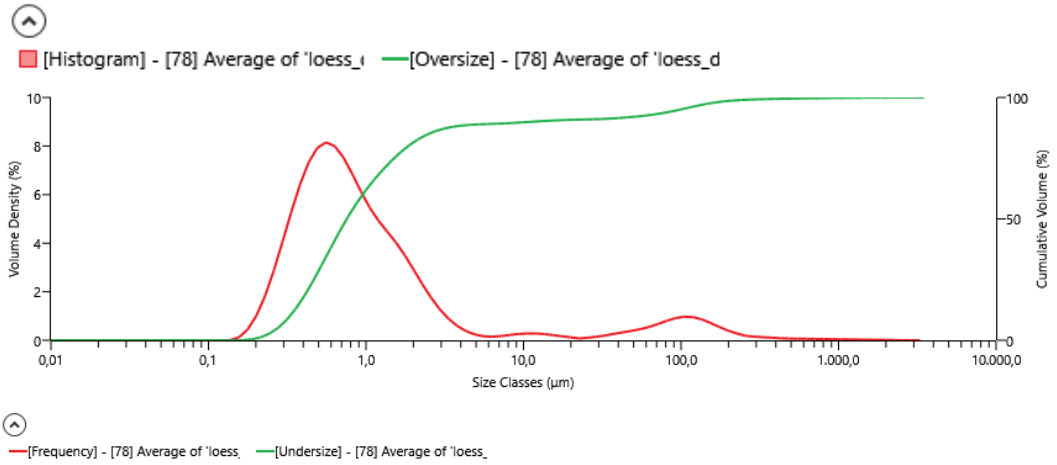
7	D4	Silty loam
8	D4	Silty loam
9	D4	Clay
10	D5	Silty loam
11	D5	Silty clay loam
12	D5	Silty loam
13	D6	Silty loam
14	D6	Silty loam
15A	D6	Silty loam
15B	D6	Silty loam
16A	D7	Silty loam
16B	D7	Silty loam
17	D7	Silty loam
18	D7	Silty clay loam

Table 4.6.3: USDA texture classification, all eighteen field samples.

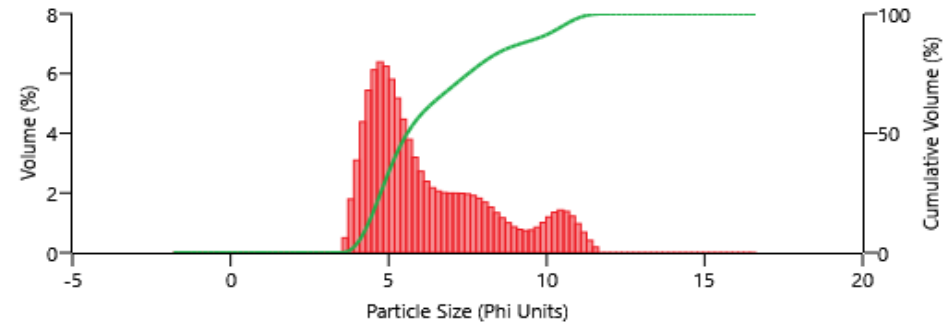
The clay dominant composition of Sample 9 is enough to push it into the "Clay" texture class outright, the only sample among all eighteen to fall into this class; among all six loess units, every other sample falls into a texture dominated by silt of one kind or another (silt, silty loam, silty clay loam or silty clay). From a standpoint of categorical classification rather than only from raw percentages, this confirms that sample 9 sits apart from the rest of the dataset rather than merely being a somewhat elevated value within an otherwise similar range.

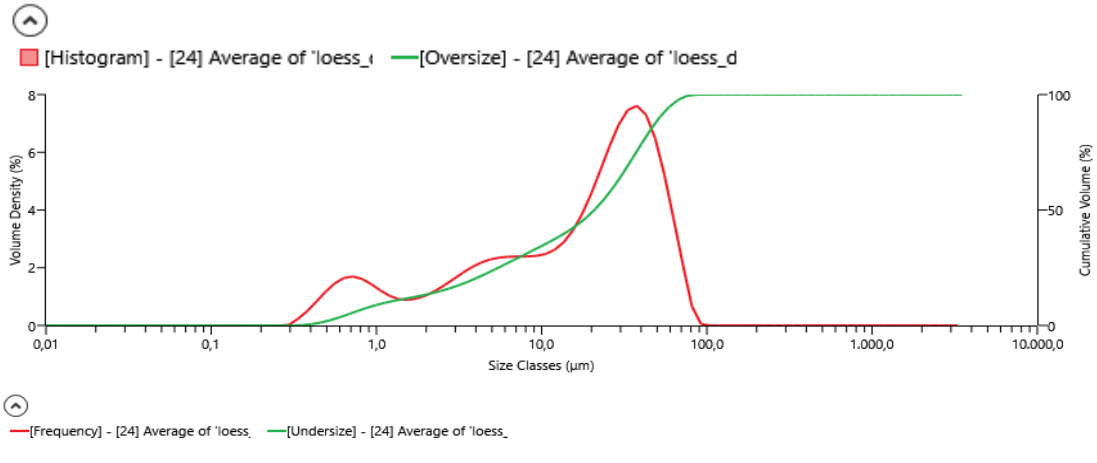
Sample 9 (D4, extreme outlier):





Sample 3 (D3.1, coarse silt-dominant):





Sample 12 (D5, representative of D5's tight internal clustering:

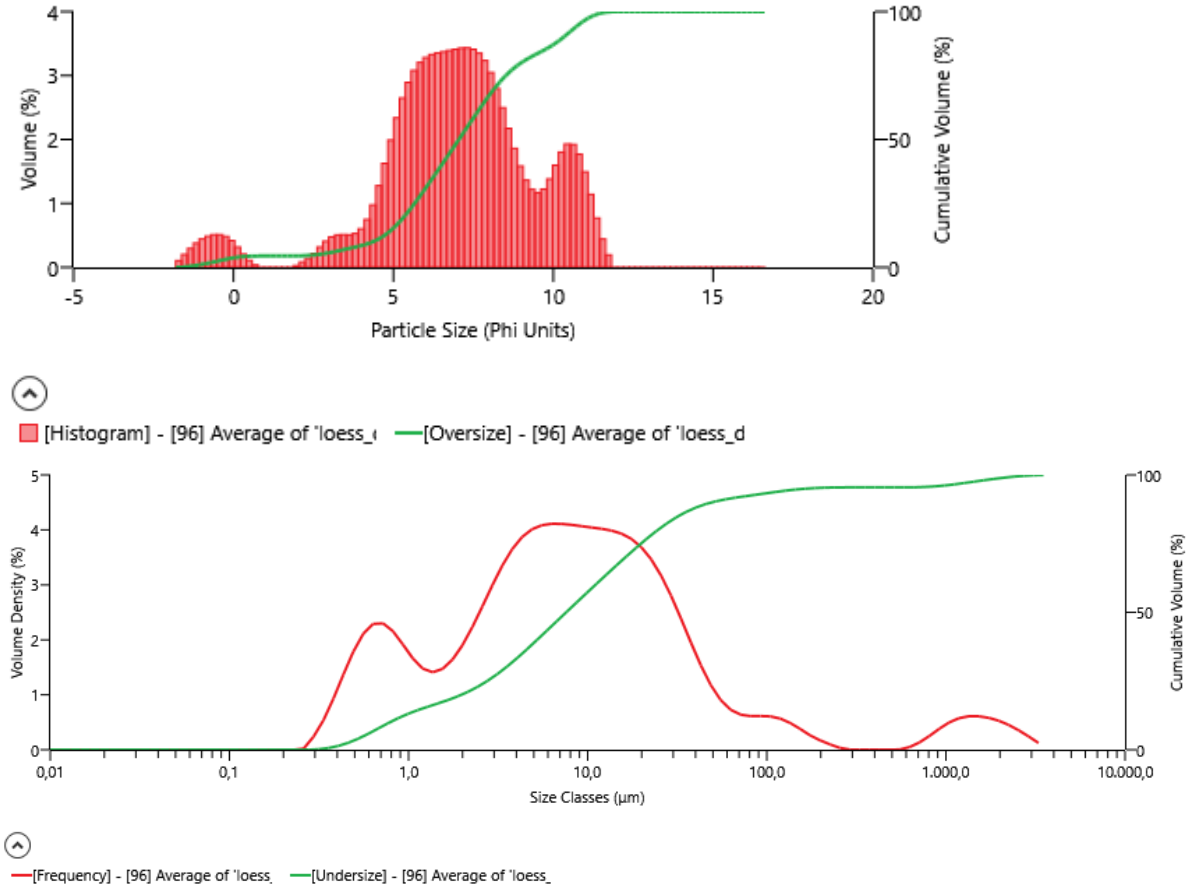


Figure 4.6.3. Representative Malvern Mastersizer 3000 particle-size distribution curves for samples 9, 3, and 12, illustrating the contrast between D4's clay-dominant outlier and the silt-dominant character of D3.1 and D5.

4.7.1. Categorical severity maps

Figure 4.7.1 shows categorical severity prediction of Model A across the full extent, without and with a hillshade base layer respectively, while Figure 4.7.1.2 show the equivalent output for Model B. Since predictions of Model B are restricted to the bare-soil-masked raster area described in Section 3.5.3, its mapped extent is comparatively smaller than Model A's, with large portions of the study area appearing masked out entirely rather than assigned to any class.

Across both models, the spatially dominant class by a wide margin is D4 (orange), which occupies the great majority of the flatter plain terrain in the northern and eastern section of the mapped extent. This aligns with the class-level pattern already established in Sections 4.2.2 and 4.2.3: D4 was the best-classified unit by sensitivity, specificity and balanced

accuracy in both models and it also carried the highest predicted probability across most of the terrain covariate space in the partial dependence results reported in Section 4.2.4, specially at low values of LS factor and slope. Therefore, the spatial dominance of D4 in these maps is aligned with, rather than a separate finding from, the statistical results already reported.

In comparison to other classes, D5 (red) is not distributed evenly across the mapped extent; it is concentrated specifically within the dissected, branching drainage network visible in the hillier southern section of the study area, which traces the dendritic pattern of incised valleys rather than appearing as a broad, continuous zone. It is a direct spatial concentration, visually confirmable match to D5's process description established in Cremaschi (1987): a piedmont glacis that is formed by erosional truncation, which would be expected to persist along zone of active or historical channel incision rather than across the flatter and less dissected plain where the aggradational loess cover of D4 remains largely intact. This is a case where the independent documented geomorphological process lines up with a model's raw spatial output.

D3.1 (green) occupies a comparatively narrow, roughly diagonal band which runs along what appears to correspond to the transition zone of Apennine piedmont, the boundary between the flatter plain to the north and the dissected hill terrain to the south, rather than being broadly scattered across the study area. In Model B, the mapped extent of D3.1 shrinks considerably relative to Model A, which appears only as a scattered patches rather than a continuous band, a direct visual consequence of the bare-soil masking step which removes large sections of vegetated or otherwise non-qualifying terrain from prediction surface of Model B entirely.

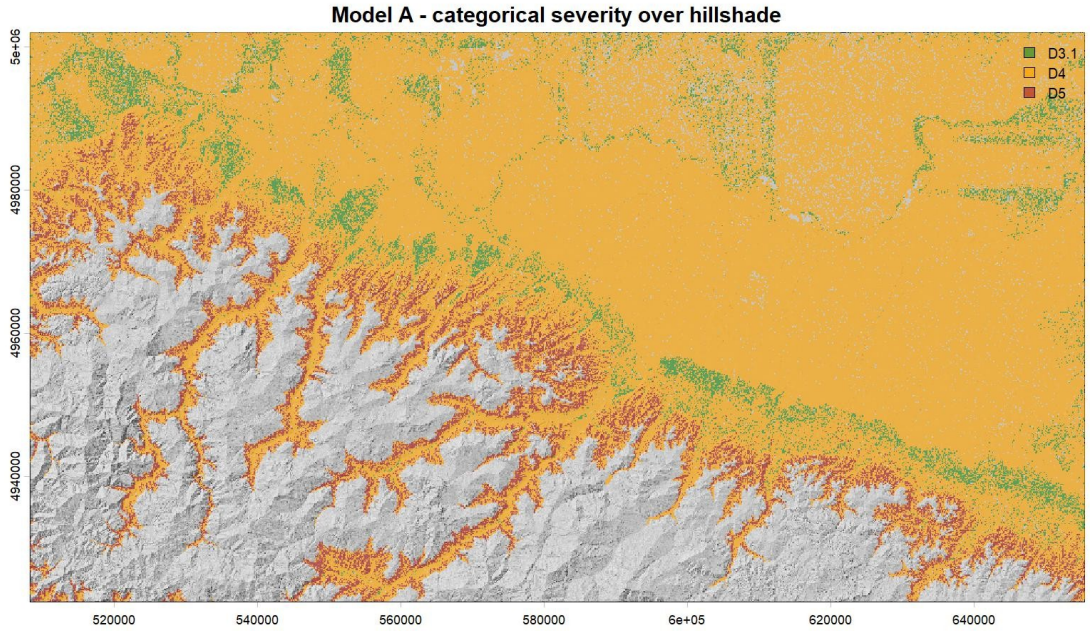
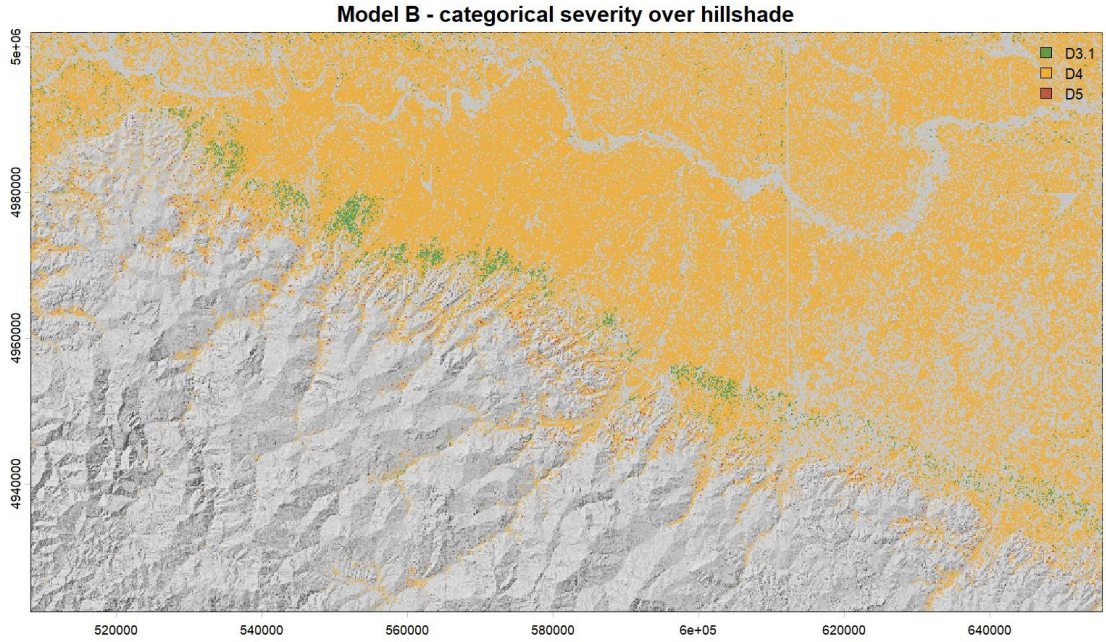


Figure 4.7.1: Categorical severity prediction for Model A across the full study extent: hillshade version



4.′ *Figure 4.7.1.2: Categorical severity prediction for Model B across the full study extent: hillshade version*

Figures 4.7.2 and 4.7.2.1 show the out-of-fold prediction correctness of individual reference points plotted over the hillshade base layer for both Model A and Model B, with correctly classified points shown as filled circles and misclassified points shown as crosses. In both models, essentially all reference points, correct and incorrect alike, are tightly clustered along the same narrow transition zone between the plain and the dissected hill terrain described

above, since this is where the mapped extent of the three focal classes converge; this is an expected consequence of the sampling design described in Section 3.4.2 rather than a finding in its own right.

However, a specific spatial pattern in the misclassification is visible within that shared zone rather than an even scattering of errors along the whole transect. In both models, the predictions of incorrect points (crosses) appear more denser in the central portion of the transition band, roughly in the middle third of the mapped transect, than at either the western or eastern ends, where correctly classified points (filled circles) are comparatively more concentrated. This pattern is consistent with a boundary-driven source of classification error, a phenomenon, well-documented in thematic land classification more broadly, in which rate of misclassification rise specifically at the interface between adjacent mapped classes due to effects of mixed-pixel and the genuine gradation of geomorphology that exists at real boundaries, rather than errors being distributed uniformly across a study area regardless of local context (Foody, 2002). Considering that the three loess classes are genetically distinct but spatially adjacent units along this same piedmont transition, a concentration of confusion specifically in the central portion of their shared boundary zone is a plausible manifestation of exactly this kind of boundary effect, rather than a random or unexplained clustering of errors.

Comparing the two models directly, the correctness map of Model B covers a visibly smaller footprint than Model A, which is consistent with the limitation of bare-soil mask discussed throughout this chapter, but the remaining points do not show a clear different spatial error pattern from Model A within the area shared by both models; the central-transect clustering of misclassifications described above appears in both maps rather being specific to one model or the other.

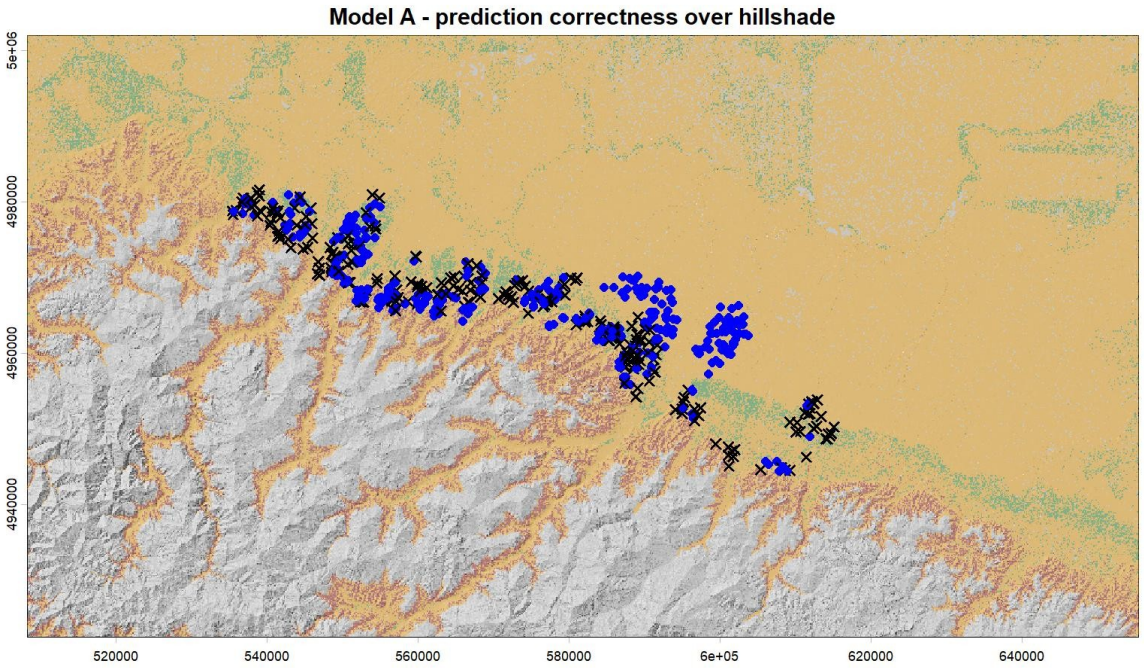


Figure 4.7.2: Out-of-fold prediction correctness for Model A, plotted over hillshade and categorical severity background, showing correct (filled circles) and incorrect (crosses) classifications concentrated along the Apennine piedmont transition zone

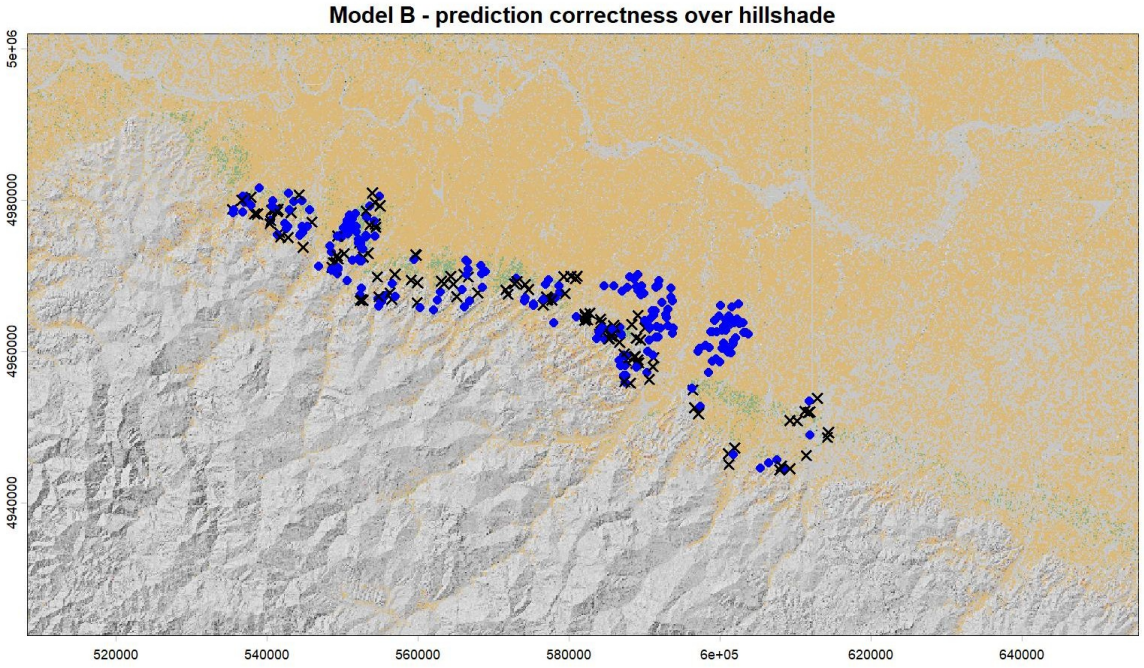


Figure 4.7.2.1: Out-of-fold prediction correctness for Model B, plotted over hillshade, showing the reduced spatial footprint resulting from bare-soil masking

5. Discussion

5.1. Model Performance and the Role of the Predictors

The study area lies on the Apennine margin of the Piacenza area, where Cremaschi (1987) mapped a sequence of Middle to Late Pleistocene units covered by the Ghiardo Loess. This thesis tested whether a legacy map trained by Random Forest could reproduce three of these units, D3.1, D4 and D5, from terrain derivatives alone (Model A) and from terrain plus spectral predictors (Model B). On all four metrics, Model B performed better than Model A, Accuracy increased from 56.7% to 63.0%, Kappa from 0.350 to 0.436 and AUC from 0.774 to 0.816, and the ordinal RMSE dropped from 0.786 to 0.743. Both models were well above the no-information rate. The spatially blocked cross-validation used here gives lower but realistic values than random cross-validation.

The increase in Model B did not come from individual spectral bands because their permutation importance ranged from (0.0003 to 0.0029), which is more than thirty times below the highest ranked predictor in the same model, LS factor (0.106). One possibility is that the spectral variables are doing real work, just not as individual predictors. Additionally, Model B was trained on 346 bare-soil points against 600 for Model A, so the two models differ in composition of sample as well as predictors. The improvement therefore cannot be assigned completely to the spectral data.

Most of the work was done by the terrain predictors. The vertical distance to channel network and LS factor were the two strong predictors in both models (Model A: 0.204 and 0.198; Model B: 0.104 and 0.106). VDCN captures differences in height and drainage position, which separates an erosional surface from a depositional or buried one. This is supported by the partial dependence plots for D5. According to the findings, the probability of D5 being present was higher when the slope and distance from the channel network increased. It was evident that D5 was positioned in accordance to the branching structure of the incised valley network, located mostly in the hilly regions. This aligns with Cremaschi (1987), who defines D5 as a piedmont glacis, an erosional surface cut across the folded and faulted formation of Pede-Apennine. Terrain attributes separated an erosional surface from aggradational units, and the model behaviour, the spatial pattern and the stratigraphy gave the same answer independently. D3.1 and D5 were confused as pair in both models. D3.1 samples were

predicted as D5 - 74 times in Model A and 33 times in Model B, and D5 samples were predicted as D3.1 – 59 and 39 times respectively. D3.1 and D5 lie on the same fluvial formation, D3.1 as a soil in its top and D5 as a surface cut across it and both are covered by Ghiardo loess. Due to similar landscape position and surface cover, it is hard to separate them with terrain and surface reflectance alone.

5.2. Geological Reading of the Units

Cremaschi (1987) describes D3.1 as the Collechio vetusol, a rubefied soil in the top of the Pede-Apennine formation that was later covered by the Ghiardo loess, so it predates the loess. The clay content of of D3.1 varies widely among the samples (13.4-45.6%), which fits the change he describes from a stone-free, clay-rich B21t horizon to stonier B3 horizons. The D4 samples were taken on the loess cover over the Borzano gravels, so their texture is most likely reflecting the loess. In table 4.6.3, Samples 7 and 8 are silt-dominated (61.8% and 75.4% silt), as expected for loess and for the Ghiardo loess, whose clay content ranges from 14% to 50% (Cremaschi, 1987). Sample 9 is an outlier with a clay content of 81.5%. Cremaschi (1987) reported fine-textured sediments at the top of the Borzano gravels and loess resting on fluvial clay in places, and either could explain it. The D5 samples are the most uniform (silt 65.6-70.8% and clay 20.2-27.1%).

Illite (10 of 24 samples) and microcline (7) were the most frequent SAM matches, followed by goethite (6) and montmorillonite (1). Illite is among the clay minerals reported for the Po Plain loess and vetusols (Cremaschi, 1987). Several samples have small margins between their first and second matches. The region of 2000-2450 nm can be identified primarily with various hydroxyl and clay components, while iron oxides mainly absorb in the visible and near infrared (Hunt, 1977; Clark, 1999). Therefore, goethite matches are weak evidence. They occur in D3.1 (sample 1) and D4 (sample 9), and not in D5 as mentioned in Table 4.5.1.

The Ferrous Index gave a weak pattern. Its permutation importance was 0.0023 ± 0.0023, and D4 gained probability above an index value of about 1.6 while D3.1 lost it. D5 stayed low and nearly flat. An iron signal was expected on D5 because erosion can expose weathering products, but Cremaschi (1987) describes D5 as covered by colluviums and loess, which would mask it. He documents iron accumulation in the D3.1 vetusol and in the loess cover

(Fe-Mn nodules and free iron up to 11-13%), but nothing that distinguishes D4 and D5. The Ferrous Index is designed to detect ferrous iron, or rather to trace the presence of reduced ferrous iron (Fe^{2+}) that is mainly present in certain silicates, particularly in pyroxenes and amphiboles. Whereas, goethite is a ferric oxide of iron (Fe^{3+}), so the two measures cannot be compared directly. X-ray diffraction of the D4 samples would be needed to test it.

5.3. Limitations and Future Perspectives

The usable training points of D5 were cut from 200 down to 85 due to the bare-soil mask, compared to roughly 65% for both D3.1 and D4. This might be most likely be the explanation for why the classification accuracy of D5 got worse in Model B even though the overall model improved; losing more than half its training data almost certainly cost D5 more than it gained from adding spectral information.

In the partial dependence result, both profile and general curvatures showed sharp, narrow spikes concentrated in a very small sliver of their overall range, right around a curvature value of zero. These narrow spikes should not be read the same way as the broad, gradually sloping trends observed for variables like LS factor or VDCN, since a spike concentrated in such a small part of the range is much more likely to be driven by a handful of unusual training points than to reflect a genuinely robust and wide-ranging relationship.

Several next steps follow from this work. Considering the texture profile documented in this thesis for these units, dominated by silt with relatively lower content of clay except in localised samples of D4 such as sample 9, which extends this modelling framework to erosion hazard potential, represents a natural next step. Silt-dominated, low-clay sediment of this kind is well established in the literature as highly susceptible to detachment and rill or gully initiation after the removal of surface protection, since the weak clay bridging between silt and grains provide little resistance to dispersion of particles under saturation (Zhuang et al., 2024). Random Forest classifiers built on slope, topographic wetness, distance to channel network and land cover have already being applied successfully to map erosion hazard potential in other loess-covered regions, which achieved strong discrimination (AUROC around 0.90) using largely the same terrain-derivative logic already tested in this thesis (Nokhandan et al., 2025). Since the LS factor, vertical distance to channel network and slope

already proved to be the dominant predictors separating an actively erosional surface such as D5 from the other units, the same stack of predictors used here could be improvised with slight modification into a dedicated erosion susceptibility model for the mapped loess units, rather than requiring an entirely modelling pipeline. Targeted mineralogical analysis, such as X-ray diffraction applied specifically to the D4 samples which drives the Ferrous Index association, would allow direct identification of the ferrous mineral phases present. An independent validation dataset designed from the outset with adequate sample sizes per class would allow the transferability of this modelling approach to broader geographic locations.

6. Conclusion

This thesis tested whether terrain and satellite data can reproduce the loess units of the Apennine margin mapped by Cremaschi (1987), using a Random Forest classifier trained on the legacy map. The study compared two models, one with terrain derivatives only and one with terrain derivatives plus Sentinel-2 spectral predictors.

The main finding is that terrain, not spectral data, distinguishes these units. The vertical distance to channel network, the LS factor and the slope were able to identify D5 as an erosional surface. However, adding spectral predictors improved the overall classification, but no single band or index mattered much and the change in sample composition means the spectral effect cannot be separated from the improvement. Therefore, D4 was the best-classified unit, D5 was the clearest to interpret, and D3.1 and D5 was the pair the model struggled to reliably separate, because they share the same formation and cover.

The reference labels come from a legacy map, so the model learns how the map was drawn not the ground itself. Therefore, agreement with the map is evidence that the map and the landscape are consistent with each other. Additionally, the cross-checking of model results with texture, mineralogy and the stratigraphy described by Cremaschi, treats the final output as a geological answer rather than a good accuracy score alone.

The results also points to a practical use. The units are mostly silt with little clay, and D5 is separated by the same terrain variables that are used in erosion hazard models. Therefore, the workflow built here could be implemented for an erosion susceptibility map of these loess units, without having to start from scratch.

In conclusion, the legacy map can be partly reproduced from terrain and spectral model, and the approach informs more about how the landscape was shaped than about the composition of the surface. The results for D5 and for the Ferrous Index need testing with larger samples and direct mineralogy before they are treated as settled.

Reference

1. Amadio, M. (2013). Flood risk assessment in the Po River basin under a climate change scenario [Master's thesis, Università Ca' Foscari Venezia]. Unive Thesis Repository. https://unitesi.unive.it/handle/20.500.14247/898
2. An, Zhisheng& Sun, Youbin& Zhou, Weijian& Liu, Weiguo&Qiang, Xiaoke& Wang, Xulong& Xian, Feng & Cheng, Peng & Burr, George. (2014). Chinese Loess and the East Asian Monsoon. https://doi.org/10.1007/978-94-007-7817-7_2
3. Andreetta, A., Benvenuti, M., Maestrelli, D., Carnicelli, S., & Sani, F. (2023). Quaternary deformations, palaeosols and strata across the Northern Apennines (Geological Field Trips and Maps, Vol. 15, No. 1.4). Servizio Geologico d'Italia - ISPRA & Società Geologica Italiana. https://doi.org/10.3301/GFT.2023.04
4. Antoine, Pierre & Rousseau, Denis-Didier &Zöller, Ludwig & Lang, Andreas &Munaut, André-Valentin & Christine, Hatté&Fontugne, Michel. (2001). High-resolution record of the last Interglacial-glacial cycle in the Nussloch loess-palaeosol sequences, Upper Rhine Area, Germany. Quaternary International. 76–77. 211–229. https://doi.org/10.1016/S1040-6182(00)00104-X
5. Batjes, N. H., Calisto, L., and de Sousa, L. M.: Providing quality-assessed and standardised soil data to support global mapping and modelling (WoSIS snapshot 2023), Earth Syst. Sci. Data, 16, 4735–4765, https://doi.org/10.5194/essd-16-4735-2024
6. Belgiu, M., & Drăguţ, L. (2016). Random forest in remote sensing: A review of applications and future directions. ISPRS Journal of Photogrammetry and Remote Sensing, 114, 24–31. https://doi.org/10.1016/j.isprsjprs.2016.01.011
7. Biddoccu, M., Guzmán, G., Capello, G., Thielke, T., Strauss, P., Winter, S., Zaller, J. G., Nicolai, A., Cluzeau, D., Popescu, D., Bunea, C.-I., Hoble, A., Cavallo, E., & Gómez, J. A. (2020). Evaluation of soil erosion risk and identification of soil cover and management factor (C) for RUSLE in European vineyards with different soil management. *International Soil and Water Conservation Research, 8*, 161–170. https://doi.org/10.1016/j.iswcr.2020.07.003
8. Birkeland, P. W. (1999). Soils and geomorphology (3rd ed.). Oxford University Press.
9. Bollati, I.M., Zerboni, A. The Po Plain Loess Basin (Northern Italy): Scientific Values, Threats, and Promotion Opportunities. *Geoheritage* **13**, 74 (2021). https://doi.org/10.1007/s12371-021-00596-2
10. Bordoni, M., Corradini, B., Lucchelli, L., Valentino, R., Bittelli, M., Vivaldi, V., &Meisina, C. (2019). Empirical and Physically Based Thresholds for the Occurrence of Shallow Landslides in a Prone Area of Northern Italian Apennines. Water, 11(12), 2653. https://doi.org/10.3390/w11122653
11. Bordoni, M., Vercesi, A., Maerker, M., Ganimede, C., Reguzzi, M. C., Capelli, E., Wei, X., Mazzoni, E., Simoni, S., Gagnarli, E., &Meisina, C. (2019). Effects of vineyard soil management on the characteristics of soils and roots in the lower Oltrepò Apennines (Lombardy, Italy). *Science of The Total Environment*, *693*, 133390. https://doi.org/10.1016/j.scitotenv.2019.07.196
12. Bosino, A., Giordani, P., Quénéhervé, G., &Maerker, M. (2020). Assessment of calanchi and rill–interrill erosion susceptibilities using terrain analysis and geostochastics: A case study in the Oltrepo Pavese,

Northern Apennines, Italy. *Earth Surface Processes and Landforms*, *45*(12), 3025–3041. https://doi.org/10.1002/esp.4949

13. Bosino, A., Omran, A., &Maerker, M. (2019). Identification, characterisation and analysis of the Oltrepo Pavese calanchi in the Northern Apennines (Italy). *Geomorphology*, *340*, 53–66. https://doi.org/10.1016/j.geomorph.2019.05.003
14. Breiman, L. Random Forests. Machine Learning 45, 5–32 (2001). https://doi.org/10.1023/A:1010933404324
15. Brus, D. J. (2019). Sampling for digital soil mapping: A tutorial supported by R scripts. Geoderma, 338, 464–480. https://doi.org/10.1016/j.geoderma.2018.07.036
16. Buma W, Abelev A and Merrick T (2024) Vegetation spectra as an integrated measure to explain underlying soil characteristics: a review of recent advances. Front. Environ. Sci. 12:1430818. https://doi.org/10.3389/fenvs.2024.1430818
17. Callesen I, Palviainen M, Armolaitis K, Rasmussen C and Kjønaas OJ (2023) Soil texture analysis by laser diffraction and sedimentation and sieving–method and instrument comparison with a focus on Nordic and Baltic forest soils. Front. For. Glob. Change 6:1144845. https://doi.org/10.3389/ffgc.2023.1144845
18. Callesen, I., Keck, H. & Andersen, T.J. Particle size distribution in soils and marine sediments by laser diffraction using Malvern Mastersizer 2000—method uncertainty including the effect of hydrogen peroxide pretreatment. J Soils Sediments 18, 2500–2510 (2018). https://doi.org/10.1007/s11368-018-1965-8
19. Caporali, E., Lompi, M., Pacetti, T., Chiarello, V., &Fatichi, S. (2020). A review of studies on observed precipitation trends in Italy. International Journal of Climatology, 41, E1-E25. https://doi.org/10.1002/joc.6741
20. Castaldini, D., Marchetti, M., Norini, G., Vandelli, V., &ZuluagaVélez, M. C. (2019). Geomorphology of the central Po Plain, Northern Italy. Journal of Maps, 15(2), 780–787. https://doi.org/10.1080/17445647.2019.1673222
21. Ciccarese, G., Corsini, A., Pizziolo, M., &Truffelli, G. (2016). Debris flows in Val Nure and Val Trebbia (Northern Apennines) during the September 2015 alluvial event in Piacenza Province (Italy).Bollettino Della Societa Geologica Italiana,41, 127–130. https://doi.org/10.3301/ROL.2016.110</div
22. Clark, R. N., Chapter 1: Spectroscopy of Rocks and Minerals, and Principles of Spectroscopy, in Manual of Remote Sensing, Volume 3, Remote Sensing for the Earth Sciences, (A.N. Rencz, ed.) John Wiley and Sons, New York, p 3- 58, 1999.https://clarkvision.com/science/principles-of-spectroscopy-clark-1999/
23. Congalton, R. G. (1991). A review of assessing the accuracy of classifications of remotely sensed data. Remote Sensing of Environment, 37(1), 35–46. https://doi.org/10.1016/0034-4257(91)90048-B
24. Conti, P., Cornamusini, G.,& Carmignani, L.(2020). An outline of the geology of the Northern Apennines (Italy), with geological map at 1:250,000 scale. Italian Journal of Geosciences, Volume 139 (2020) f.2, Pages 149-194, ISSN 2038-1719. https://doi.org/10.3301/IJG.2019.25
25. Cremaschi, M. (1987). Paleosols and vetusols in the central Po plain (Northern Italy): A study in Quaternary geology and soil development [Doctoral dissertation, University of Amsterdam]. Edizioni Unicopli.
26. D'Amico, M.E., Casati, E., Andreucci, S. et al. New dates of a Northern Italian loess deposit (Monte Orfano, Southern pre-Alps, Brescia). J SoilsSediments 21, 832–841 (2021). https://doi.org/10.1007/s11368-020-02860-4

27. Delpiano, Davide & Peresani, Marco & Bertola, Stefano & Cremaschi, Mauro & Zerboni, Andrea. (2019). Lashed by the wind. Short-term Middle Palaeolithic occupations within the loess-palaeosoil sequence at Monte Netto (Northern Italy). Quaternary International. 502. https://doi.org/10.1016/j.quaint.2019.01.026
28. Demattê, J. A. M., Fongaro, C. T., Rizzo, R., & Safanelli, J. L. (2018). Geospatial Soil Sensing System (GEOS3): A powerful data mining procedure to retrieve soil spectral reflectance from satellite images. Remote Sensing of Environment, 212, 161–175. https://doi.org/10.1016/j.rse.2018.04.047
29. Desmet, P. & Govers, Gerard. (1996). A GIS procedure for automatically calculating the USLE LS factor on topographically complex landscape units. Journal of Soil and Water Conservation. 51. 427-433. https://doi.org/10.1080/00224561.1996.12457102
30. Dormann, C. F., Elith, J., Bacher, S., Buchmann, C., Carl, G., Carré, G., et al. (2013). Collinearity: A review of methods to deal with it and a simulation study evaluating their performance. Ecography, 36(1), 27–46. https://doi.org/10.1111/j.1600-0587.2012.07348.x
31. Eshel, G., Levy, G. J., Mingelgrin, U., & Singer, M. J. (2004). Critical evaluation of the use of laser diffraction for particle-size distribution analysis. Soil Science Society of America Journal, 68(3), 736–743. https://doi.org/10.2136/sssaj2004.7360
32. F. Lehmkuhl, J.J. Nett, S. Pötter, P. Schulte, T. Sprafke, Z. Jary, P. Antoine, L. Wacha, D. Wolf, A. Zerboni, J. Hošek, S.B. Marković, I. Obreht, P. Sümegi, D. Veres, C. Zeeden, B. Boemke, V. Schaubert, J. Viehweger, U. Hambach. (2021). Loess landscapes of Europe – Mapping, geomorphology, and zonal differentiation. Earth-Science Reviews, Volume 215, 2021, 103496, ISSN 0012-8252. https://doi.org/10.1016/j.earscirev.2020.103496.
33. Fisher, A., & Hesse, P. P. (2019). The response of vegetation cover and dune activity to rainfall, drought and fire observed by multitemporal satellite imagery. Earth Surface Processes and Landforms, 44(15), 2957–2967. https://doi.org/10.1002/esp.4721
34. Friedman, J. H. (2001). Greedy function approximation: A gradient boosting machine. *The Annals of Statistics, 29*(5), 1189–1232. https://doi.org/10.1214/aos/1013203451
35. Gaudette, L., Japkowicz, N. (2009). Evaluation Methods for Ordinal Classification. In: Gao, Y., Japkowicz, N. (eds) Advances in Artificial Intelligence. Canadian AI 2009. Lecture Notes in Computer Science(), vol 5549. Springer, Berlin, Heidelberg. https://doi.org/10.1007/978-3-642-01818-3_25
36. Gholizadeh, A., Borůvka, L., Saberioon, M. M., & Vašát, R. (2015). Visible, near-infrared, and mid-infrared spectroscopy applications for soil assessment with emphasis on soil organic matter content and quality: A review. Applied Spectroscopy Reviews, 50(2), 139–162.
37. Graham, R. L. (1969). Bounds on multiprocessing timing anomalies. SIAM Journal on Applied Mathematics, 17(2), 416–429. https://doi.org/10.1137/0117039
38. Guidoni, S., Gangemi, L., & Mania, E. (2012). Slope viticulture risk factors impacting on the environment equilibrium: The case of North-West Italy. In *IXth International Terroir Congress: Proceedings* (Vol. 2, pp. 6–39). Alliance PartenairesGraphiques.https://iris.unito.it/handle/2318/105140
39. Hao, L., Zhang, Z. & Yang, X. Mine tailing extraction indexes and model using remote-sensing images in southeast Hubei Province. Environ Earth Sci 78, 493 (2019). https://doi.org/10.1007/s12665-019-8439-1
40. Hunt, G. R. (1977). Spectral signatures of particulate minerals in the visible and near infrared. Geophysics, 42(3), 501–513.https://doi.org/10.1190/1.1440721

41. Khan, Farhat Ullah & Khan, Adnan & Li, Kai &Xuexuan, Xu & Adnan, Muhammad &Sh, F. & Ra, Ahmad & Khan, Ahmad & Nawaz, Taufiq & Zaman, Faisal. (2022). Influences of Long-term Crop Cultivation and Fertilizer Management on Soil Aggregates Stability and Fertility in the Loess Plateau, Northern China. Journal of Soil Science and Plant Nutrition. 22. 1446-1457. https://doi.org/10.1007/s42729-021-00744-1
42. Kokaly, R.F., Clark, R.N., Swayze, G.A., Livo, K.E., Hoefen, T.M., Pearson, N.C., Wise, R.A., Benzel, W.M., Lowers, H.A., Driscoll, R.L., and Klein, A.J., 2017, USGS Spectral Library Version 7: U.S. Geological Survey Data Series 1035, 61 p., https://doi.org/10.3133/ds1035.
43. Konert, M., & Vandenberghe, J. (1997). Comparison of laser grain size analysis with pipette and sieve analysis: A solution for the underestimation of the clay fraction. Sedimentology, 44(3), 523–535. https://doi.org/10.1046/j.1365-3091.1997.d01-38.x
44. Kruse, F. A., Lefkoff, A. B., Boardman, J. W., Heidebrecht, K. B., Shapiro, A. T., Barloon, P. J., & Goetz, A. F. H. (1993). The spectral image processing system (SIPS)—Interactive visualization and analysis of imaging spectrometer data. Remote Sensing of Environment, 44(2–3), 145–163.https://ui.adsabs.harvard.edu/link_gateway/1993AIPC..283..192K/doi:10.1063/1.44433
45. Kuhn, M. (2008). Building Predictive Models in R Using the caret Package. Journal of Statistical Software, 28(5), 1–26. https://doi.org/10.18637/jss.v028.i05
46. Kühn, P., Terhorst, B., &Ottner, F. (2006). Micromorphology of middle Pleistocene palaeosols in northern Italy. *Quaternary International*, *156–157*, 156–166. https://doi.org/10.1016/j.quaint.2006.05.026
47. Lagacherie, P. (2008). Digital Soil Mapping: A State of the Art. In: Hartemink, A.E., McBratney, A., Mendonça-Santos, M.d. (eds) Digital Soil Mapping with Limited Data. Springer, Dordrecht. https://doi.org/10.1007/978-1-4020-8592-5_1
48. Landis, J. R., & Koch, G. G. (1977). The measurement of observer agreement for categorical data. Biometrics, 33(1), 159–174. https://doi.org/10.2307/2529310
49. Maher, B. A. (2016). Palaeoclimatic records of the loess/palaeosol sequences of the Chinese Loess Plateau. Quaternary Science Reviews, 154, 23–84. https://doi.org/10.1016/j.quascirev.2016.08.004
50. Malandra, F., Vitali, A., Urbinati, C., & Garbarino, M. (2018). 70 Years of Land Use/Land Cover Changes in the Apennines (Italy): A Meta-Analysis. Forests, 9(9), 551. https://doi.org/10.3390/f9090551
51. Malvern Panalytical. (n.d.). Determining the particle size distribution of metal powders. Retrieved September 22, 2026, from https://www.malvernpanalytical.com/tw/learn/knowledge-center/insights/determining-the-particle-size-distribution-of-metal-powders/
52. Marchetti, B., Castelli, G., & Corvaro, F. (2025). Evaluation of Environmental Impacts Related to Land Use Modification in the Central Apennines of Italy. Highlights of Sustainability, 4(4), 240–255. https://doi.org/10.54175/hsustain4040015
53. McBratney, A. B., Mendonça Santos, M. L., & Minasny, B. (2003). On digital soil mapping. Geoderma, 117(1–2), 3–52. https://doi.org/10.1016/S0016-7061(03)00223-4
54. Meyer, H., & Pebesma, E. (2021). Predicting into unknown space? Estimating the area of applicability of spatial prediction models. Methods in Ecology and Evolution, 12(9), 1620–1633. https://doi.org/10.1111/2041-210X.13650

55. Mombrini, E., Tamea, S., Viglione, A., and Revelli, R.: A 60-year drought analysis of meteorological data in the western Po River basin, Hydrol. Earth Syst. Sci., 29, 2255–2273, https://doi.org/10.5194/hess-29-2255-2025
56. Moore, I. D., & Burch, G. J. (1986). Physical basis of the length-slope factor in the Universal Soil Loss Equation. Soil Science Society of America Journal, 50(5), 1294–1298. https://doi.org/10.2136/sssaj1986.03615995005000050042x
57. Moore, I. D., Grayson, R. B., & Ladson, A. R. (1991). Digital terrain modelling: A review of hydrological, geomorphological, and biological applications. Hydrological Processes, 5(1), 3–30. https://doi.org/10.1002/hyp.3360050103
58. Morelli, R., Zanzotti, R., Pindo, M., Donati, C., Cestaro, A., &Coller, E. (2025). Pedological origin and edaphic factors drive biota in vineyard soils of Northeast Italy. Soil Biology and Biochemistry, 192, 109345. https://doi.org/10.1016/j.soilbio.2024.109345
59. Mzid, N., Pignatti, S., Huang, W., & Casa, R. (2021). An Analysis of Bare Soil Occurrence in Arable Croplands for Remote Sensing Topsoil Applications. Remote Sensing, 13(3), 474. https://doi.org/10.3390/rs13030474
60. Nachtergaele, F.. (2017). Classification Systems: FAO. Reference Module in Earth Systems and Environmental Sciences. https://doi.org/10.1016/B978-0-12-409548-9.10520-2
61. Nduwamungu, C., Ziadi, N., Tremblay, G. F., & Parent, L.-É. (2009). Near-infrared reflectance spectroscopy prediction of soil properties: Effects of sample cups and preparation. Soil Science Society of America Journal, 73(6), 1896–1903. https://doi.org/10.2136/sssaj2008.0213
62. Nyall Dawson, Jürgen Fischer, Matthias Kuhn, Alessandro Pasotti, Denis Rouzaud, mhugent, Alexander Bruy, Tim Sutton, Martin Dobias, Mathieu Pellerin, Even Rouault, Víctor Olaya, Paul Blottiere, Werner Macho, Julien Cabieces, Radim Blazek, Loïc Bartoletti, Gary Sherman, Harrissou Sant-anna, … Borys Jurgiel. (2026). qgis/QGIS: 3.44.15 (Versions final-3_44_15) [Computer software]. Zenodo. https://doi.org/10.5281/zenodo.22962160
63. Panizza, M., & Piacente, S. (2008). La geodiversità e una sua applicazione nel territorio emiliano. *Il Geologo dell'Emilia-Romagna, 29*, 35–37. https://www.geologiemiliaromagna.it/old/rivista/2008-29_Panizza.pdf
64. Parco Regionale dello Stirone e del Piacenziano. (2011). The gullies in loc. Trabucchi. Parks.it. https://www.parks.it/parco.stirone.piacenziano/Epar.php
65. Persichillo, M. G., Bordoni, M., &Meisina, C. (2017). The role of land use changes in the distribution of shallow landslides. *Science of The Total Environment*, *574*, 924–937. https://doi.org/10.1016/j.scitotenv.2016.09.125
66. Piacenza climatenormals. (2026). Piacenza climate — normals and trends. ClimateMemory. https://climatememory.com/en/climate/italy/piacenza
67. Pornaro, C., Meggio, F., Tonon, F., Mazzon, L., Sartori, L., Berti, A., & Macolino, S. (2022). Selection of inter-row herbaceous covers in a sloping, organic, non-irrigated vineyard. PLOS ONE, 17(12), e0279759. https://doi.org/10.1371/journal.pone.0279759

68. Provincia di Piacenza. (2016, March 4). The province of Piacenza and its land. https://web.archive.org/web/20160304041958/http://www.provincia.piacenza.it/pagina.php?IDpag=58&idvocebox=65
69. Regione Emilia-Romagna. (2024). Geologicallandscape of Emilia-Romagna. https://ambiente.regione.emilia-romagna.it/en/geologia/geology/geological-heritage/geological-landscape-new
70. Renard, K. G., Foster, G. R., Weesies, G. A., McCool, D. K., & Yoder, D. C. (1997). Predicting soil erosion by water: A guide to conservation planning with the Revised Universal Soil Loss Equation (RUSLE) (Agriculture Handbook No. 703). United States Department of Agriculture.
71. Roberts, D. R., Bahn, V., Ciuti, S., Boyce, M. S., Elith, J., Guillera-Arroita, G., Hauenstein, S., Lahoz-Monfort, J. J., Schröder, B., Thuiller, W., Warton, D. I., Wintle, B. A., Hartig, F., & Dormann, C. F. (2017). Cross-validation strategies for data with temporal, spatial, hierarchical, or phylogenetic structure. Ecography, 40(8), 913–929. https://doi.org/10.1111/ecog.02881
72. Sadeghi, M., Babaeian, E., Tuller, M., & Jones, S. B. (2017). The optical trapezoid model: A novel approach to remote sensing of soil moisture applied to Sentinel-2 and Landsat-8 observations. Remote Sensing of Environment, 198, 52-68. https://doi.org/10.1016/j.rse.2017.05.041
73. Schad, P. (2023). World Reference Base for Soil Resources—Its fourth edition and its history. Journal of Plant Nutrition and Soil Science, 186(2), 151-163. https://doi.org/10.1002/jpln.202200417
74. Schütte, Rebekka&Plaas, Elke & Gómez, J. & Guzmán, Gema. (2020). Profitability of erosion control with cover crops in European vineyards under consideration of environmental costs. Environmental Development. 35. 100521. https://doi.org/10.1016/j.envdev.2020.100521
75. Shi, G.; Shangguan, W.; Zhang, Y.; Li, Q.; Wang, C.; Li, L. Reducing location error of legacy soil profiles leads to improvement in digital soil mapping. Geoderma 2024, 447, https://doi.org/10.1016/j.geoderma.2024.116912.
76. Stenberg, B., Viscarra Rossel, R. A., Mouazen, A. M., & Wetterlind, J. (2010).Visible and near infrared spectroscopy in soil science. Advances in Agronomy, 107, 163–215. https://doi.org/10.1016/S0065-2113(10)07005-7
77. Stevens, T., Thomas, D. S. G., Armitage, S. J., Lunn, H. R., & Lu, H. (2007). Reinterpreting climate proxy records from late Quaternary Chinese loess: A detailed OSL investigation. Earth-Science Reviews, 80(1-2), 111-136. https://doi.org/doi:10.1016/j.earscirev.2006.09.001
78. Tanda, M. G., Cafiero, L., Castellarin, A., Colombo, A., Colosio, P., De Michele, C., Martinengo, M., Neri, M., Spadoni, A., Todaro, V., Viglione, A., & Ranzi, R. (2025). Characterization of precipitation extremes, flow rates and flood volumes, in the context of climate change for the Po River Basin District. In G. Frega& F. Macchione (Eds.), *Technologies for integrated river basin management* (Vol. 46, pp. 63–72). EdiBios. https://hdl.handle.net/11381/3038613
79. Tucker, C. J. (1979). Red and photographic infrared linear combinations for monitoring vegetation. Remote Sensing of Environment, 8(2), 127–150. https://doi.org/10.1016/0034-4257(79)90013-0
80. van der Meer, F. D., van der Werff, H. M. A., & van Ruitenbeek, F. J. A. (2014). Potential of ESA's Sentinel-2 for geological applications. Remote Sensing of Environment, 148, 124–133. https://doi.org/10.1016/j.rse.2014.03.022

81. Višnić T, Marković SB, Vasiljević Đ (2013) “Loessland“ Project” – The development perspectives of the first loess geosite in Serbia Researches Reviews of the Department of Geography. Tour Hotel Manag 42(2013):110–121. https://doi.org/10.3986/AGS51305
82. Wang, L., & Liu, H. (2006). An efficient method for identifying and filling surface depressions in digital elevation models for hydrologic analysis and modelling. International Journal of Geographical Information Science, 20(2), 193–213. https://doi.org/10.1080/13658810500433453
83. Wani, J. M., E. Gleason, K., Dall’Amico, M., Di Paolo, F., Tasin, S., Roati, G., Brian, M., Tornatore, F., and Rigon, R.: Three decades of snow water equivalent dynamics in the Po River Basin, Italy: Trends and Implications, EGUsphere [preprint], https://doi.org/10.5194/egusphere-2025-5520
84. Xiong, LY., Li, SJ., Hu, GH. et al. Past rainfall-driven erosion on the Chinese loess plateau inferred from archaeological evidence from Wucheng City, Shanxi. Commun Earth Environ 4, 4 (2023). https://doi.org/10.1038/s43247-022-00663-8
85. Xu, H. (2006). Modification of normalised difference water index (NDWI) to enhance open water features in remotely sensed imagery. International Journal of Remote Sensing, 27(14), 3025–3033. https://doi.org/10.1080/01431160600589179
86. Zerboni, A., Trombino, L., Frigerio, C. et al. The loess-paleosol sequence at Monte Netto: a record of climate change in the Upper Pleistocene of the central Po Plain, northern Italy. J Soils Sediments 15, 1329–1350 (2015). https://doi.org/10.1007/s11368-014-0932-2
87. Zhuang, J., Kong, J., Zhu, Y. et al. The structural evolution of undisturbed loess due to water infiltration. Sci Rep 14, 14880 (2024). https://doi.org/10.1038/s41598-024-65838-zZhuang, J., Kong, J., Zhu, Y. et al. The structural evolution of undisturbed loess due to water infiltration. Sci Rep 14, 14880 (2024). https://doi.org/10.1038/s41598-024-65838-z
88. Zuffetti, A., et al. (2018). The Po Plain–Northern Apennines border: The interplay between Late Pleistocene loess–paleosol sequences, tectonic reliefs and fluvial terrace systems. Catena, 167, 176–190.https://doi.org/10.1016/j.catena.2018.07.026